APPLICATIONS OF THE BOUNDARY-ELEMENT METHOD FOR ELECTROKINETICS IN MICROFLUIDICS

BY

Dustin L. House

Dissertation

Submitted to the Faculty of the

Graduate School of Vanderbilt University

in partial fulfillment of the requirements

for the degree of

DOCTOR OF PHILOSOPHY

in

Mechanical Engineering

May, 2012

Nashville, Tennessee

Approved:

Professor Haoxiang Luo, Chair

Professor Deyu Li

Professor Jon Edd

Professor M. Douglas LeVan

To my parents, Kendall and Vickie,

for their endless supply of love and support.

ACKNOWLEDGMENTS

It has been a long and eventful journey. During my time at Vanderbilt University, there have been many to whom I owe my gratitude.

For his never-ending supply of answers and his ability to inspire, I must thank my advisor, Dr. Haoxiang Luo. As a beacon, he ensured that I never lost sight of the ultimate goal. I would not have made it this far without his encouragement and persevering sense of urgency.

My commitment to the field of BioMEMS comes from my previous advisor, Dr. Dongqing Li. His passion for advancing this technology was stirring, and deeply motivated those around him. He introduced me to the field and gave me the confidence necessary to withstand challenging times. For that I am sincerely thankful.

Having made Olin Hall my home for the past five years, I have developed great relationships with the faculty from the Mechanical Engineering Department and also the Chemical and Biomolecular Engineering Department. For his empathy, I owe Dr. Nilanjan Sarkar. As the Director of Graduate Studies, he was immensely supportive in my academic career. For the depth of their knowledge and everlasting support I owe many thanks to Dr. Greg Walker and Dr. Douglas LeVan. And for their guidance and helpful evaluations, I owe gratitude to committee members, Dr. Jon Edd and Dr. Deyu Li.

While attending Ohio Northern University, I had the pleasure of studying under a greatly influential person in my life, Dr. John-David Yoder. He had an admirable way of getting the most out of the students in class. His faith in my abilities instilled a confidence to which I am forever thankful. Without his advice and direction, my academic career would never have reached such heights.

It is easy to get lost in the intricate networks that help campus operate. To help guide students through this in their career, we have an invaluable guide in Suzanne Weiss. I could never have made it this long without her benevolent support.

During the early mornings and late evenings, I was kept sane and well entertained by my good friends and fellow graduate students. They, too, were instrumental in my success. To Nicholas Roberts, Brandon Travis, Barbaros Çetin, Steve Vilt and Paulo Ferreira de Sousa, I owe thanks. And for their assistance, to my former and current labmates Yuejun Kang, Zhemin Wu, Yandong Gao, Hu Dai and Bo Yin, I owe gratitude.

Dr. C. Pozrikidis of the University of Massachusetts, Amherst has been a paramount source of knowledge in my academic career. The present code is based on the BEMLIB, a free online software library that he developed. His texts, heavily referenced in this work, have served as unbounded wealth of answers. For this I am deeply thankful.

For its financial support, I am sincerely appreciative to the Mechanical Engineering Department. During and after my transition from one research area to another, the department offered the necessary assistance to help me stay on track in my academic career.

My family has always served as a firm foundation of love and support. I can never repay the amount of help they offered during this process. And to my future wife, Courtney, I offer the most sincere of thanks. Her unyieldingly positive attitude brings out the best in me. I could never have made it without her.

CONTENTS

LIST OF FIGURES

LIST OF TABLES

CHAPTER I

INTRODUCTION

1.1 Motivation

The promise of fast and portable diagnoses of dangerous infectious agents created a large growth in lab-on-a-chip (LOC) technology through the 1990s [1, 2]. Also referred to as micro-total analysis systems (μTAS), these devices are often described as miniature laboratories. They are small enough to be portable, but provide the same functionality as their room-sized counterparts [3]. Other than portability, advantages that are often listed for these systems include reduced operating costs, shorter testing times, automation and high throughput [1]. Recent growth in this technology was undoubtedly catalyzed by preceding advances in microfabrication [4]. The ability to construct miniature devices that can hold and manipulate microliter fluid volumes induced tremendous growth in microfluidic studies. This, in turn, lead to a great number of applications. Others have compiled more exhaustive lists of applications for microfluidics, but a sample of the more prominent topics would include fluid optics, inkjet printing, drug discovery, biosynthesis, bio-warfare defense, food and agriculture testing and the most common application, medicinal diagnostics.

Due mostly to the simplicity of their integration and use, electric fields have become a popular form of actuation in microfluidics. This technique eliminates the need for micro-scaled mechanical components such as pumps, valves and mixers. Using an electric field, one can induce bulk fluid motion within in a microchannel through a process called electroosmotic flow (EOF). Additionally, electric fields can drive downstream motion of individual dielectric particles by means of their net charge in a process referred to as electrophoresis (EP). Each of these effects are well documented [3, 5–8]

and will be discussed in more detail in the following chapter.

The electrophoretic motion of a particle can be perturbed by the presence of a spatial non-uniformity in the electric field. This effect is referred to as dielectrophoresis (DEP) and it is an extensively studied topic. More detail can be found in literature [2, 7, 9–16]. A DEP force is often used to generate motion orthogonal to the direction of the applied field. The ability to generate a force acting on a micro-particle in a direction transverse to fluid flow is of particular interest to biomedical researchers. Such a capacity has allowed them to manipulate biological particles in an effort to incorporate sorting [17, 18], focusing [19–21], trapping [22–24], migration [25–27], characterization [28–30] and filtering [31, 32] processes into microfluidic devices. Additionally, DEP interaction between non-conducting particles has also conjured interest in aggregation applications [33–35]. The unique reorientation process allows for the construction of desired materials including tissues [36, 37], biocomposites [38], microwires [39] and photonic crystals [40].

Despite the number of applications for microfluidic devices, modeling and characterization of particle handling in electrokinetic flows is still a challenging task. This is especially the case for arbitrary channel geometries and large particle-to-channel size ratios, which causes significant distortion of the local electric and flow fields. Nevertheless, microfluidic channels often use complex geometries and small design features for the intricate manipulation of suspended particles. For example, Kang *et al.* [41] investigated the DEP effect of an insulating hurdle on the trajectory of electrophoretic polystyrene particles. Their objective was to use the DEP force generated near the corners of the hurdle to “push" the particles into different streamlines. The effect was introduced as a separation technique due to the fact that the streamline shift was dependent upon the size of the particle. To extend the study, the same group used a similar technique to separate white blood cells, and in a separate experiment, breast cancer cells [12]. A more adjustable form of DC-DEP was realized by Barbulovic-Nad *et al.* [42] by using an oil droplet as the insulating hurdle. In that study, adjusting

the droplet size allowed for simple dynamic control of the field gradient used to generate the DEP force. Other non-trivial microfluidic networks utilize serpentine channels [43], spiraling channels [44] and converging–diverging sections [45] to attain the field distributions necessary for DEP particle manipulation in DC or DC-biased alternating fields.

In general, accounting for the finite size of a particle in a numerical simulation is computationally demanding when attempting to model the particle's motion in a microchannel. For this reason, simplified approaches have been developed. For example, some researchers choose to take advantage of a similitude between the electric field and the fluid velocity field for electroosmotic flows [46–48]. By assuming that the particles in such flows simply follow the streamlines, the solution to the electric field alone may be used to approximate the particle motion [17, 49]. When the DEP effect on the particles is considered, a further approximation is to employ the the point dipole or multipole methods [10] to determine the DEP force. In these methods, the particle size is assumed to be infinitely small, and the DEP force can be evaluated based on a simple formula involving the undisturbed local electric field strength and its derivatives. Under these approximations, the particle's trajectory can be found by performing straightforward Lagrangian tracking. To improve the accuracy of this approach, sometimes an empirical correction factor is used to correct the particle mobility [50, 51]. The point–particle approach can be highly efficient and is valid when the size of the particle is small when compared to that of the channel. However, as the particle is close to the wall, or its size approaches that of the channel, distortion of the surrounding electric field due to the presence of the particle can no longer be neglected. A recently published and well-cited review explicitly stated the need for further studies on the perturbing influence of microchannel boundaries [2]. For example, when a non-conducting particle is close to a plane wall, it has been shown in experiments that a net DEP force is generated from the distorted electric field in the narrow gap between the particle and wall [52–54]. This force is in addition to the DEP generated by the global nonuniformity of the electric field. Some previous studies have shown that the dipolar or multipole approximation

of the DEP leads to inaccuracies when applied to a particle in the vicinity of an electrode [55–57]. Similar to the DEP approximation, ignoring the particle's presence in the flow field may oversimplify the hydrodynamics and lead to inaccurate estimate of the viscous drag on the particle. For these reasons, a study addressing the DEP mobility of particles of finite size would have to fully couple the particle together with the electric field and flow. So far there are only a few limited such studies [45, 58].

For electrokinetic particles of finite sizes, both analytical and computational approaches have been applied previously to solve the governing equations and to obtain description of the particle dynamics. For example, exact solutions [59, 60] and asymptotic expansions [61–63] have been applied to obtain expressions of the velocity or force on a spherical particle near a planar or cylindrical geometry. For an arbitrary geometrical configuration, a numerical technique is necessary to simulate the flow and electric field. Numerical methods based on volume discretization, such as the finite-element method (FEM) [64–66], have limited accuracy when the particle–wall or particle–particle separation is small compared to the particle size and a fine resolution is needed to resolve the gap region. Additionally, for transient simulations, the volume mesh often has to be regenerated every a few time steps to avoid severe mesh distortion. On the other hand, the boundary-element method (BEM) [67], which requires a surface mesh only, is superior to the FEM in accuracy and efficiency when a linear problem is considered, e.g., an electrokinetic problem with the thin-EDL assumption. Previously, the BEM has been applied in electrokinetic flows [68–70] and has shown great promises. We also have developed an in-house BEM code to solve electrokinetics of particles in arbitrary channels [71, 72]. The numerical approach can handle very small gap region (around 1% of the particle size). With slight modification, the solver can incorporate the Maxwell stress tensor and can thus be used to simulate the DEP effect on the particle.

1.2 Objectives

The goals of this work can be summarized into two objectives. First, we wish to advance the application of the boundary-element method within the field of electrokinetics in microfluidics. Under the notion that precision and the ability to efficiently optimize microchannel design is paramount to the future of LOC technology, we want to extend this numerical approach and demonstrate its capabilities. In doing so, it helps us achieve our second objective: to study and characterize several fundamental phenomena related to electrokinetic particle motion in microfluidics.

1.3 Outline

Each of the studies within this dissertation are presented as independent applications of the developed BEM. Before discussing each implementation, we will provide a background of the underlying physics and introduce the integral equations which serve as the foundation to the BEM.

Chapter 1 introduces the subject material. It serves as a brief overview of the field to provide context to the studies. Here, we report various applications by researchers. In this introduction, we intend to detail the motivation behind the studies herein and also to clarify the objectives of the work.

Chapter 2 conveys the underlying physics behind the phenomena studied. The primary electrokinetic effects discussed in this dissertation are electroosmosis, electrophoresis, dielectrophoresis and electro-orientation. As such, each topic has its own section describing its origin and the formulas used to model its effect.

Chapter 3 provides a broad overview of the boundary-element method and how it is applied. Here, we detail each of the integral equations used in this method: the 2D and 3D integral formulation for Laplace's equation and also the 2D and 3D integral formulation for Stokes' equation. Additionally, we provide the integral identities used during integration to address singularities that arise.

Chapter 4 details the results of our first application of the BEM. Here, we applied our 2D BEM code to study the electrophoretic mobility of a colloidal cylinder when arbitrarily positioned between two parallel walls. In doing so, we evaluate a wall-induced electrokinetic enhancement for the case of two walls. In this report, we find that the enhancement effect is comparable to the viscous effect introduced by the second wall. This is most significant for a tightly bounded particle.

Chapter 5 is a fundamental study of DC-DEP. Here, we implement our 3D BEM code to observe a spherical particle translating through a bent cylindrical channel. In doing so, we look at the effects of particle size, field strength and eccentricity as the particle experiences negative DEP when traveling through the bent region. The systematic study helps to characterize this effect for the case of a fundamental geometry common to microfluidic networks. We also compare our results with those obtained using the point–particle approach to clarify its limitations and justify the need for a numerical technique when the particle's size is no longer negligible.

Chapter 6 is a thorough report over the DEP interaction of ellipsoidal particles. By using our 3D BEM code, we study the field-induced chaining effect for non-conducting prolate spheroids. In this report we characterize the phenomenon by observing the finite chaining angle formed and its dependence upon the particle aspect ratio. Also addressed is the significance of electro-orientation for particles of arbitrarily initial orientation and position.

Chapter 7 serves as closing remarks to the dissertation. In this section the motivation behind the work is summarized. We present the overall conclusions and contributions made to the field. In addition, future topics of study are suggested.

CHAPTER II

BACKGROUND

2.1 Electric double layer

When in contact with an aqueous solution, a solid surface will carry a net charge. In some cases this surface charge stems from the ionization arising from the dissociation of chemical groups. This process depends on the acidic or basic strengths of these groups and the pH of the solution. In many other cases, the surface charge comes from its adsorption of ions in the solution. For most electrolyte solutions, the surface will develop a negative charge [11]. The existence of a surface charge attracts ions of opposite charge (counterions) and repels ions of like charge (co-ions) within the solution. This results in a thin layer of fluid with a net charge that balances the adjacent surface charge. This layer of fluid is commonly referred to as the electric double layer (EDL). Outside of this layer, the bulk fluid is electrically neutral.

If we assume that the surface develops a negative charge, then positive ions within the solution are drawn toward it. A diagram of the EDL in this scenario is shown in Figure 2.1. Here we see the EDL is comprised of two main sections: a compact layer and a diffuse layer. The compact layer is composed of counterions that are immobile due to their strong attraction to the surface. In general, the compact layer is only a few Angstroms in thickness and the electric potential distribution is mostly linear [4]. Beyond the compact layer exists a thicker layer of fluid in which the net charge density gradually reduces to zero. This layer is referred to as the diffuse layer and the ions within it are mobile. Thickness of the diffuse layer is dependent upon the electrical properties of the solution and can range from several nanometers to a few microns [3]. The compact layer and diffuse layer make up the EDL. Outside of the EDL, there is an

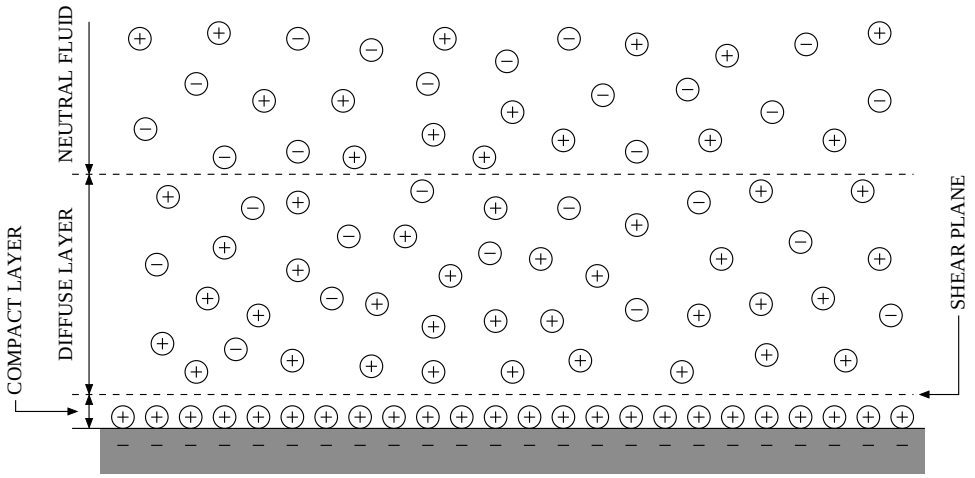

Figure 2.1: Diagram of the electric double layer.

even number of counterions and co-ions and the net charge density everywhere is zero. The plane separating the diffuse and compact layers is referred to as the shear plane. It is straightforward to experimentally measure the electric potential at this plane. This potential is referred to as the zeta potential (ζ). Determining the potential at the solid-liquid interface is more challenging. Because of this, the zeta potential is commonly used as an approximation of the electric potential at the interface [3].

The distribution of electric potential within the diffuse layer of the EDL is governed by the Poisson-Boltzmann (PB) equation. For a symmetric electrolyte (constant z), this relationship simplifies into the following form,

$$\nabla^2\phi = \frac{2zen_\infty}{\varepsilon_m}\sinh\left(\frac{ze\phi}{k_bT}\right), \tag{2.1}$$

where z is the ionic valence, e is the elementary charge, n_∞ is the bulk ionic number concentration, ε_m is the permittivity of the solution, k_b is the Boltzmann constant and T is the absolute solution temperature.

In many microfluidic studies, it is common to use an approximation referred to as the thin-EDL assumption. This method takes advantage of the large difference in length scales when comparing the EDL thickness to the enclosing geometry, *e.g.* microchannel

width. If the solution has a low electrolyte concentration (nearly pure water), then it will yield a thicker EDL. However, as was mentioned before, a *large* EDL is generally still less than a few microns in thickness. This is much smaller than the diameter of many microchannels, which are commonly on the order of 100 μm. The characteristic thickness of the EDL is commonly referred to as $1/k$, where

$$k^2 = \frac{2z^2e^2n_\infty}{\varepsilon_m k_b T}, \tag{2.2}$$

is the Debye-Hückel parameter. If a is the characteristic length scale of your system, then the thin-EDL assumption is commonly written as $ka >> 1$. Under this condition, the EDL thickness is neglected. The electric potential distribution and velocity flow field within the EDL are not considered. Instead, we use the condition of both fields at the slip plane to represent the condition of both fields at the surface. From a modeling point of view, the no-slip boundary condition common in conventional fluid mechanics is replaced with a slip velocity boundary condition that is proportional to the electric field,

$$u^S = -\frac{\varepsilon\zeta}{\mu}E, \tag{2.3}$$

where u^S is the slip velocity, ε is the dielectric constant of the electrolyte solution and ζ is the zeta potential of the surface. This is important because it means we can model electric field without having to solve the nonlinear PB equation. Outside of the EDL, there is no net charge density. Thus, by using the thin-EDL assumption, we are modeling the field as being electrically neutral everywhere. From this, we can model the electric potential using Laplace's equation,

$$\nabla^2\phi = 0. \tag{2.4}$$

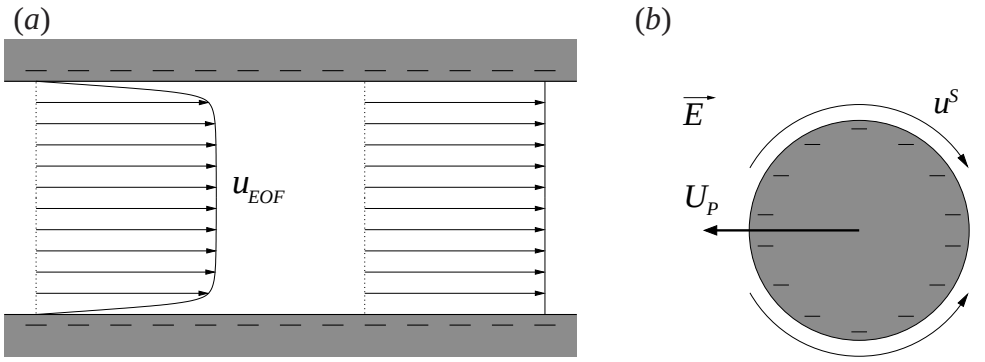

Figure 2.2: (*a*) Plug-like electroosmotic flow profile when considering a finite EDL thickness (left) and under the thin-EDL assumption (right). (*b*) Electrophoretic motion of a particle under the thin-EDL assumption.

2.2 Electroosmosis and electrophoresis

Formation of the electric double layer is a fundamental phenomenon that drives a common form of electrokinetic actuation. If an electric field is applied tangential to an EDL, it generates electrostatic forces on the ions within the EDL. The force acting on the mobile ions within the diffuse layer yields motion of the fluid in this layer in the direction of the applied field. At the characteristic length scales common in microfluidics, viscous forces dominate over inertial forces. This stems from the a large ratio of surface area to volume (typically on the order of 10^6 m [4]). A result of these effects is bulk fluid motion outside of the EDL. This electrokinetic form of pumping is referred to as electro-osmosis. The viscous motion of the fluid produces a plug-like velocity profile. When considering a finite EDL thickness, the velocity profile is similar to that seen on the left side of Figure 2.2(*a*). As mentioned previously, however, a well-accepted model for electrokinetic flow is to neglect the EDL thickness ($ka >> 1$). Under this treatment, the velocity profile resembles that shown on the right side of Figure 2.2(*a*). Based on the thin-EDL assumption, electroosmotic flow can be represented by the following relation,

$$u_{EOF} = -\frac{\varepsilon \zeta_w}{\mu} E, \tag{2.5}$$

where ζ_w is the zeta potential of the microchannel wall.

A contrasting motion arises when the charged surface is no longer stationary. Consider a rigid non-conducting particle suspended in an electrolyte solution. There still exists an EDL in this situation. It forms around the surface of the particle much like it would a plane wall. What is different about this scenario is that the charged surface is free to move under an electrostatic body force. Under an electric field, the particle will be driven toward one of the electric field while the fluid in the EDL is driven toward the opposite end. The driving force behind this motion is the Coulombic force acting on the particle's net charge. The resulting motion of the particle is referred to as electrophoresis. This form of electrokinetic motion is depicted in Figure 2.2(*b*). Under the thin-EDL assumption, the electrophoretic velocity of a particle is expressed as the *Helmholtz–Smoluchowski* equation,

$$u_{EP} = \frac{\varepsilon \zeta_p}{\mu} E, \tag{2.6}$$

where ζ_p is the zeta potential of the particle surface. Combining the advection of the surrounding fluid and electrophoretic mobility, it can be shown that a particle's velocity under both electroosmotic flow and electrophoretic motion can be described in the following manner [5],

$$U_P = \frac{\varepsilon(\zeta_p - \zeta_w)}{\mu} E, \tag{2.7}$$

2.3 Dielectrophoresis

If electrophoresis is described as a technique used to transport particles along the length of a microchannel, then dielectrophoresis could be described as the technique often used to induce a lateral migration. Under an electric field, the ions within and on the surface of the particle material will have a tendency to shift in the direction of the field that is opposite its own charge. This redistribution of charge results in a

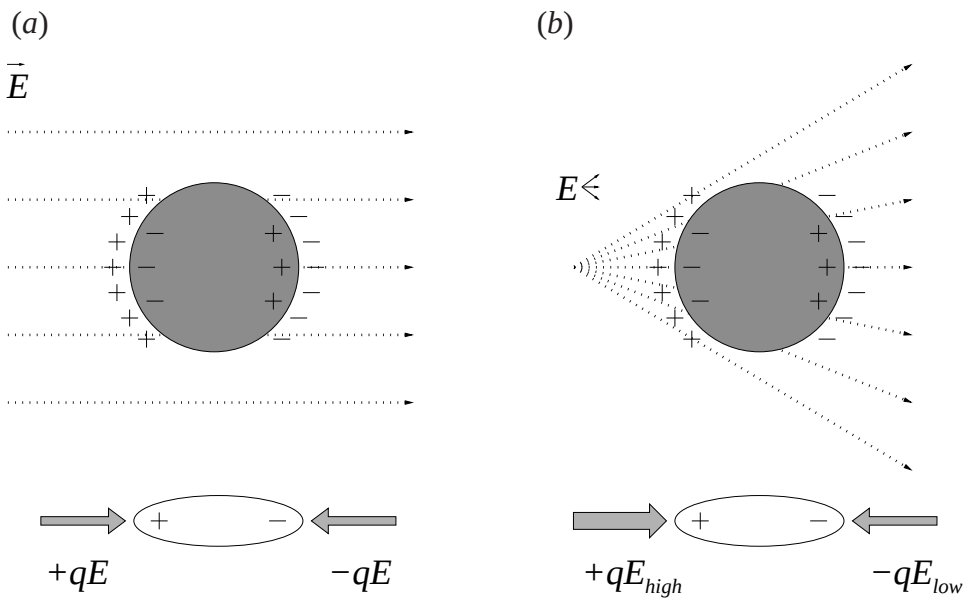

Figure 2.3: Diagram visualizing the origin of a DEP force on a particle. The dotted lines represent the electric field lines in the absence of a particle. Orientation of the dipole and Coulombic force acting on it are displayed below the particle.(*a*) Represents the case of a uniformly applied electric field whereas (*b*) represents that of a non-uniform field.

polarization of the particle. This polarization draws counter-ions within the suspending medium toward the particle surface. In the case of a dielectric particle suspended in an electrolyte solution, more charge will accumulate on the medium side of the particle–medium interface. This is because a material of low conductivity does not easily permit the migration of ions. The resulting imbalance of charge at the interface on either side of the particle yields a field-induced dipole across the particle. In a uniformly applied electric field, such as that seen in Figure 2.3(*a*), the Coulombic forces acting on the induced dipole are balanced. In a non-uniform field, however, a lack of symmetry in electric field strength across the particle yields and imbalance of force distribution. The resulting net force is referred to as the dielectrophoretic force. A schematic of how a DEP force is generated is shown in Figure 2.3(*b*).

Both alternating and direct current electric fields (AC and DC) have been widely used for generating the DEP force needed to manipulate particles. By using embedded electrodes, AC-DEP is capable of operating under reduced field strengths, which

is important to cell viability. However, it often requires a metal deposition step in the fabrication of the fluid channels. This increases complexity and raises the cost. On the other hand, DC-DEP (sometimes referred to as electrode-less DEP or insulator DEP) does not require embedded electrodes. It utilizes an irregularity in the geometry of a microchannel such as an insulating obstacle to locally alter the electric field and generate the DEP force [73]. Another advantage to DC-DEP is that it reduces fouling and electrolysis, two common problems encountered when using embedded electrodes. This work will focus on DC-DEP. The results of many DC-DEP studies are useful in reference to AC-DEP in the fact that DC-DEP simply represents the lower limit of frequency for AC-DEP.

2.3.1 Point-dipole method

To solve for the DEP force acting on a particle, there are two common approaches. The first technique discussed is a popular approach due to its simplicity. It is referred to as the point-dipole method (PDM). In this approach, detailed by Jones [10] and again by Morgan and Green [11], the higher order multipolar moments are neglected and the polarized particle is modeled using an effective dipole moment. For a spherical particle under a constant field, the effective dipole moment is,

$$\mathbf{p} = 4\pi a^3 \varepsilon_m f_{CM} \mathbf{E}, \tag{2.8}$$

where a is the particle radius and f_{CM} is the *Clausius-Mossotti* factor. Under a DC field, the *Clausius-Mossotti* factor is defined by the the conductivity of the particle, σ_p, and suspending medium, σ_m [74],

$$f_{CM} = \frac{\sigma_p - \sigma_m}{\sigma_p + 2\sigma_m}. \tag{2.9}$$

For a dielectric particle in which $\sigma_p << \sigma_m$, f_{CM} approaches the lower limit of -$\frac{1}{2}$. By modeling the particle as an infinitesimal dipole with an effective dipole moment given by Eq. (2.8), we can find the force acting on the particle,

$$\mathbf{F}_{\mathrm{DEP}} = (\mathbf{p} \cdot \nabla)\mathbf{E} = -2\pi a^3 \varepsilon_m (\mathbf{E} \cdot \nabla)\mathbf{E}. \tag{2.10}$$

After rearranging the following vector identity and considering the electric field is irrotational [10],

$$\nabla(\mathbf{E} \cdot \mathbf{E}) = 2(\mathbf{E} \cdot \nabla)\mathbf{E} + 2\mathbf{E} \times (\nabla \times \mathbf{E}). \tag{2.11}$$

we arrive at the final relation for the DEP force according to the effective moment approach, often referred to as the point-dipole method,

$$\mathbf{F}_{\mathrm{DEP}} = -\pi a^3 \varepsilon_m \nabla(\mathbf{E} \cdot \mathbf{E}) = -\pi a^3 \varepsilon_m \nabla|\mathbf{E}|^2. \tag{2.12}$$

It is important to note that this technique is only valid in cases where the particle is sufficiently smaller than its environment. This is because the finite size of a particle is neglected. The DEP force acting on the particle comes from the derivatives of the electric field at the point where the center of the particle would be located. This is why the PDM is labeled as a *point–particle approach*. Any distortion of the field from the dielectric volume of the particle is not considered. The simplicity of this approximation makes it a popular technique. Oversight of its limitations, however, can lead to significant error. This will be discussed in a later chapter.

2.3.2 Maxwell stress tensor integration

A different approach, commonly accepted to be the most rigorous approach [75], utilizes the Maxwell stress acting on the surface of a particle suspended in an electric

field. The Maxwell stress tensor (MST) describes the stress on an object within an electric and/or magnetic field. In its general form for a constant field, it is written as,

$$\mathbf{T} = \varepsilon_m(\mathbf{EE} - \frac{1}{2}|\mathbf{E}|^2\mathbf{I}) + \mu_0(\mathbf{HH} - \frac{1}{2}|\mathbf{H}|^2\mathbf{I}), \tag{2.13}$$

where μ_0 is the vacuum magnetic permeability, **I** is the unit tensor and **H** is the magnetic field vector. In this form, the product of two vectors without a dot product is the dyadic product. For a DC field, the near-field approximation is a suitable simplification to the Maxwell stress tensor [75]. Under this approximation, the magnetic field effects are neglected and the stress tensor simplifies to,

$$\mathbf{T} = \varepsilon_m(\mathbf{EE} - \frac{1}{2}|\mathbf{E}|^2\mathbf{I}). \tag{2.14}$$

The total DEP force acting on a particle can then be found by integrating this stress around the surface of the particle,

$$\mathbf{F}_{\text{DEP}} = \int_P \mathbf{T} \cdot \mathbf{n}\, \mathrm{d}S = \int_P [\varepsilon_m(\mathbf{EE} - \frac{1}{2}|\mathbf{E}|^2\mathbf{I})] \cdot \mathbf{n}\, \mathrm{d}S \tag{2.15}$$

The Neumann boundary condition utilized for a particle under general conditions is continuity of the normal component of electric displacement. Expressed numerically for a point *x*, on the interface, it takes on the following form [70],

$$\varepsilon_m \left.\frac{\partial \phi_m}{\partial \mathbf{n}}\right|_x = \varepsilon_p \left.\frac{\partial \phi_p}{\partial \mathbf{n}}\right|_x \tag{2.16}$$

where ε_p is the permittivity of the particle and ϕ_m and ϕ_p correspond to the electric potential just outside and inside of the particle interface, respectively. In the studies performed herein, it is assumed that the particle is a dielectric such that $\varepsilon_p << \varepsilon_m$. With this assumption, we model the particle using an insulating homogeneous boundary condition, $\partial\phi/\partial\mathbf{n} = 0$, where the electric field does not penetrate the particle surface.

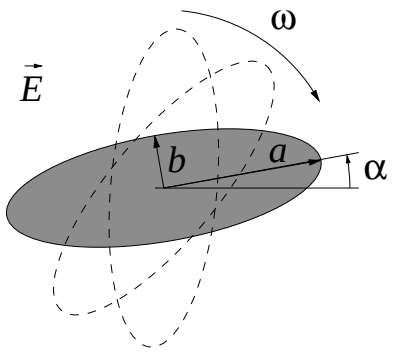

Figure 2.4: Diagram visualizing the electro-orientation process of an ellipsoid.

Under this condition, the field vector is orthogonal to the surface normal, yielding $\mathbf{E}\cdot\mathbf{n} = 0$. After applying this fact to Eq. (2.15), the first term is zero based on the fact that $\mathbf{EE}\cdot\mathbf{n} = \mathbf{E}\cdot(\mathbf{E}\cdot\mathbf{n})$. Through this simplification, the total DEP force is found through the following integral,

$$\mathbf{F}_{\mathrm{DEP}} = -\frac{\varepsilon_m}{2}\int_P |\mathbf{E}|^2\mathbf{n}\,\mathrm{d}S. \tag{2.17}$$

2.4 Electro-orientation

A constant electric field that is spatially independent of phase does not exert a torque on an isotropic spherical particle. This is owed to the fact that the local Maxwell stress is always in line with the surface normal and passes through the centroid of the particle. For a non-spherical particle, however, a torque can arise. It is well known that a lossless dielectric particle in a DC field will align itself such that its longest axis is parallel with the electric field. This field-induced self-orientation process of a non-spherical particle is referred to as electro-orientation. It can be seen depicted in Figure 2.4. By approximating the particle as an infinitesimal dipole and utilizing the effective moment method, Jones [10] formulates the DEP torque for a particle under this condition,

$$T_{\mathrm{DEP}} = \frac{4\pi abc(\varepsilon_p-\varepsilon_m)^2(L_\perp - L_\parallel)\,|E|^2\sin\alpha\cos\alpha}{3\varepsilon_m\left[1+\left(\frac{\varepsilon_p-\varepsilon_m}{\varepsilon_m}\right)L_\parallel\right]\left[1+\left(\frac{\varepsilon_p-\varepsilon_m}{\varepsilon_m}\right)L_\perp\right]} \tag{2.18}$$

where θ is the angle between the longest axis, a, and the electric field. In a later section, the interaction of non-spherical particles will be addressed. Specifically, prolate spheroids will be modeled. Thus, it is of interest to simplify the above equation. For a prolate spheroid in which $b = c$, the depolarization factors, $L_\perp$ and $L_\parallel$ reduce to the following expressions,

$$L_\parallel = \frac{b^2}{2a^2e^3}\left[\ln\left(\frac{1+e}{1-e}\right) - 2e\right] \tag{2.19}$$

$$L_\perp = \frac{1 - L_\parallel}{2}, \tag{2.20}$$

where the eccentricity is defined as $e = \sqrt{1 - b^2/a^2}$. For the a prolate spheroid under the limiting case of $\varepsilon_p << \varepsilon_m$, Eq. (2.18) reduces to

$$T_{\text{DEP}} = \frac{4\pi ab^2\varepsilon_m(L_\perp - L_\parallel)\,|E|^2 \sin\alpha\cos\alpha}{3(1 - L_\parallel)(1 - L_\perp)}. \tag{2.21}$$

Analogous to the previous section, there exists a more computationally demanding technique that is a more direct approach to calculating the DEP torque. Similarly, this method utilizes full integration of the Maxwell stress tensor and provides more accurate results for cases when a colloidal particle is positioned near another surface, whether it is another particle or a channel well. Implementing the Maxwell stress tensor, the DEP torque on a particle can be expressed as,

$$\mathbf{T}_{\text{DEP}} = \int_P (\mathbf{T}\cdot\mathbf{n}) \times \mathbf{r}\, \mathrm{d}S, \tag{2.22}$$

where $\mathbf{r}$ is the displacement vector (lever arm). Because $\mathbf{E}\cdot\mathbf{n} = 0$ is zero on the surface of the particle, we can make the same simplifications that were made in the previous section to arrive at the following relation,

$$\mathbf{T}_{\text{DEP}} = -\frac{\varepsilon_m}{2}\int_P |\mathbf{E}|^2\,(\mathbf{n}\times\mathbf{r})\,\mathrm{d}S. \tag{2.23}$$

2.5 Influence of electric fields on cells

Many of the applications discussed in this work involve the use of cells. In this use, care must be taken to ensure the viability of the type of cell used. Exposing cells to strong electric fields can alter their natural state and under certain conditions it can lead to cell lysis [5]. In a review, Voldman discusses two common negative results when using electric fields to manipulate cells [76]. One is an altered cell membrane potential. Under an electric field, the cell membrane can develop an “imposed" electric potential that alters the natural bioelectricity, and ultimately, the cell phenotype. For direct current DEP, the topic of this work, the imposed potential is proportional to $1.5|E|a$ where a is the radius of the cell. It is often desirable to keep the imposed potential well below the naturally existing potential (tens of millivolts) to reduce negative effects [76]. Under a strong enough field, it is possible to rupture the cell membrane. Some researchers have used this technique to modify cells through electroporation or electrofusion [77]. However, the DEP forces discussed herein are dependent upon viability of the cell. Because of this, and for reasons stated above, it is necessary to reduce field-induced cell membrane stresses by reducing field strengths [73].

Another potentially negative effect arising from the use of electric fields is Joule heating. The current passing through the medium results in a temperature rise. It has been shown that a temperature rise from Joule heating can be expressed as $\Delta T \sim L^2|E|^2$ [78]. It was previously reported that a temperature rise in a suspending medium can lead to physiological changes within the cell. A more significant increase in temperature, (4°C above a cell’s physiological temperature) can lead to cell death [76]. A third factor to consider is pH variations that could develop within the suspending medium. Water electrolysis at the electrodes can yield pH gradients. This can induce cell stresses, alter the transport of certain biological particles or modify channel wall surfaces [79]. However, as has been exemplified through numerous studies, if cautiously applied, DC fields are still a capable form of cell manipulation [12, 43, 73, 80–82].

Lastly, it is important to note the significance of the cell membrane's dielectric properties. When placed within a DC field, the membrane acts as a low loss capacitor [10]. Thus, the electric field does not penetrate the membrane. Based on this, we can effectively model a cell as an insulating surface. This is why simulations within this study utilize the homogeneous Neumann boundary condition, $\partial\phi/\partial\mathbf{n} = 0$, at particle surfaces. Additionally, most cells will have a negative surface charge due to the negatively charged groups (carboxylates, phosphates) on its surface [77]. This would yield a positively-charged EDL.

CHAPTER III

NUMERICAL APPROACH

One of the primary goals of this work is to extend and promote application of the boundary-element method within the field of electrokinetic-based microfluidics. This technique is well-suited for linear partial differential equations. This is the case for electrokinetics under the thin-EDL assumption. Analytical techniques such as asymptotic approaches often require elementary geometries. To perform systematic studies required in the design of microfluidic networks, a computational method is necessary. Commercial software such as COMSOL Multiphysics® allows modeling of complex geometries by utilizing a finite-element method. Although suitable, this method is inefficient and can be inaccurate.

Finite-element methods require a volumetric mesh for 3D simulations. The boundary-element method only requires a surface mesh to model a 3D domain. This is the primary advantage when using a BEM — you can reduce your computational domain by one dimension when compared to finite-element techniques. With the boundary solution known, you can find the solution at any point within the volume of your domain through an explicit equation in post-processing. Not only is this a more efficient approach, but it is a more accurate approach. Consider two surfaces in a 3D computational domain. As the distance between these surfaces is reduced, the resolution of the mesh must be increased. When utilizing a finite-element approach, this requires a fine volume mesh. Adapting the 2D surface mesh required of a BEM, however, is not as computationally demanding. In addition, the BEM utilizes Gauss quadratures for numerical integration, which provides a spectral convergence. Therefore, the BEM is able to exceed the narrow gap limits of techniques using a volumetric mesh. Thus, we present the BEM as a

powerful technique in systematic studies necessary for the design and optimization of channel geometries.

In our work, we have completed both a two-dimensional and a three-dimensional version of the code, written in Fortran. Each is based upon the framework of a free online library, BEMLIB [83]. Each of the electrokinetic phenomena discussed in Chapter II are incorporated into the solver. For transient simulations, temporal updating of the velocity and position of the particle is achieved using a second-order Runge–Kutta scheme. This improved Euler approach is written as

$$\begin{aligned} \mathbf{k}_1 &= \mathbf{u}(\mathbf{x}_n) \\ \mathbf{k}_2 &= \mathbf{u}(\mathbf{x}_n + \frac{1}{2}\Delta t \mathbf{k}_1) \\ \mathbf{x}_{n+1} &= \mathbf{x}_n + \frac{1}{2}\Delta t(\mathbf{k}_1 + \mathbf{k}_2). \end{aligned} \tag{3.1}$$

where $\mathbf{x}_n$ is the particle location at t_n. Integrals over each element are carried out using Gauss–Legendre quadratures, and the resulting linear equation systems are solved using the LAPACK library. Three-dimensional simulations are performed in parallel using MPI.

3.1 Derivation of the boundary-integral

Before discussing application of the boundary-element method, it is appropriate that we discuss its origins. A more extensive derivation can be found in texts by C. Pozrikidis [67, 83]. Here, we begin with Green's identities. If we consider two twice continuously differentiable functions, $\psi(x, y)$ and $f(x, y)$, then Green's first identity states that the following relation applies,

$$\psi \, \nabla^2 f = \nabla \cdot (\psi \, \nabla f) - \nabla\psi \cdot \nabla f. \tag{3.2}$$

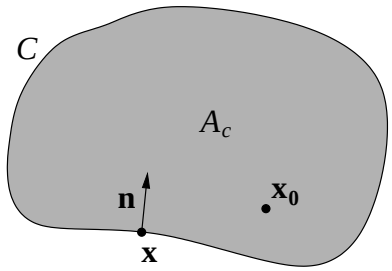

Figure 3.1: An example of a control area, A_C, confined by closed line, C.

We can produce Green's second identity by switching ψ and f and subtracting the result from Green's first identity,

$$\psi\,\nabla^2 f - f\,\nabla^2\psi = \nabla\cdot(\psi\,\nabla f - f\,\nabla\psi). \tag{3.3}$$

Given $\mathbf{x} = (x, y)$, if we assume $f(\mathbf{x})$ to be non-singular and consider this relation for a Green's function, $g(\mathbf{x}, \mathbf{x}_0)$, in the place of $\psi(\mathbf{x})$, we find

$$-f(\mathbf{x})\,\nabla^2 g(\mathbf{x}, \mathbf{x}_0) = \nabla\cdot[\,g(\mathbf{x}, \mathbf{x}_0)\,\nabla f(\mathbf{x}) - f(\mathbf{x})\,\nabla g(\mathbf{x}, \mathbf{x}_0)]. \tag{3.4}$$

A Green's function of Laplace's equation satisfies the following,

$$\nabla^2 g(\mathbf{x}, \mathbf{x}_0) + \delta(\mathbf{x} - \mathbf{x}_0) = 0, \tag{3.5}$$

in which $\mathbf{x}$ is the field point, $\mathbf{x}_0$ is the singular point and $\delta(\mathbf{x}-\mathbf{x}_0)$ is Dirac's delta function in two dimensions. With this, we can simplify Eq. (3.4) into the form,

$$f(\mathbf{x})\,\delta(\mathbf{x} - \mathbf{x}_0) = \nabla\cdot[\,g(\mathbf{x}, \mathbf{x}_0)\,\nabla f(\mathbf{x}) - f(\mathbf{x})\,\nabla g(\mathbf{x}, \mathbf{x}_0)]. \tag{3.6}$$

This result can then be integrated over a control area, A_C, bounded by a closed surface, C, such as the one shown in Figure 3.1. After using the divergence theorem to change

the area integral into a line integral, we obtain,

$$f(\mathbf{x}_0) = -\int_C g(\mathbf{x}_0, \mathbf{x})[\mathbf{n}(\mathbf{x}) \cdot \nabla f(\mathbf{x})]dl(\mathbf{x}) + \int_C f(\mathbf{x})[\mathbf{n}(\mathbf{x}) \cdot \nabla g(\mathbf{x}_0, \mathbf{x})]dl(\mathbf{x}), \qquad (3.7)$$

for the case of $\mathbf{x}_0$, the singular point, located inside of the control area. Here, $\mathbf{n}$ is the surface normal pointing into the control area, and dl is a differential arc length along C. Eq. (3.7) allows us to find the value of a harmonic function at any point within the control area when the boundary values and boundary distribution of the normal derivative are known. The first integral is referred to as the *single-layer potential* and the second as the *double-layer potential*. This terminology is common in BEM literature and stems from an analogy using electrostatics.

3.2 Boundary-integral formulation for Laplace's equation

In the following studies, we assume that the thickness of the EDL, i.e., the Debye length k^{-1}, adjacent to all surfaces is small when compared to particle size or any particle–wall or particle–particle gap widths such that there is no EDL overlapping and the thin-EDL approximation may be used. With this approximation, the entire flow field is electrically neutral, and the distribution of electric potential, ϕ, is governed by Laplace's equation from Eq. (2.4). Under this condition, we can utilize the boundary-integral, Eq. (3.7), to recast the Laplace equation and then solve it using the developed boundary-element method.

3.2.1 Two-dimensional formulation

Following the derivation in Section 3.1, the electric potential at a point $\mathbf{x}_0$ in the interior of the 2D flow field, $\phi(\mathbf{x}_0)$, can be written in the following form,

$$\phi(\mathbf{x}_0) = -\int_C g(\mathbf{x}, \mathbf{x}_0)[\mathbf{n} \cdot \nabla\phi]dl(\mathbf{x}) + \int_C \phi[\mathbf{n} \cdot \nabla g(\mathbf{x}, \mathbf{x}_0)]dl(\mathbf{x}), \qquad (3.8)$$

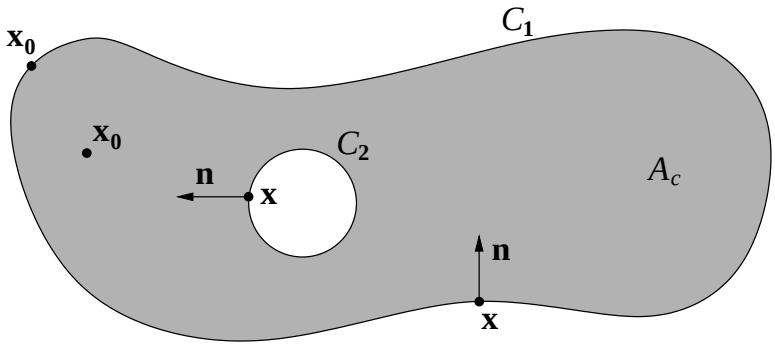

Figure 3.2: An example of a boundary, $C = C_1 + C_2$, confining a control area, A_C, that would be used in the boundary-element method. The form of the integral equation depends on the location of the singular point, $\mathbf{x}_0$.

where $\mathbf{x} = (x, y)$, $r = |\mathbf{x} - \mathbf{x}_0|$, and

$$\begin{aligned} g(\mathbf{x}, \mathbf{x}_0) &= -\frac{1}{2\pi} \ln r, \\ \frac{\partial g}{\partial x} = -\frac{1}{2\pi} \frac{x - x_0}{r^2}, & \qquad \frac{\partial g}{\partial y} = -\frac{1}{2\pi} \frac{y - y_0}{r^2}, \end{aligned} \tag{3.9}$$

are, respectively, the free-space Green's function of the two-dimensional Laplace equation and its associated gradient (e.g., [83]). Applying (3.8) on the boundary, C, we have

$$\frac{1}{2}\phi(\mathbf{x}_0) = -\int_C g(\mathbf{x}, \mathbf{x}_0)[\mathbf{n} \cdot \nabla\phi] dl(\mathbf{x}) + \int_C \phi[\mathbf{n} \cdot \nabla g(\mathbf{x}, \mathbf{x}_0)] dl(\mathbf{x}), \tag{3.10}$$

which is the integral representation used in the BEM. Figure 3.2 visualizes what a 2D domain may look like when using a BEM. In this case, the control area, A_C, is contained by a boundary, C, comprised of two closed lines, C_1 and C_2. The shaded area would represent the electric field. In this example, Eq. (3.8) represents the electric potential for the interior evaluation point, $\mathbf{x}_0$, located within A_C. Eq. (3.10) expresses the electric potential at the point, $\mathbf{x}_0$, located directly on C. The integrals on the right-hand side of each equation are performed over the segments $dl(\mathbf{x})$ comprising both C_1 and C_2 with the surface normal facing into the shaded area.

The boundary-element method is a technique for solving for the solution to a function at the boundary of a domain. If we were trying to solve for the boundary solution to ϕ in this example, we would approximate the integrals in Eq. (3.10) using a finite number of boundary-elements E_i. Under this method, Eq. (3.10) can be written as

$$\frac{1}{2}\phi(\mathbf{x}_0) = -\sum_{i=1}^{N}\int_{E_i} g(\mathbf{x},\mathbf{x}_0)[\mathbf{n}\cdot\nabla\phi]dl(\mathbf{x}) + \sum_{i=1}^{N}\int_{E_i}\phi[\mathbf{n}\cdot\nabla g(\mathbf{x},\mathbf{x}_0)]dl(\mathbf{x}), \qquad (3.11)$$

where $i = 1, ..., N$ represents the total number of elements and $\mathbf{x}$ lies on E_i. With this approximation, Gauss–Legendre quadrature is used for integration. At this stage a system of linear equations is formed and the unknown boundary values of ϕ or its derivatives are computed. Once the boundary solution is known, one has the option of using Eq. (3.8) to find the value of ϕ at any point within A_C explicitly.

3.2.2 Three-dimensional formulation

In a three-dimensional domain, the electric potential at a point $\mathbf{x}_0$ in the interior of the flow field, $\phi(\mathbf{x}_0)$, takes on the following form,

$$\phi(\mathbf{x}_0) = -\int_D g(\mathbf{x}_0,\mathbf{x})[\mathbf{n}\cdot\nabla\phi(\mathbf{x})]dS(\mathbf{x}) + \int_D \phi(\mathbf{x})[\mathbf{n}\cdot\nabla g(\mathbf{x}_0,\mathbf{x})]dS(\mathbf{x}), \qquad (3.12)$$

where $\mathbf{n}$ is the surface normal pointing into the flow field enclosed by all surfaces, D. The function g is the free-space Green's function for the three-dimensional Laplace equation, together with its gradient, ∇g, given respectively by

$$g(\mathbf{x},\mathbf{x}_0) = \frac{1}{4\pi r},$$

and

$$\frac{\partial g}{\partial x} = -\frac{1}{4\pi}\frac{x-x_0}{r^3}, \qquad \frac{\partial g}{\partial y} = -\frac{1}{4\pi}\frac{y-y_0}{r^3}, \qquad \frac{\partial g}{\partial z} = -\frac{1}{4\pi}\frac{z-z_0}{r^3}, \qquad (3.13)$$

where $r = |\mathbf{x} - \mathbf{x}_0|$.

If the point $\mathbf{x}_0$ lies on the boundary, D, the integral equation becomes

$$\frac{1}{2}\phi(\mathbf{x}_0) = -\int_D g(\mathbf{x}_0, \mathbf{x})[\mathbf{n} \cdot \nabla\phi(\mathbf{x})]dS(\mathbf{x}) + \int_D \phi(\mathbf{x})[\mathbf{n} \cdot \nabla g(\mathbf{x}_0, \mathbf{x})]dS(\mathbf{x}). \qquad (3.14)$$

The discretization process in 3D is similar to that detailed for two dimensions. By approximating the integrals over D as sums of integrals across surface elements, E_i, we can re-write Eq. (3.14) as

$$\frac{1}{2}\phi(\mathbf{x}_0) = -\sum_{i=1}^{N}\int_{E_i} g(\mathbf{x}, \mathbf{x}_0)[\mathbf{n} \cdot \nabla\phi]dS(\mathbf{x}) + \sum_{i=1}^{N}\int_{E_i} \phi[\mathbf{n} \cdot \nabla g(\mathbf{x}, \mathbf{x}_0)]dS(\mathbf{x}), \qquad (3.15)$$

where $i = 1, ..., N$ represents the total number of elements and $\mathbf{x}$ lies on E_i.

3.3 Boundary-integral formulation for Stokes equation

The fluid is assumed to be Newtonian and incompressible, and the Reynolds number is small so that the fluid inertia can be ignored. Bulk flow is then governed by the Stokes and continuity equations

$$-\nabla p + \mu\nabla^2\mathbf{u} = 0, \qquad \nabla \cdot \mathbf{u} = 0, \qquad (3.16)$$

where p, $\mathbf{u}$, and μ are the pressure, velocity, and viscosity, respectively. Although there is no time dependence visible in Eq. (3.16), a time evolution can exist based on the motion of a particle boundary. For this reason, the simulations are said to be quasi-steady. A derivation of the boundary-integral representing Stokes flow analogous to that presented in section 3.1 can be found in [83].

3.3.1 Two-dimensional formulation

To solve the flow in two dimensions, we use the boundary-integral formulation for the Stokes equation and express $\mathbf{u}$ at the point $\mathbf{x}_0$ that lies inside the fluid,

$$u_j(\mathbf{x}_0) = -\frac{1}{4\pi\mu}\int_C G_{ij}(\mathbf{x},\mathbf{x}_0)\, f_i(\mathbf{x})\mathrm{d}l(\mathbf{x}) + \frac{1}{4\pi}\int_C u_i(\mathbf{x})\, T_{ijk}(\mathbf{x},\mathbf{x}_0)\, n_k(\mathbf{x})\, \mathrm{d}l(\mathbf{x}), \quad (3.17)$$

where C represents the boundary of the domain, f_i is the traction, and

$$G_{ij}(\mathbf{x},\mathbf{x}_0) = -\delta_{ij}\ln r + \frac{\hat{x}_i\hat{x}_j}{r^2}, \qquad T_{ijk}(\mathbf{x},\mathbf{x}_0) = -4\,\frac{\hat{x}_i\hat{x}_j\hat{x}_k}{r^4}, \quad (3.18)$$

are, respectively, the free-space Green's function of two-dimensional Stokes flow and associated stress tensors, $\hat{\mathbf{x}} = \mathbf{x} - \mathbf{x}_0$, and $r = |\hat{\mathbf{x}}|$ (e.g., [67]). If the point $\mathbf{x}_0$ lies on the boundary C, the integral equation takes on the form,

$$\frac{1}{2}u_j(\mathbf{x}_0) = -\frac{1}{4\pi\mu}\int_C G_{ij}(\mathbf{x},\mathbf{x}_0)\, f_i(\mathbf{x})\mathrm{d}l(\mathbf{x}) + \frac{1}{4\pi}\int_C u_i(\mathbf{x})\, T_{ijk}(\mathbf{x},\mathbf{x}_0)\, n_k(\mathbf{x})\, \mathrm{d}l(\mathbf{x}). \quad (3.19)$$

As with the integral equations representing electric potential, the integrals in Eq. (3.19) can be approximated over a finite number of elements to develop a system of linear equations.

3.3.2 Three-dimensional formulation

When working with a three-dimensional computational domain, the formulation for $\mathbf{u}$ at the point $\mathbf{x}_0$ inside of the fluid takes on the following form,

$$u_j(\mathbf{x}_0) = -\frac{1}{8\pi\mu}\int_D G_{ji}(\mathbf{x}_0,\mathbf{x})\, f_i(\mathbf{x})dS(\mathbf{x}) + \frac{1}{8\pi}\int_D u_i(\mathbf{x})T_{ijk}(\mathbf{x},\mathbf{x}_0)n_k(\mathbf{x})dS(\mathbf{x}), \quad (3.20)$$

where $\mathbf{u} = (u_x, u_y, u_z)$ and $\mathbf{f} = \boldsymbol{\sigma}\cdot\mathbf{n}$ is the component of the hydrodynamic traction, and G and T are the free-space Green's function and associated stress tensor for Stokes

flow, given by

$$G_{ij}(\mathbf{x}-\mathbf{x}_0) = \frac{\delta_{ij}}{r} + \frac{\hat{x}_i\hat{x}_j}{r^3}, \qquad T_{ijk}(\mathbf{x}-\mathbf{x}_0) = -6\,\frac{\hat{x}_i\hat{x}_j\hat{x}_k}{r^5}, \tag{3.21}$$

and again, $r = |\mathbf{x}-\mathbf{x}_0|$. Note that the dummy indices i, j, and k rotate among the components x, y, and z. If the point $\mathbf{x}_0$ lies on the boundary D, the integral equation takes on the form

$$\frac{1}{2}u_j(\mathbf{x}_0) = -\frac{1}{8\pi\mu}\int_D G_{ji}(\mathbf{x}_0,\mathbf{x})\,f_i(\mathbf{x})dS(\mathbf{x}) + \frac{1}{8\pi}\int_D u_i(\mathbf{x})T_{ijk}(\mathbf{x},\mathbf{x}_0)n_k(\mathbf{x})dS(\mathbf{x}). \tag{3.22}$$

After discretization, Eq. (3.22) will be used to formulate the algebraic system to obtain the hydrodynamic traction $\mathbf{f}$ on the particle and cylinder surfaces (note that the fluid velocity at these surfaces will be based on the slip velocity and can be obtained, once ϕ and its gradient are available). Once $\mathbf{f}$ is obtained, the fluid velocity at any interior point in the flow can be calculated by evaluating Eq.(3.20) in post-processing.

3.4 Integral identities

An issue arises with use of the integral equations pertaining to the singularity of the integrals. More specifically, as the integration point, $\mathbf{x}$, approaches the evaluation point $\mathbf{x}_0$ on a surface, the integrands in the boundary-integral formulation exhibit singularity and thus require special numerical treatment. In two dimensions, we can subtract the singularities and integral analytically [83]. In three dimensions, to deal with the singularity found in the single-layer potential terms, a straightforward coordinate transformation into local polar coordinates is used [83]. For the double-layer potential, a set of integral identities are utilized to subtract the singularity. Therefore, it is of interest to identify the applicable integral identities here for use in each study. For the Laplace

equation we have the following identity,

$$\int_D [\mathbf{n}(\mathbf{x}) \cdot \nabla g(\mathbf{x}, \mathbf{x}_0)] dS(\mathbf{x}) = \begin{cases} 1 \text{ when } \mathbf{x}_0 \text{ is inside } V_c \\ \frac{1}{2} \text{ when } \mathbf{x}_0 \text{ is on } D \\ 0 \text{ when } \mathbf{x}_0 \text{ is outside } V_c \end{cases} \tag{3.23}$$

when the surface normal, **n**, points into the control volume V_c bounded by the surface, D. If the surface normal were directed outside of the the control volume or area, the sign of the terms on the right side would be reversed.

The stress tensor of Green's functions satisfies the following identity,

$$\frac{1}{8\pi} \int_D T_{ijk}(\mathbf{x}, \mathbf{x}_0) n_k(\mathbf{x}) dS(\mathbf{x}) = \begin{cases} \delta_{ij} \text{ when } \mathbf{x}_0 \text{ is inside } V_c \\ \frac{1}{2}\delta_{ij} \text{ when } \mathbf{x}_0 \text{ is on } D \\ 0 \text{ when } \mathbf{x}_0 \text{ is outside } V_c \end{cases} \tag{3.24}$$

when the surface normal, **n**, points into the control volume V_c bounded by the surface, D. Again, if the surface normal were directed outside of the the control volume or area, the sign of the terms on the right side would be reversed.

Two identities used to simplify the expressions for translational and rotational rigid-body velocity of the particle in 2D are expressed as [67],

$$\begin{aligned} \int_C T_{ijk}(\mathbf{x}, \mathbf{x}_0) n_k(\mathbf{x}) dl(\mathbf{x}) &= -2\pi\delta_{ij} \\ \epsilon_{ilm} \int_C (x - x_c)_m T_{ijk}(\mathbf{x}, \mathbf{x}_0) n_k(\mathbf{x}) dl(\mathbf{x}) &= -2\pi\epsilon_{jlm}(x_0 - x_c)_m. \end{aligned} \tag{3.25}$$

where **n** is the surface normal that is directed outside of the area enclosed by the surface, C. An equivalent set of identities for three dimensions takes on the following form,

$$\begin{aligned} \int_D T_{ijk}(\mathbf{x}, \mathbf{x}_0) n_k(\mathbf{x}) dS(\mathbf{x}) &= -4\pi\delta_{ij} \\ \epsilon_{ilm} \int_D (x - x_c)_m T_{ijk}(\mathbf{x}, \mathbf{x}_0) n_k(\mathbf{x}) dS(\mathbf{x}) &= -4\pi\epsilon_{jlm}(x_0 - x_c)_m. \end{aligned} \tag{3.26}$$

The same rules between the direction of the surface normal and the sign of the right-hand side apply to these identities as well.

CHAPTER IV

ELECTROPHORETIC MOBILITY OF A COLLOIDAL CYLINDER BETWEEN PARALLEL WALLS

4.1 Background

It is well known that in an unbounded flow, the electrophoretic motion of a non-conducting particle with arbitrary shape is purely translational, and the velocity can be described by Smoluchowski's formula, Eq. (2.6). However, when the particle is near a wall, its mobility may change significantly due to modification of the electric field by the presence of the wall. In fact, it was found that the translational velocity of a spherical particle is increased as the particle is sufficiently close to the wall [59, 61, 84]. This result is in sharp contrast to the intuitive idea that when compared to a particle in unbounded flow, a particle travelling along a wall would be slowed down due to the increased viscous force, as seen in the Stokes mobility problem.

Electrophoretic motion of a particle near boundaries has been studied for various configurations. The translation of a spherical particle near a wall was analyzed by Keh & Chen [59] for insulating surfaces using the eigenfunction series, and their study was later complemented by Yariv & Brenner [62] for closer particle-wall separation using an asymptotic expansion. Other configurations include spheroids, cylinders, or ellipsoids in confined environments such as cylindrical pores [61, 65], spherical cavities [85, 86], and complex channels [64, 66]. Despite these works, the electrophoretic mobility of an infinite cylindrical particle bounded by two parallel walls and translating perpendicular to its own axis has not been reported. The problem emulates the situation where a slender particle is moving sideways in a microchannel. Keh *et al.* [87] derived an analytical solution for an infinite, insulating cylinder electrophoretically moving along

a single non-conducting wall and found that the velocity grows unboundedly as the cylinder-wall separation approaches zero. It is not clear yet how the cylinder's mobility would change if it is bounded from both sides. One relevant situation to this issue is the electrophoresis of a spherical particle moving between two parallel walls, which was studied analytically by Unni *et al.* [88] for arbitrary eccentricity. In Unni *et al.*, the particle's translation is found to be enhanced when both walls are close to the particle, which implies that the increasing electrophoretic effect has overcome the hydrodynamic retardation for the close particle-wall separation. However, this phenomenon may not occur in the two-dimensional case, where the closely fitting cylinder is subject to a "piston effect" and will experience much higher hydrodynamic resistance than the spherical particle in the channel. In this sense, the confined cylinder is more like the sphere in a narrow cylindrical pore, whose electrophoretic mobility decreases significantly when the particle-to-pore radius ratio approaches to unity [61].

4.2 Problem specification

In this study, we consider a cylindrical particle suspended in an aqueous electrolyte solution between two parallel walls, as shown in Figure 4.1. The axis of the cylinder is parallel to the walls and is perpendicular to the uniform, external electric field, E^{∞}. The problem configuration is two-dimensional, where the particle may rotate about the z axis while translating in the x direction. Both the particle and the channel walls are non-conducting and carry uniform surface charges, which are characterized by their respective zeta potentials, ζ_p and ζ_w. A positively charged surface has a positive value of zeta potential. The thin-EDL approximation is utilized so that Eq. (2.4) governs electric potential. The homogeneous Neumann boundary condition, $\partial\phi/\partial\mathbf{n} = 0$, is applied at the particle surface and channel walls [62] because both are nonconducting. Note that $\mathbf{n}$ is the surface normal and points into the flow. Dielectrophoresis is not considered in this study.

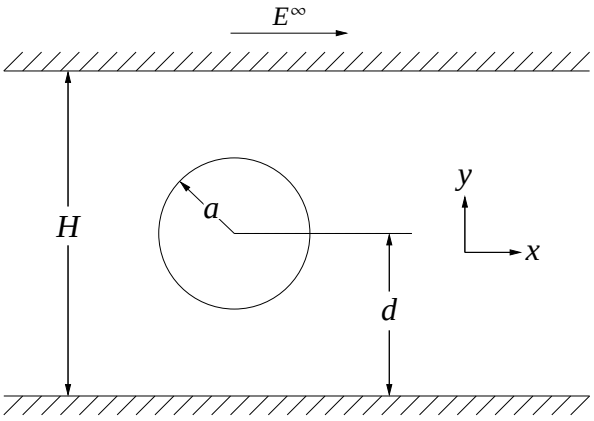

Figure 4.1: Schematic of the cylindrical particle suspended in an aqueous solution between two parallel walls.

Bulk fluid flow is governed by the Stokes and continuity equations, Eq. (3.16). From the thin-EDL assumption, Eq. (2.3) is used to describe the slip velocity next to the particle or channel walls. The slip velocity is relative to the solid surfaces and proportional to the local tangential gradient of the electric potential,

$$\mathbf{u}^S = \frac{\varepsilon_m \zeta}{\mu}(\mathbf{I} - \mathbf{nn}) \cdot \nabla\phi, \tag{4.1}$$

where $\zeta = \zeta_p$ or ζ_w is the zeta potential on either the particle surface or channel wall, and $(\mathbf{I} - \mathbf{nn})$ is a surface gradient operator. For clarification, using an arbitrary vector $\mathbf{f}$, the operator provides the following adjustment,

$$(\mathbf{I} - \mathbf{nn}) \cdot \mathbf{f} = \mathbf{f} - \mathbf{nn}^\intercal \mathbf{f} = \mathbf{f} - \mathbf{n}(\mathbf{n} \cdot \mathbf{f}) = \mathbf{f} - |\mathbf{f}_n|\mathbf{n} = \mathbf{f}_\tau \tag{4.2}$$

in order to yield the tangential component. In the laboratory coordinates, the fluid velocity at the particle surface is the combination of the rigid body motion of the particle and the slip velocity,

$$\mathbf{u}(\mathbf{x}) = \mathbf{u}^B + \mathbf{u}^S = \mathbf{u}_c + \omega \mathbf{e}_z \times (\mathbf{x} - \mathbf{x}_c) + \mathbf{u}^S, \tag{4.3}$$

where $\mathbf{x}$ is a point on the particle surface, $\mathbf{x}_c$ and $\mathbf{u}_c$ are the position and velocity of the centroid of the particle, ω is the rotational speed of the particle, $\mathbf{e}_z$ is the unit vector in z, and $\mathbf{u}^B = \mathbf{u}_c + \omega \mathbf{e}_z \times (\mathbf{x} - \mathbf{x}_c)$ is the velocity of the point $\mathbf{x}$ due to the rigid body motion. The particle is assumed to be neutrally buoyant in the fluid, and its inertia can also be ignored. Therefore, both the total traction and torque exerted on the particle vanish,

$$\int_P \mathbf{f}\, \mathrm{d}l = \mathbf{0}, \qquad \int_P (\mathbf{x} - \mathbf{x}_c) \times \mathbf{f}\, \mathrm{d}l = \mathbf{0}, \tag{4.4}$$

where $\mathbf{f} = \boldsymbol{\sigma} \cdot \mathbf{n} = (f_x, f_y)$ is the local traction, and the integrations are performed over the particle contour, P. At the two channel ends, which are far away from the particle, we assume that flow is fully developed so that the velocity no longer depends on x.

4.3 Formulation

Note that the Laplace equation solution is independent of the solution of Stokes flow while the latter depends on the former through the slip velocity boundary condition Eq. (4.1). Therefore, the Laplace and Stokes equations can be solved sequentially.

In this study, the electric potential, ϕ, is decomposed into a combination of the background potential, $\phi^\infty = -E^\infty x$, and the disturbance potential generated due to the presence of the particle, ϕ^D, so that $\phi = \phi^\infty + \phi^D$. Following the 2D formulation from Chapter III, the disturbance potential at a point, $\mathbf{x}_0$ on the boundary of the flow field can be written as

$$\frac{1}{2}\phi^D(\mathbf{x}_0) = -\int_C g(\mathbf{x}, \mathbf{x}_0)[\mathbf{n} \cdot \nabla \phi^D] dl(\mathbf{x}) + \int_C \phi^D [\mathbf{n} \cdot \nabla g(\mathbf{x}, \mathbf{x}_0)] dl(\mathbf{x}), \tag{4.5}$$

where the boundary, C, consists of the walls and particle surface.

Similarly, we decompose the fluid velocity into the background velocity,

$$u^\infty = -\frac{\varepsilon \zeta_w E^\infty}{\mu}, \tag{4.6}$$

which is the uniform electroosmotic flow in the absence of the particle, and the disturbance velocity generated by the particle, $\mathbf{u}^D$, so that $\mathbf{u}^D = u^\infty \mathbf{e}_x + \mathbf{u}^D$. The disturbance velocity vanishes as x approaches infinity. To compute the disturbance velocity, we use the formulation from Chapter III and express $\mathbf{u}^D$ at the point $\mathbf{x}_0$ that lies on the boundary, C, in the following form,

$$\frac{1}{2}\mathbf{u}^D(\mathbf{x}_0) = -\frac{1}{4\pi\mu}\int_C f_i^D(\mathbf{x})G_{ij}(\mathbf{x},\mathbf{x}_0)\mathrm{d}l(\mathbf{x}) + \frac{1}{4\pi\mu}\int_C u_i^D(\mathbf{x})T_{ijk}(\mathbf{x},\mathbf{x}_0)n_k(\mathbf{x})\mathrm{d}l(\mathbf{x}), \quad (4.7)$$

where $\mathbf{f}^D$ is the disturbance traction. If we break up the integrals to represent the total boundary C, with a sum of integrals over the particle surface, P, and channel walls, W, then we can write the previous equation as,

$$\begin{aligned}\frac{1}{2}\mathbf{u}^D(\mathbf{x}_0) &= -\frac{1}{4\pi\mu}\int_P f_i^D(\mathbf{x})G_{ij}(\mathbf{x},\mathbf{x}_0)\mathrm{d}l(\mathbf{x}) - \frac{1}{4\pi\mu}\int_W f_i^D(\mathbf{x})G_{ij}(\mathbf{x},\mathbf{x}_0)\mathrm{d}l(\mathbf{x}) \quad (4.8)\\ &+ \frac{1}{4\pi}\int_P u_i^D(\mathbf{x})T_{ijk}(\mathbf{x},\mathbf{x}_0)n_k(\mathbf{x})\mathrm{d}l(\mathbf{x}) + \frac{1}{4\pi}\int_W u_i^D(\mathbf{x})T_{ijk}(\mathbf{x},\mathbf{x}_0)n_k(\mathbf{x})\mathrm{d}l(\mathbf{x}).\end{aligned}$$

To simplify the integral expressions, we use $\mathcal{S}$ and $\mathcal{D}$ to represent the single-layer and double-layer potentials respectively in the previous equation. Each of the components are given as,

$$\begin{aligned}\mathcal{S}_j(\mathbf{x}_0,\mathbf{f},C) &\equiv \int_C f_i(\mathbf{x})\, G_{ij}(\mathbf{x},\mathbf{x}_0)\, \mathrm{d}l(\mathbf{x}),\\ \mathcal{D}_j(\mathbf{x}_0,\mathbf{u},C) &\equiv \int_C u_i(\mathbf{x})\, T_{ijk}(\mathbf{x},\mathbf{x}_0)\, n_k(\mathbf{x})\, \mathrm{d}l(\mathbf{x}). \quad (4.9)\end{aligned}$$

Using this form, Eq. (4.8) can be written as,

$$\begin{aligned}\frac{1}{2}\mathbf{u}^D(\mathbf{x}_0) = -\frac{1}{4\pi\mu}&\left[\mathcal{S}(\mathbf{x}_0,\mathbf{f}^D,P) + \mathcal{S}(\mathbf{x}_0,\mathbf{f}^D,W)\right]\\ &+\frac{1}{4\pi}\left[\mathcal{D}(\mathbf{x}_0,\mathbf{u}^D,P) + \mathcal{D}(\mathbf{x}_0,\mathbf{u}^D,W)\right]. \quad (4.10)\end{aligned}$$

We expand conditions for the particle by substituting $\mathbf{f}^D = \mathbf{f} - \mathbf{f}^\infty$ into the first term

and $\mathbf{u}^D = \mathbf{u} - \mathbf{u}^\infty = \mathbf{u}^B + \mathbf{u}^S - \mathbf{u}^\infty$ into the third term on the right-hand side of (4.10).

$$\begin{aligned}\frac{1}{2}\mathbf{u}^D(\mathbf{x}_0) = &-\frac{1}{4\pi\mu}\left[\mathcal{S}(\mathbf{x}_0, (\mathbf{f}-\mathbf{f}^\infty), P) + \mathcal{S}(\mathbf{x}_0, \mathbf{f}^D, W)\right] \\ &+\frac{1}{4\pi}\left[\mathcal{D}(\mathbf{x}_0, (\mathbf{u}^B + \mathbf{u}^S - \mathbf{u}^\infty), P) + \mathcal{D}(\mathbf{x}_0, \mathbf{u}^D, W)\right]. \end{aligned} \tag{4.11}$$

Applying the reciprocal relation [67] to the background flow we obtain the following,

$$-\frac{1}{4\pi\mu}\mathcal{S}(\mathbf{x}_0, \mathbf{f}^\infty, P) + \frac{1}{4\pi}\mathcal{D}(\mathbf{x}_0, \mathbf{u}^\infty, P) = \begin{cases} \frac{1}{2}\mathbf{u}^\infty(\mathbf{x}_0) \text{ when } \mathbf{x}_0 \text{ is on } P \\ 0 \text{ when } \mathbf{x}_0 \text{ is on } W. \end{cases} \tag{4.12}$$

Applying Eq. (3.25) for 2D rigid body motion provides the following relationship,

$$\frac{1}{4\pi}\mathcal{D}(\mathbf{x}_0, \mathbf{u}^B, P) = -\frac{1}{2}\mathbf{u}^B(\mathbf{x}_0). \tag{4.13}$$

Combining the simplifications from Eqs. (4.12) and (4.13) with Eq. (4.11), we can write the final integral equation for when $\mathbf{x}_0$ is located on the particle surface, P,

$$\begin{aligned}\mathbf{u}^B(\mathbf{x}_0) + \frac{1}{2}\mathbf{u}^S(\mathbf{x}_0) - \mathbf{u}^\infty &= -\frac{1}{4\pi\mu}\left[\mathcal{S}(\mathbf{x}_0, \mathbf{f}, P) + \mathcal{S}(\mathbf{x}_0, \mathbf{f}^D, W)\right] \\ &\quad +\frac{1}{4\pi}\left[\mathcal{D}(\mathbf{x}_0, \mathbf{u}^S, P) + \mathcal{D}(\mathbf{x}_0, \mathbf{u}^D, W)\right]. \end{aligned} \tag{4.14}$$

Apply the same simplifications and write the final integral equation for when $\mathbf{x}_0$ is located on the wall, W, and we get,

$$\begin{aligned}\frac{1}{2}\mathbf{u}^D(\mathbf{x}_0) = &-\frac{1}{4\pi\mu}\left[\mathcal{S}(\mathbf{x}_0, \mathbf{f}, P) + \mathcal{S}(\mathbf{x}_0, \mathbf{f}^D, W)\right] \\ &+\frac{1}{4\pi}\left[\mathcal{D}(\mathbf{x}_0, \mathbf{u}^S, P) + \mathcal{D}(\mathbf{x}_0, \mathbf{u}^D, W)\right]. \end{aligned} \tag{4.15}$$

To solve the integral equations (4.5), (4.14), and (4.15), the wall and particle contours are discretized by a non-uniform mesh consisting of linear or arc segments. The unknown variables, ϕ^D on both P and W, $\mathbf{f}$ on P, and $\mathbf{f}^D$ on W, are defined at the ele-

ment centers. The integral equation for the disturbance potential, (4.5), is solved first. Then, the slip velocity at the particle surface and walls, $\mathbf{u}^S$, is calculated from Eq. (4.1), and the disturbance velocity at the walls, $\mathbf{u}^D$, is obtained by subtracting the background velocity,

$$\mathbf{u}^D = \mathbf{u}^S - \mathbf{u}^\infty = \frac{\varepsilon\zeta_w}{\mu}(\mathbf{I} - \mathbf{nn}) \cdot \nabla\phi^D, \tag{4.16}$$

where $\mathbf{u}^S$ is the total slip velocity due to both the background potential and the disturbance potential. Finally, (4.14) and (4.15) are solved together with the unknown translational and rotational velocities of the particle. To match the total number of unknowns, two additional equations from (4.4) expressing vanishing condition of the total traction in x and the total torque on the particle are appended to the linear algebraic system. In all the equations, the integrals are carried out using the Gauss–Legendre quadratures over each element. The singularities of the singular elements are subtracted off and computed analytically.

Calculation of the slip velocity in (4.1) requires evaluation of the tangential derivative of the electric potential. To do this, we compute ϕ at the two end nodes of each element after solving (4.5) and then approximate the tangential derivative of ϕ at the element center using a second-order finite-difference scheme. The channel is truncated at $x = \pm L/2$ with the particle located at $x = 0$. We have chosen $L = 30a$ for all simulations. One difficulty arises as the channel width approaches to the particle size, as an exceedingly long domain is needed for $\mathbf{u}^D$ to decay to an acceptable limit. To deal with the problem, we require that the flow be unidirectional at the channel inlet/outlet. Consequently, u_y and f_x are zero at the inlet/outlet, but u_x and f_y are unknown. These additional variables are solved together with the integral equations by including the inlet and outlet in the integration contours. We point out that the non-zero disturbance velocity at the inlet and outlet still satisfies the boundary condition at the walls, Eq. (4.16). That is, $\mathbf{u}^D$ is zero at the four corners of the channel since the disturbance potential and

its gradient vanish at those locations.

4.4 Validation

In order to validate the accuracy of the two-dimensional BEM code, we first consider electrophoretic mobility of a cylindrical particle in a semi-infinite flow driven by electroosmosis, that is, the uniform flow due to a non-zero charge on the *single* wall. The analytical solution of this two-dimensional problem was reported by Keh *et al.* [87]. Figure 4.2 plots the normalized translational and rotational velocities of the cylinder, $\hat{U}_p = \frac{U_p \mu}{\varepsilon(\zeta_p - \zeta_w)E^\infty}$, and $\hat{\omega} = \frac{\omega \mu a}{\varepsilon(\zeta_p - \zeta_w)E^\infty}$, where U_p and ω are the corresponding dimensional quantities in the laboratory coordinates. The results are depicted as functions of the ratio between the particle radius and the distance from the particle center to the lower wall, a/d. It can be seen that the present numerical results are in excellent agreement with the theoretical prediction. The smallest particle-wall separation in the figure is $0.01a$, i.e., $a/d \approx 0.99$, for which we used 256 uniform elements on the particle and 192 non-uniform elements on the wall. The comparison of the numerical calculation with the analytical result for a few selected cases is also provided in Table 4.1, where the difference is up to the second decimal point for the closest proximity.

When the particle is far away from the wall, the translational velocity approaches the value corresponding to the electrophoretic velocity of the particle in an infinite flow, $\varepsilon(\zeta_p - \zeta_w)E^\infty/\mu$, and the rotational velocity approaches zero, as expected. As the particle comes nearly in contact with the wall, both the translational and rotational velocities grow to infinity, which is in sharp contrast with a purely hydrodynamic flow where the particle velocity is reduced by the wall due to viscous retardation. A similar enhancing effect of the wall on the electrophoretic mobility of a nearby spherical particle was reported in Keh & Chen [59] and Yariv & Brenner [62]. As pointed out by them, the phenomenon is caused by the intensified electric field in the narrow gap, which is dominant over the viscous effect and introduces a high slip between the particle and fluid in

(*a*)

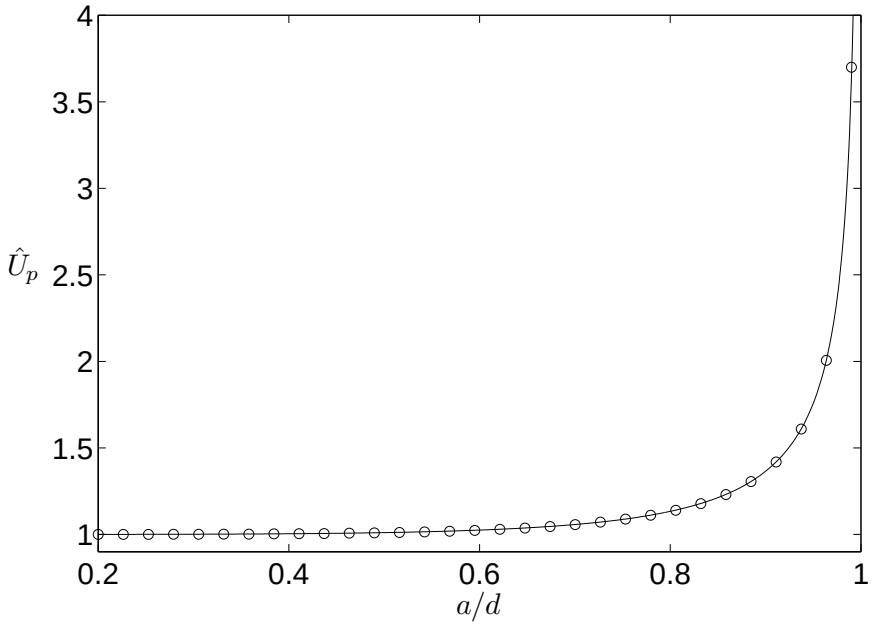

(*b*)

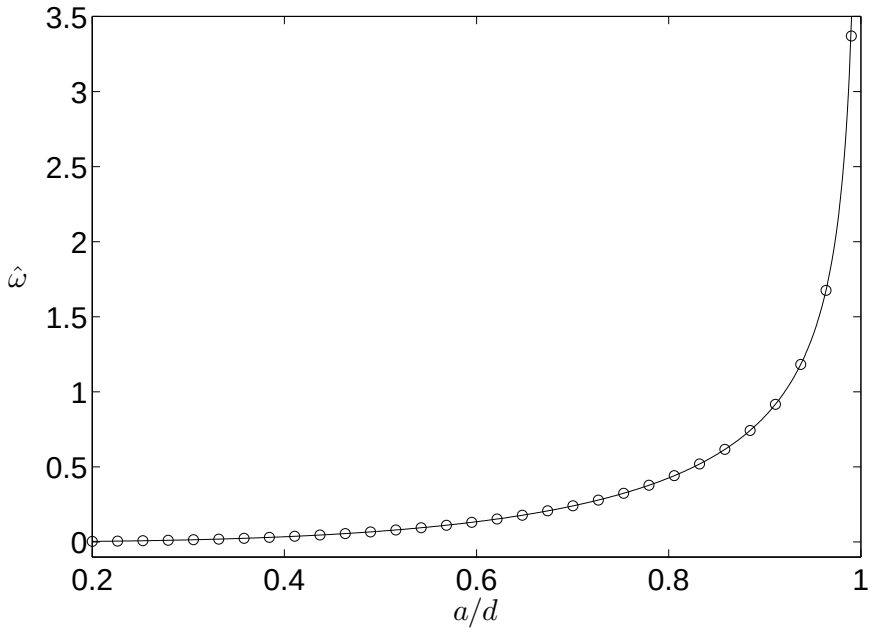

Figure 4.2: The normalized (a) translational and (b) rotational velocities of the cylinder as functions of a/d computed from Keh *et al.* [87] (solid line) and the BEM used in the current study (markers).

the gap.

Table 4.1: Comparison of the normalized translational and rotational velocities of the cylinder as functions of a/d computed from Keh *et al.* [87] and the BEM used in the current study.

	Current study		Keh *et al.* [87]	
a/d	$\hat{U}_p$	$\hat{\omega}$	$\hat{U}_p$	$\hat{\omega}$
0.20	1.0000	0.0041	1.0002	0.0041
0.60	1.0244	0.1351	1.0250	0.1350
0.80	1.1328	0.4267	1.1333	0.4267
0.90	1.3648	0.8360	1.3650	0.8362
0.95	1.7577	1.3720	1.7574	1.3729
0.98	2.6120	2.3620	2.6121	2.3648
0.99	3.5963	3.4464	3.6149	3.4391

4.5 Results

Next, we consider a particle bounded by two walls. Figure 4.3 shows the particle's translational and rotational velocities at varying distances between the two walls at four reduced channel widths, H/a. As in other two- and three-dimensional particle/channel configurations (e.g., [59, 61, 62, 87]) where the EDL is assumed to be thin, we also found that U_p and ω are proportional to the difference between the zeta potentials on the particle and wall, $\zeta_p - \zeta_w$. Therefore, the same normalizations for U_p and ω as in the single wall case are used here. To better display the results, the eccentric position of the particle has been scaled by $H - 2a$.

For wide channels such as $H/a = 20$, the reduced translational velocity and rotational velocity are nearly unity and zero, respectively, for a wide range of particle locations. This reflects the situation of infinite flow and means that the wall effect is negligible. When the particle approaches either one of the two walls, the particle behaves as it would if it were brought within close proximity of only a single wall and the effect of the other wall is negligible.

At smaller values of H/a, the effect of both channel walls on the particle motion

(*a*)

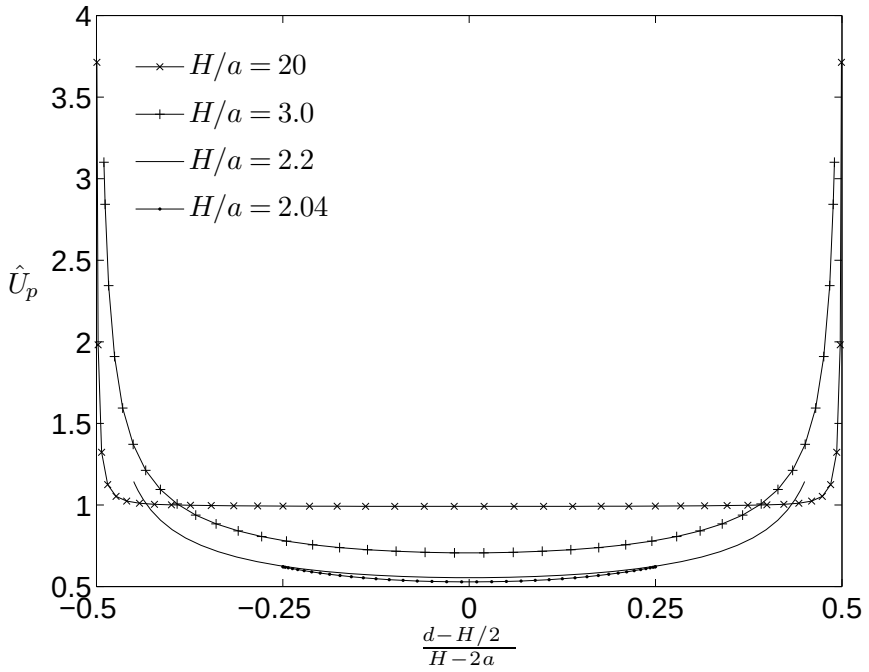

(*b*)

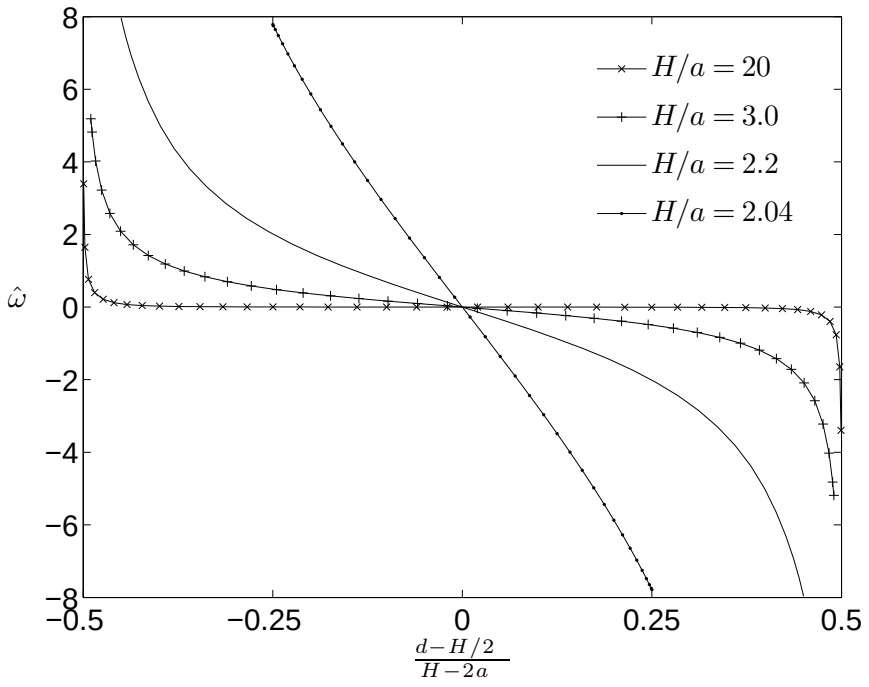

Figure 4.3: The translation (*a*) and rotation (*b*) of the particle as functions of the normalized eccentricity.

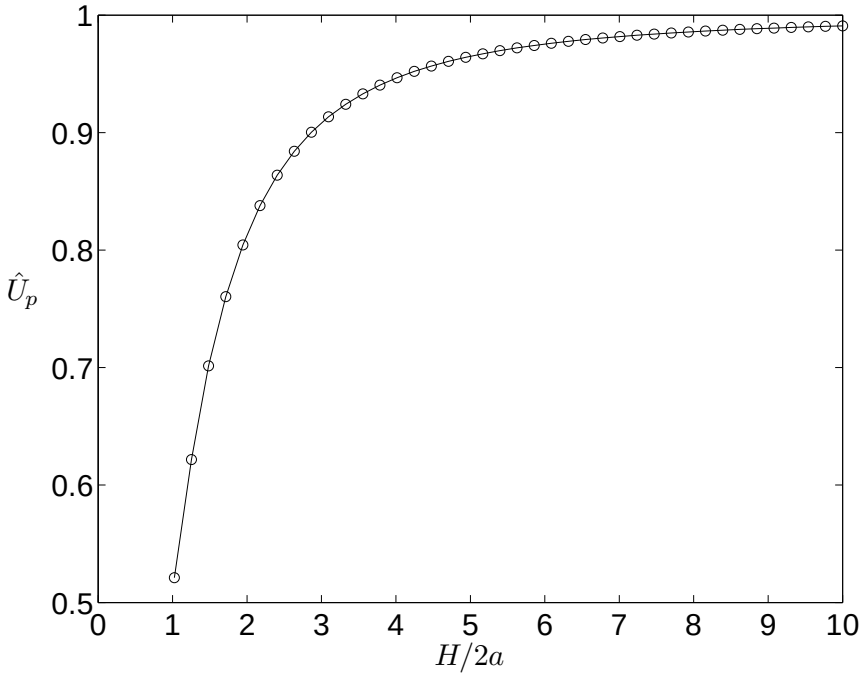

Figure 4.4: The translation of the particle located at the centerline of the channel as a function of H/a.

becomes evident. When the particle is located away from the walls, its translational velocity is lower compared to the wide channel case, while its rotational velocity is higher. As the particle approaches either wall, both the translational and rotational velocities increase monotonically. The closest particle-wall distance here is 1% of the particle radius. Due to the deteriorated numerical accuracy, we were unable to verify if the particle's velocities would go to infinity when the particle further approaches the wall.

To see how the channel width affects the particle motion at the symmetric configuration, in Figure 4.4 we plot the reduced velocity against $H/(2a)$ for the particle located at the centerline of the channel. The graph shows that, as the channel approaches the same size of the particle, the translational velocity approaches a value which is around 53% of the unbounded case. This behavior is in contrast with that of the corresponding spherical particle traveling along the centerline of the channel. According to the analytical result of Unni *et al.* [88], the normalized translational velocity of the sphere

decreases slightly as $H/(2a)$ goes from infinity down to around 1.25, and then it starts to increase instead as $H/(2a)$ is further reduced. The translation grows by around 70% when $H/(2a)$ approaches unity.

The reduced mobility of the cylindrical particle in a narrow channel can be understood from the opposing effects of the electrophoresis and viscosity. For a wide channel relative to the particle size, the particle motion induces little friction anywhere between the fluid and the channel walls except within the gap regions, and the mass flow caused by the particle translation can be easily offset by the reversal flow through at least one of the two particle-wall gaps. Therefore, if the particle is close to either of the walls in a wide channel, the intensified electric field in the smaller gap dominates over the viscous resistance, and as a result, the particle translation is enhanced. When the channel becomes narrow and its width comparable to the particle diameter, due to the friction in the small gaps on both sides of the particle, the amount of the reversal flow is restricted. The particle's translation tends to induce a net flow in the channel due to the mass conservation, but the net flow is subject to the friction between the fluid and entire channel. The narrower the channel is, the stronger the frictional effect becomes. For a particle near the centerline of the channel, the frictional resistance is of the same order as the electric force. Therefore, the particle velocity approaches a limiting value as shown in Figure 4.4. The "piston effect" is similar to the spherical particle in a cylindrical pore analyzed in Keh & Chiou [89] and Yariv & Brenner [61], where they found that the particle also approaches to a finite velocity as the diameter of the pore becomes increasingly close to that of the particle. In comparison, for a spherical particle in the channel with infinite span, flow can go around the particle easily even when the particle is tightly bounded by the walls. As a result, the electrical force outgrows the hydrodynamic retardation, and the particle's mobility is enhanced due to the comprehensive wall effect, as shown in Unni *et al.* [88].

Note that even though the particle's translation is reduced when the channel becomes narrower, its rotation is not. The rotation is caused by the necessary slip velocity

(*a*)

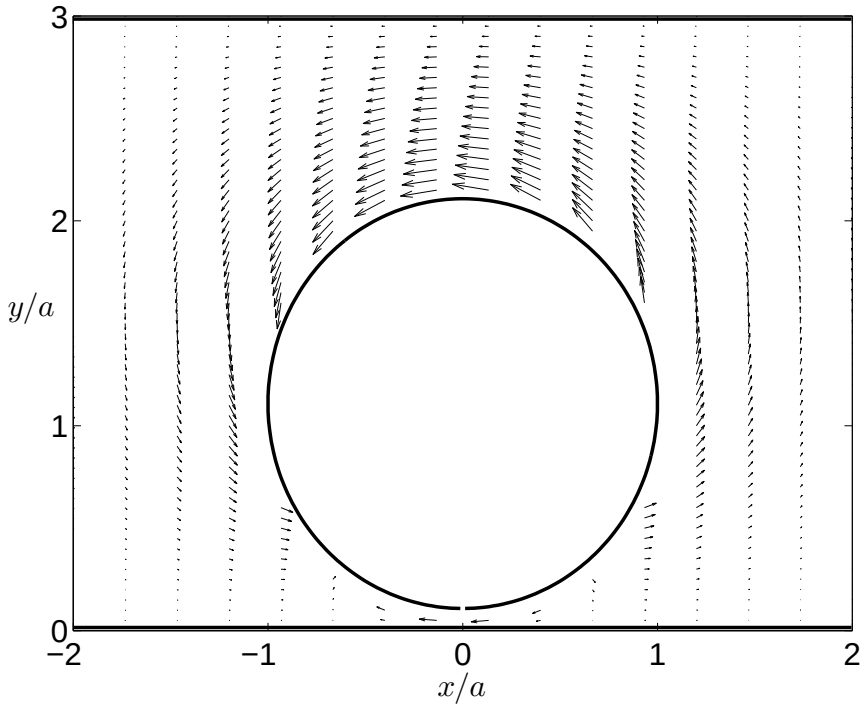

(*b*)

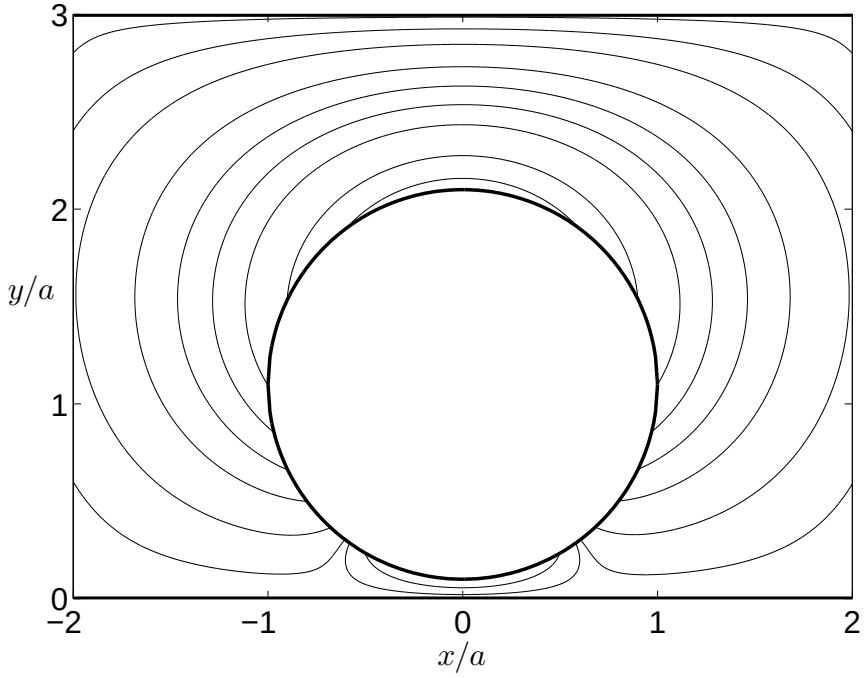

Figure 4.5: (*a*) The flow field and (*b*) streamline plots for $H/a = 3$, $d/a = 1.1$, and $\zeta_w = 0$. The particle is moving from left to right and rotating counterclockwise.

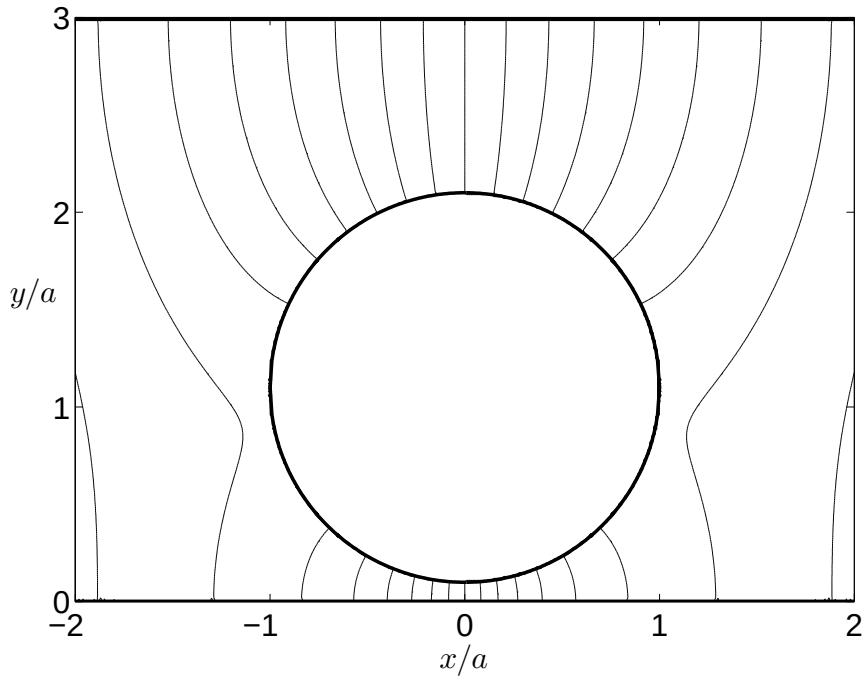

Figure 4.6: Equipotential contours for when the particle is positioned such that $H/a = 3$, $d/a = 1.1$.

on the particle surface as dictated by Eq. (2.3). Figure 4.3(*b*) shows that $\hat{\omega}$ is zero for a symmetrical configuration, but it grows quickly as soon as the particle is located off the centerline. For smaller H/a, $\hat{\omega}$ can be much larger than 1. Therefore, the particle's rotation is sensitive to its eccentricity in a narrow channel. This increased rotational sensitivity is also observed in Unni *et al.* [88] for the wall-bounded spherical particle, where, however, $\hat{\omega}$ of the sphere is below unity at least when $H/(2a)$ is above 0.99.

The flow field is visualized in Figure 4.5(*a*) for $H/a = 3$ and $d/a = 1.1$. The zeta potential on the wall is chosen to be zero so that the electrically neutral walls yield no background velocity and the velocity vectors represent the disturbance velocity from the presence of the particle. The slip velocity on the particle surface is evident in the figure. In addition, Figure 4.5(*b*) visualizes the streamlines around the particle. Here, two stagnation points can be seen on the particle's boundary in the region near the lower wall.

Figure 4.6 visualizes the total electric potential solution with the presence of the

particle. The potential undergoes a quick change along the narrower gap between the particle and channel, causing a high slip velocity of the fluid on both the particle surface and wall in the region.

4.6 Conclusion

In this study, we have implemented a boundary-element method to solve for the electrophoretic mobility of a cylindrical particle placed in a rectangular channel with arbitrary eccentricity. When the ratio between the channel width and cylinder diameter approaches unity, the viscous effect becomes comparable to the electrophoresis and the translational velocity of the particle reaches a finite value determined by the eccentricity. In addition, the rotational velocity of a closely fitting particle is sensitive to its eccentricity.

CHAPTER V

EFFECT OF DC DIELECTROPHORESIS ON THE TRAJECTORY OF A NON-CONDUCTING COLLOIDAL SPHERE IN A BENT PORE

5.1 Background

The purpose of this work was to study the fundamental effect of DC-DEP on particle motion in microchannels where the electric field is non-uniform due to both local channel geometry and presence of the particle. A non-conducting spherical particle driven by electrophoresis in a bent cylindrical pore is chosen as the basic configuration for this study. The BEM solver is used to solve the electrokinetic flow and integrate the Maxwell stress tensor. Governing parameters including the size and initial position of the particle, and the electric field strength, are systematically varied to investigate the DEP effect. In a closely related study, Ai *et al.* [58] investigated the DEP effect on the transient dynamics of an electrophoretic particle in an L-shaped rectangular channel. Using two-dimensional simulations, they also studied the effects of the particle size, initial location, and electric field strength. Compared to their work, the present study solves a three-dimensional flow rather than using a 2D approximation. A 3D study is motivated by several important differences in both the surrounding Stokes flow and the electric field when comparing an infinite cylinder and a sphere. For example, when there is a bounding wall nearby, the fluid within the gap between the particle and wall experiences much less viscous impedance for a sphere than for a cylinder due to the 3D effect. However, the electric field in the gap is much stronger for the cylinder. The opposing effects thus complicate the problem at hand.

In fact, Keh *et al.* [87] showed that the electrophoretic mobility of a non-conducting near-wall cylindrical particle is much higher than that of a sphere, especially when the

particle–wall gap is small. In their work, the translational velocity of the cylinder is 37% higher than that of the sphere when $a/d = 0.9$ (a is radius of the particle and d is the distance from the particle's center to the wall), and the difference between the rotational velocity is even higher (about a factor of 4 when $a/d = 0.9$). Our own calculation using the BEM method shows that the DEP force on a cylinder increases much faster than the DEP on a sphere as they are closer to a plane wall (at $a/d = 0.5$, the normalized DEP force is 0.07 for 3D but is 0.46 for 2D, and at $a/d = 0.98$, the force is 2.12 for 3D but is 23.49 for 2D). In the current study, the small particle–wall gap, whose minimum is on order of 1% of the particle radius, is well resolved using the highly accurate boundary-element method, while in Ai *et al.* [58], the minimum gap appears to be more than 30% of the particle radius. This capability allows us to explore the smaller-gap situation where the DEP effect is much stronger. Finally, another important goal of the present work is to perform a comparison of the full numerical simulation with predictions based on the point-dipole method (PDM) in an effort to provide a clear view of the limitations associated with the latter method.

5.2 Problem specification

The underlying assumptions and theory in each of the studies performed in this dissertation are similar. Because of this, the problem specifications will be similar, but with subtle differences depending on whether DEP is accounted for or the shape of the modeled bounding geometry. Thus, for clarity, each problem specification will be presented in its entirety. This investigation considers a spherical particle suspended in an aqueous electrolyte solution within a cylindrical channel, as shown in Figure 5.1. The problem configuration is three-dimensional where the particle is free to rotate and translate in the plane of symmetry. Both the particle and the channel wall are non-conducting. Surface charge on each is characterized by their respective zeta potentials, ζ_p and ζ_w. As in the 2D study, the electric potential is governed by the Laplace equation,

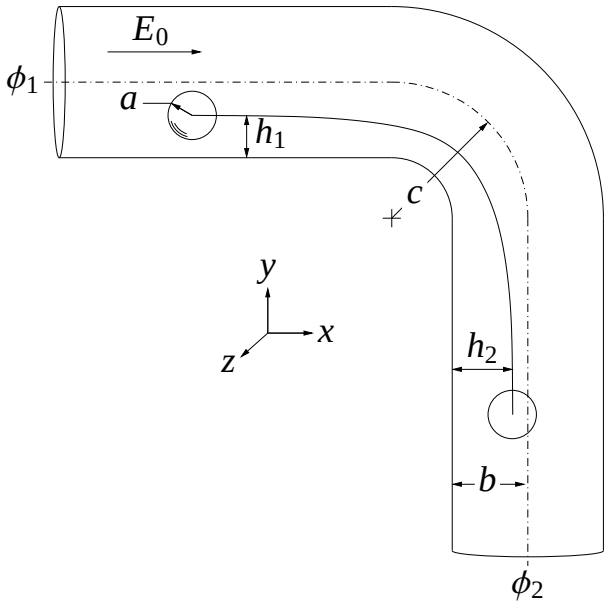

Figure 5.1: Schematic of a non-conducting particle moving through a cylindrical pore due to electrophoresis, where the trajectory is deflected due to the DEP effect.

Eq. (2.4) and is subject to the homogeneous Neumann boundary condition, $\partial\phi/\partial\mathbf{n} = 0$, at all particle surfaces and channel walls [62]. A constant potential is specified at the inlet, $\phi = \phi_1$, and also at the outlet, $\phi = \phi_2$. Note that $\mathbf{n}$ is the surface normal and points into the flow.

The Stokes and continuity equations, Eq. (3.16), are used to model the Bulk flow. Using the thin-EDL assumption, we express the fluid velocity next to the particle and channel walls using a slip velocity that is proportional to the local tangential gradient of the electric potential [84],

$$\mathbf{u}^S = \frac{\varepsilon\zeta}{\mu}(\mathbf{I} - \mathbf{nn}) \cdot \nabla\phi, \tag{5.1}$$

where $\mathbf{u}^S$ is the slip velocity, ε is the dielectric constant of the electrolyte solution, $\zeta = \zeta_p$ or ζ_w is the zeta potential on either the particle surface or channel wall. Details of the surface gradient operator $(\mathbf{I} - \mathbf{nn})$ are provided in Eq. (4.2). In laboratory coordinates, the fluid velocity at the particle surface is a combination of the rigid-body motion of the

particle and the slip velocity,

$$\mathbf{u}(\mathbf{x}) = \mathbf{u}^B + \mathbf{u}^S = \mathbf{u}_c + \omega \mathbf{e}_z \times (\mathbf{x} - \mathbf{x}_c) + \mathbf{u}^S, \tag{5.2}$$

in which $\mathbf{x}$ is a point on the particle surface, $\mathbf{x}_c$ and $\mathbf{u}_c$ are the position and velocity of the centroid of the particle, ω is the rotational speed of the particle, $\mathbf{e}_z$ is the unit vector in z, and $\mathbf{u}^B = \mathbf{u}_c + \omega \mathbf{e}_z \times (\mathbf{x} - \mathbf{x}_c)$ is the velocity of the point $\mathbf{x}$ due to the rigid body motion. The particle is assumed to be neutrally buoyant in the fluid and has negligible inertia. Thus, the total traction and torque on the particle vanish,

$$\int_P \mathbf{f}_t \, \mathrm{d}S = \mathbf{0}, \qquad \int_P (\mathbf{x} - \mathbf{x}_c) \times \mathbf{f}_t \, \mathrm{d}S = \mathbf{0}, \tag{5.3}$$

where P represents the particle surface. This study accounts for DEP. As such, the total traction in Eq.(5.3) is defined as

$$\mathbf{f}_t = (\mathbf{T} + \boldsymbol{\sigma}) \cdot \mathbf{n}, \tag{5.4}$$

where $\boldsymbol{\sigma}$ is the hydrodynamic stress tensor and $\mathbf{T}$ is the Maxwell stress tensor [75] given by Eq. (2.14). Note that because we are modeling a spherical particle, the Maxwell stress has zero contribution to the torque on the particle.

5.3 Formulation

As in the previous study, the Laplace equation solution is independent of the solution of Stokes flow while the latter depends on the former through the slip velocity boundary condition. Therefore, the Laplace equation and Stokes flow can be solved sequentially. No decomposition is used in this study, thus, we begin with Eq. (3.10) repeated here for

convenience,

$$\frac{1}{2}\phi(\mathbf{x}_0) = -\int_D g(\mathbf{x}_0, \mathbf{x})[\mathbf{n} \cdot \nabla\phi(\mathbf{x})]dS(\mathbf{x}) + \int_D \phi(\mathbf{x})[\mathbf{n} \cdot \nabla g(\mathbf{x}_0, \mathbf{x})]dS(\mathbf{x}). \quad (5.5)$$

To address the singularity as $\mathbf{x}$ approaches $\mathbf{x}_0$ within the second integral on the right-hand side, we take advantage of the integral identity in Eq. (3.23),

$$\int_D [\mathbf{n}(\mathbf{x}) \cdot \nabla g(\mathbf{x}, \mathbf{x}_0)]dS(\mathbf{x}) = \frac{1}{2} \quad (5.6)$$

by noting that $\mathbf{x}_0$ falls on the boundary D. If we express the second integral in Eq. (5.5) as

$$\int_D \phi(\mathbf{x})[\mathbf{n} \cdot \nabla g(\mathbf{x}_0, \mathbf{x})]dS(\mathbf{x}) = \int_D [\phi(\mathbf{x}) - \phi(\mathbf{x}_0)][\mathbf{n} \cdot \nabla g(\mathbf{x}_0, \mathbf{x})]dS(\mathbf{x}) + \int_D \phi(\mathbf{x}_0)[\mathbf{n} \cdot \nabla g(\mathbf{x}_0, \mathbf{x})]dS(\mathbf{x}), \quad (5.7)$$

then we can use Eq. (5.6) to simplify it to the following form,

$$\int_D \phi(\mathbf{x})[\mathbf{n} \cdot \nabla g(\mathbf{x}_0, \mathbf{x})]dS(\mathbf{x}) = \int_D [\phi(\mathbf{x}) - \phi(\mathbf{x}_0)][\mathbf{n} \cdot \nabla g(\mathbf{x}_0, \mathbf{x})]dS(\mathbf{x}) + \frac{1}{2}\phi(\mathbf{x}_0). \quad (5.8)$$

Implementing this adjustment into Eq. (5.5) allows us to remove the singularity and transform the integral equation for the laplace equation into

$$0 = -\int_D g(\mathbf{x}_0, \mathbf{x})[\mathbf{n} \cdot \nabla\phi(\mathbf{x})]dS(\mathbf{x}) + \int_D [\phi(\mathbf{x}) - \phi(\mathbf{x}_0)][\mathbf{n} \cdot \nabla g(\mathbf{x}_0, \mathbf{x})]dS(\mathbf{x}). \quad (5.9)$$

To solve the flow, we begin with Eq. (3.22), the 3D integral equation for Stokes flow, repeated here

$$\frac{1}{2}u_j(\mathbf{x}_0) = -\frac{1}{8\pi\mu}\int_D G_{ji}(\mathbf{x}_0, \mathbf{x}) f_i(\mathbf{x})dS(\mathbf{x}) + \frac{1}{8\pi}\int_D u_i(\mathbf{x})T_{ijk}(\mathbf{x}, \mathbf{x}_0)n_k(\mathbf{x})dS(\mathbf{x}). \quad (5.10)$$

Because the fluid velocity at the particle surface includes both rigid-body motion and the slip velocity, Eq. (5.10) needs further manipulation before it can be solved. To do this, we use Eq. (5.2) and apply the integral identities for the right-hand term containing the rigid body motion, Eq. (3.26). The final equation depends on whether the evaluation point $\mathbf{x}_0$ is located on the particle or on the pore surface. If $\mathbf{x}_0$ is on the particle surface, Eq. (5.10) becomes

$$u_j^B(\mathbf{x}_0) + \frac{1}{2}u_j^S(\mathbf{x}_0) = \\ -\frac{1}{8\pi\mu}\int_D G_{ji}(\mathbf{x}_0,\mathbf{x})\, f_i(\mathbf{x}) dS(\mathbf{x}) + \frac{1}{8\pi}\int_D u_i^S(\mathbf{x}) T_{ijk}(\mathbf{x},\mathbf{x}_0) n_k(\mathbf{x}) dS(\mathbf{x}), \qquad (5.11)$$

and if $\mathbf{x}_0$ is on the pore surface, it becomes

$$\frac{1}{2}u_j^S(\mathbf{x}_0) = -\frac{1}{8\pi\mu}\int_D G_{ji}(\mathbf{x}_0,\mathbf{x})\, f_i(\mathbf{x}) dS(\mathbf{x}) + \frac{1}{8\pi}\int_D u_i^S(\mathbf{x}) T_{ijk}(\mathbf{x},\mathbf{x}_0) n_k(\mathbf{x}) dS(\mathbf{x}). \quad (5.12)$$

the only difference between (5.11) and (5.12) is that there would be no rigid-body term on the left side of (5.12).

Similar techniques are used to avoid the singularities inherent in the integral equations for the fluid velocity. Specifically, the use of local polar coordinates remove the singularity exhibited by the first integral on the right side of Eqs. (5.11) and (5.12). For the second integral, the identity discussed in Eqs. (3.24) is applied. When $\mathbf{x}_0$ is positioned on the surface of the boundary, this identity takes on the following form,

$$\int_D T_{ijk}(\mathbf{x},\mathbf{x}_0) n_k(\mathbf{x}) dS(\mathbf{x}) = 4\pi\delta_{ij}. \qquad (5.13)$$

Similar to the technique used for the electric potential, Eq. (5.13) allows us to remove

the singularity and transform the velocity integral equation into

$$u_j^B(\mathbf{x}_0) = -\frac{1}{8\pi\mu}\int_D G_{ji}(\mathbf{x}_0,\mathbf{x})\, f_i(\mathbf{x}) dS(\mathbf{x}) + \frac{1}{8\pi}\int_D [u_i^S(\mathbf{x}) - u_i^S(\mathbf{x}_0)] T_{ijk}(\mathbf{x},\mathbf{x}_0) n_k(\mathbf{x}) dS(\mathbf{x}), \tag{5.14}$$

when $\mathbf{x}_0$ lies on the particle surface and,

$$0 = -\frac{1}{8\pi\mu}\int_D G_{ji}(\mathbf{x}_0,\mathbf{x})\, f_i(\mathbf{x}) dS(\mathbf{x}) + \frac{1}{8\pi}\int_D [u_i^S(\mathbf{x}) - u_i^S(\mathbf{x}_0)] T_{ijk}(\mathbf{x},\mathbf{x}_0) n_k(\mathbf{x}) dS(\mathbf{x}), \tag{5.15}$$

when $\mathbf{x}_0$ lies on the pore surface. By property of Kronecker's delta, $u_i\delta_{ij} = u_j$. After discretization, these relations will be used to formulate the algebraic system to obtain the hydrodynamic traction, f_i, on the particle and cylinder surfaces (note that the fluid velocity at these surfaces will be based on the slip velocity and can be obtained, once ϕ and its gradient are available). Once the traction is obtained, the fluid velocity at any interior point in the flow can be calculated in post-processing.

To discretize the integral equations, the particle surface, cylinder wall, and the inlet and outlet are represented using six-node curved triangular elements. The unknown variables pertinent to the electric field, i.e., ϕ at the particle and wall surfaces and $\partial\phi/\partial\mathbf{n}$ at the inlet/outlet, are discretized at the six vertices of the elements. The unknown variables pertinent to the flow, i.e., the traction f_i, are discretized at the element centroids. At each time step, the integral equation for the electric potential is solved first. Then, the slip velocity at all surfaces is found from Eq. (5.1) by computing the gradient of ϕ numerically. In the end, Eqns. (5.14) and (5.15) are solved together with unknown translational and rotational velocities of the particle. To match the total number of unknowns, two additional equations in Eq. (5.3), expressing the total traction and the total torque on the particle are appended to the linear algebraic system. Note that in Eq. (5.3) the contribution of the Maxwell stress can be computed explicitly once the electric field

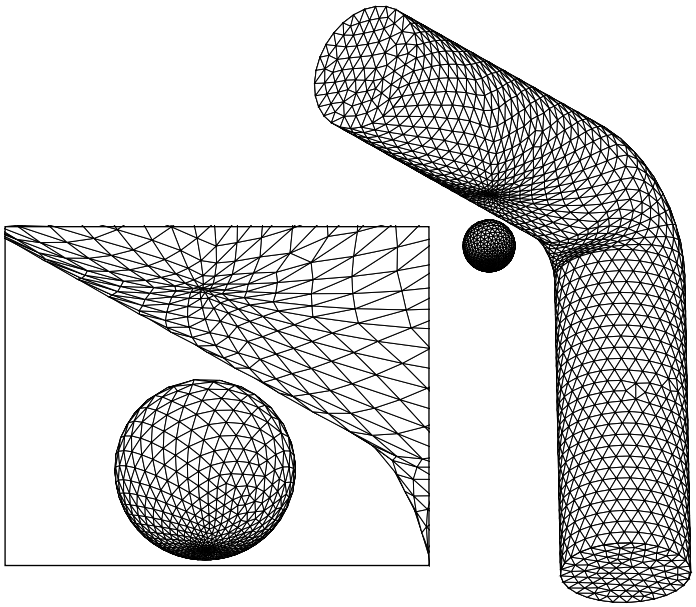

Figure 5.2: The adaptive mesh used in the BEM simulation. Note that the particle is translated outside of the channel to better visualize its mesh.

is obtained.

The element size of the mesh used in this study is adaptive and is based on the particle's proximity to the wall. That is, the local resolution of the mesh around the particle–wall gap, including both the particle and wall surfaces, is increased to make sure that the small region is resolved sufficiently (see Figure 5.2).

5.4 Validation

In order to validate the accuracy of the present BEM code, we compared our results with those published previously. Three problems for which an analytical solution is available were chosen for the test.

In first two tests, we consider the configuration of a non-conducting spherical particle suspended in an electrolyte and positioned near an infinite non-conducting plane wall. Solutions for these tests are compared in Table 5.1. In the first test, we calcu-

late the "wall-enhanced" electrophoretic velocity reported by Keh and Chen [59] for the particle when translating steadily along the plane wall (deactivating the Maxwell stress in the code). In the second test, the lateral dielectrophoretic force of the particle is calculated and compared with that reported by Young and Li [60]. Both of these effects have to do with the distortion of the electric potential in the a narrow gap between the particle and wall. For these tests, the code was slightly modified to calculate the disturbance potential and flow field caused by introducing the particle. This technique is described in more detail in a previous report [71].

Table 5.1: Comparison of our results with the analytical solutions for an electrophoretic particle near a plane wall. (a) translational electrophoretic mobility of the particle, U_p; (b) the dielectrophoretic force F_{dep}. a is the particle radius, and d is the distance of the particle center from the wall.

(a)

	$U_p\mu/[\varepsilon(\zeta_p-\zeta_w)E_0]$	
a/d	Current study	Keh and Chen [59]
0.50	0.994	0.994
0.70	0.988	0.989
0.90	0.997	0.998
0.95	1.022	1.022
0.98	1.080	1.080
0.99	1.147	1.145

(b)

	$F_{dep}/[\varepsilon E_0^2 a^2/2]$	
a/d	Current study	Young and Li [60]
0.50	0.074	0.075
0.71	0.336	0.337
0.91	1.133	1.136
0.95	1.584	1.587
0.98	2.121	2.124
0.99	2.457	2.459

For the first test, the normalized translational mobility is tabulated in Table 5.1(a) as a function of a/d, where a is the particle radius and d is the distance from the particle center to the wall. From this comparison, we can see the mobility decrease to a minimum before increasing to values greater than that of an unbounded particle. This is consistent with the result previously reported. In that report, Keh and Chen [59] represented the exact solution with eigenfunction expansion series in bipolar coordinates. It should be noted that the closest particle–wall separation simulated in the current study was $a/d = 0.98$ (where d is defined using the nearest wall. This corresponds to a difference between our numerical result and the analytical solution [59] of less than 0.03%, exemplifying the exceptional accuracy of the boundary element approach.

The second comparison, tabulated in Table 5.1(b), is the normalized DEP force acting in the lateral direction as a function of a/d. Here, we can see that the lateral force monotonically increases with a decreasing gap width. This trend agrees with the exact solution originally obtained by Young and Li [60]. Similar to the electrophoretic validation, superb accuracy was achieved. For the closest particle–wall separation simulated in the current study ($a/d = 0.98$), the difference between our result and the analytical result is less than 0.2%.

The domain used in the present study consists of a spherical particle within a cylindrical pore, so it is also appropriate to conduct a validation for such an enclosed geometry. Thus, our third test concerns a spherical, electrophoretic particle within a straight cylinder. Our numerical result was compared with the analytical result reported by Keh and Chiou [89], who found the fundamental solution of the problem and then applied the Fourier transform and a collocation technique to impose the boundary conditions on the particle and wall. The cylinder in our test was truncated so that its length is 6 times its own diameter. The comparison is shown in Table 5.2, where it can be seen that the non-dimensional electrophoretic mobility of the particle monotonically decreases as the radius of the particle increases. This pore-impedance effect parallels that discussed by Keh and Chiou [89] and is caused by the hydrodynamic retardation due to the presence of the wall. Again, the numerical results are in excellent agreement with the analytical solution.

5.5 Simulation setup

For the current study, the cylindrical pore of radius b is chosen such that the turning radius, c, as measured from the cylinder's centerline is $c/b = 1.2$. The total length of the cylinder along the centerline is $L/b = 12$, and the bend takes place in the middle of the cylinder. The nominal electric field strength, $E_0 = (\phi_1 - \phi_2)/L$, is used as a variable of study. The non-dimensional form adopted for this variable is $E_0^* = E_0(b/\zeta_p)$.

Table 5.2: Comparison of our results with the analytical solution for the normalized translational mobility, U_p, of a sphere concentrically positioned within a cylindrical pore, where a and b are the particle and cylinder radii.

	$U_p\mu/[\varepsilon(\zeta_p - \zeta_w)E_0]$	
a/b	Current study	Keh and Chiou [89]
0.1	1.000	0.999
0.2	0.990	0.990
0.3	0.966	0.969
0.4	0.928	0.932
0.5	0.872	0.880

In simulations, 1294 elements were used to model the particle and 4026 elements for the cylinder wall. Sufficiency of the described mesh in resolving small particle–wall gap distances has been demonstrated in the validation tests. After extensive testing, a time step of $\Delta t = 0.05a/U_p$, where $U_p = \varepsilon(\zeta_p - \zeta_w)E_0/\mu$, was utilized for transient simulations to ensure Δt was small enough to accurately predict the particle's trajectory.

To illustrate the results obtained from our BEM code, Figure 5.3 plots the electric potential and flow field computed after the boundary-element solution was obtained for an arbitrarily specified particle location. For comparison, Figures 5.3(a) and (b) visualize equipotential curves and the electric field strength for cases with and without a suspended particle. In this comparison, the normalized particle radius is $a/b = 0.4$, and it is positioned within the bend near the inner side of the pore. From Figure 5.3(b) we can see that a nonuniform electric field is created due to the pore bend itself. Here the analogy of a bending beam under a transverse load can be used to visualize the effect this geometry has on the electric field. When a beam deforms under a transverse load, the volume on the inner side of the bend is under compression while the opposite side is under tension. The electric field shown in Figure 5.3(b) behaves similarly. Observing the equipotential lines in this figure, we can see how the contours appear "compressed" near the inner side of the bend and the compression corresponds to a greater electric field strength $\boldsymbol{E} = -\nabla\phi$. Such spatial nonuniform electric field would facilitate genera-

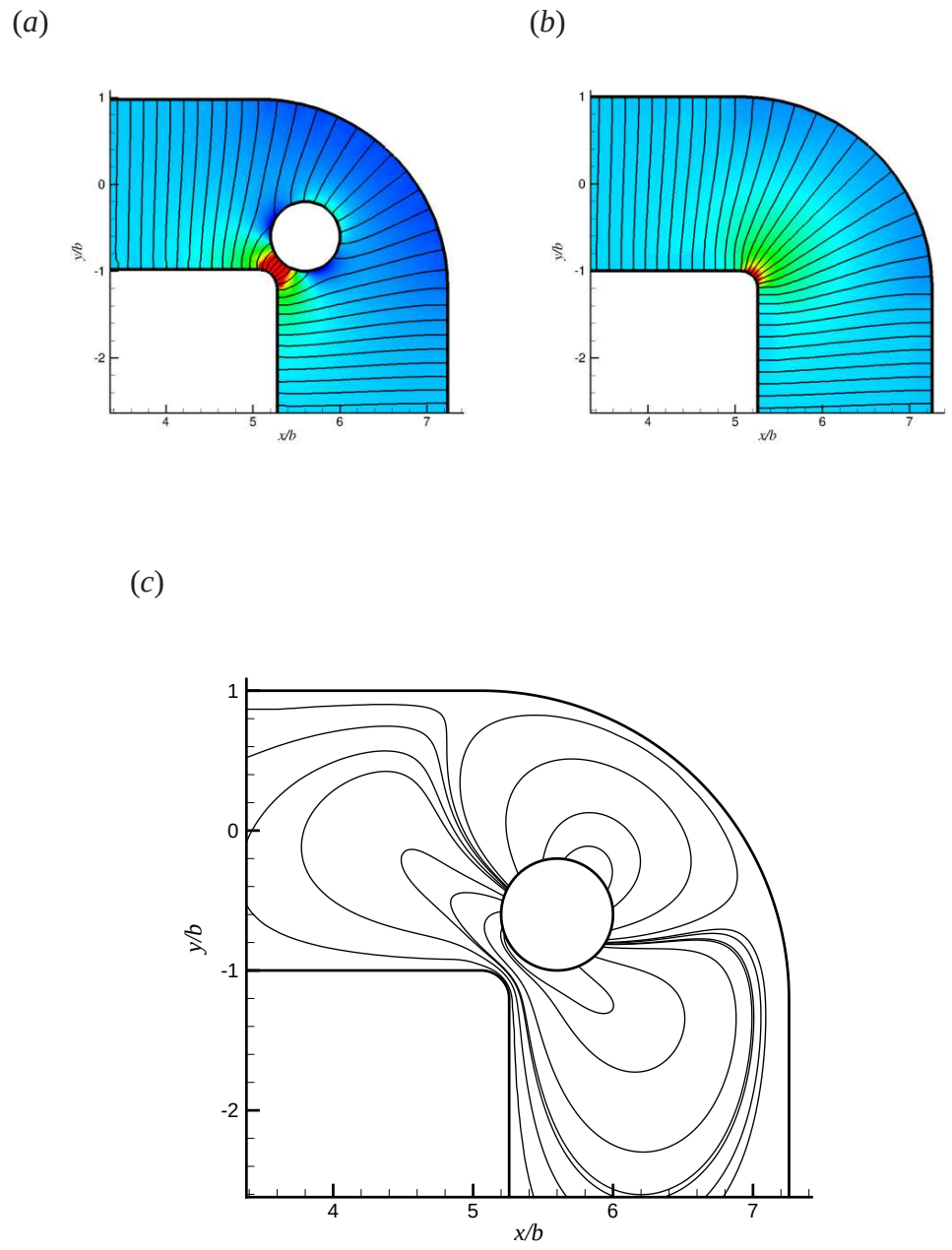

Figure 5.3: Internal field solutions for a particle ($a/b = 0.4$) positioned close to the inner wall. Equipotential contours are plotted over electric field strength with (a) and without (b) the particle. The corresponding flow field of (a) is shown in (c).

tion of the DEP force. In addition, the close proximity of the particle to the wall further distorts the electric field by raising the electric potential in the gap region, as shown in Figure 5.3(a). From this, we can expect that the DEP force will be strengthened when the particle goes through the bend. Figure 5.3(c) plots the corresponding streamlines in the presence of the particle under the same conditions as Figure 5.3(a) with the electroosmotic flow set to zero. Here, we can see the distortion in the flow field induced by the presence of the particle. Note that the plots are independent of the choice for E_0 or the zeta potential.

To justify the need for the full numerical simulation, we also compare our particle trajectory with that predicted by the point-dipole method. When using the PDM, the DEP force is calculated as if the particle were not present and both the electric field and the flow field were undisturbed. The motion of the particle, which is approximated by an infinitesimal point, is then a combination of the Smoluchowski velocity (electrophoretic translation of an unbounded particle), the electroosmotic velocity, and the velocity due to the DEP force,

$$\mathbf{u} = \mathbf{u}_{ep} - \mathbf{u}_{eof} + \mathbf{u}_{dep} = \frac{\varepsilon\zeta_p}{\mu}\mathbf{E} - \frac{\varepsilon\zeta_w}{\mu}\mathbf{E} + \frac{\varepsilon a^2 f_{cm}}{3\mu}\nabla|\mathbf{E}|^2. \tag{5.16}$$

where f_{cm}, the Clausius–Mossotti function, is $-\frac{1}{2}$ for a non-conducting spherical particle [10]. The DEP translational velocity is found by assuming the DEP force equal to the Stokes drag force induced by $\mathbf{u}_{dep}$, that is,

$$\mathbf{F}_{dep} = \mathbf{F}_{Drag} = 6\pi\mu a\mathbf{u}_{dep}. \tag{5.17}$$

To evaluate Eq. (5.16), the field strength E of the undisturbed electric field at the location of the centroid of the particle is used for each term.

Note that in the current BEM simulation, neither the point-dipole approximation of the DEP force, or the Stokes drag is assumed for the finite-size particle. To show the

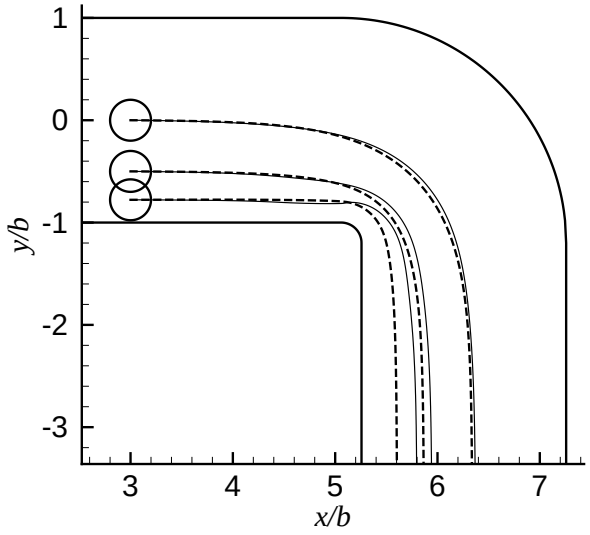

Figure 5.4: The effect of initial position, h_1/b, on the particle trajectory for $a/b = 0.2$ and $E_0^* = 5$. Dashed lines represent results found using the BEM and the solid lines represent trajectories predicted by the point-dipole method.

difference between our numerical result and the PDM, we use both methods for the instantaneous particle location used in Figure 5.3 under a non-dimensional, nominal electric field, $E_0^* = 20$. The BEM method shows that $u_{ep}/U_p = 1.12$ and $u_{dep}/U_p = 0.48$, while the point-dipole approximation claims $u_{ep}/U_p = 1.25$ and $u_{dep}/U_p = 1.51$. Therefore, the PDM may lead to significant error in estimation of the DEP mobility of the particle.

5.6 Results

5.6.1 Effect of the initial location

The first parameter studied was the eccentricity of the particle. In this section we wanted to observe the effect that the particle's initial location had on its trajectory. We are also interested in the ability of the PDM to predict this effect. For these simulations, the particle's radius was held constant at $a/b = 0.2$ while the initial location of the particle was adjusted to three different values: $h_1/b = 1.0$, 0.5 and 0.22. Note that in

the third case, the initial particle–wall gap is 10% of the particle radius. The results of these tests are presented as dashed lines in Figure 5.4 for the case of $E_0^* = 5$.

While approaching the exit of the pore, the final deviation of each particle from its original location was found to be $(h_2 - h_1)/h_1 = 0.08$, 0.22 and 0.56, respectively for the three cases. Apparent from this is what was anticipated. A particle positioned closer to the inner side of the bent region will deviate farther from the wall than that of a particle originally positioned closer to the center of the pore. As was visualized in Figure 5.3, the highest electric field strength is found in the region within the cylinder close to the inside of the bend. It follows that the dielectrophoretic force acting on a particle closer to that region would be greater because this force scales with $|\mathbf{E}|^2$. The particle originally positioned with the highest eccentricity is shifted by a distance equal to 62% of its own radius. Considering the scenario of a stream of multiple particles, each with a different initial location, this effect would serve to reduce the width of the particle stream in a focusing effect by “pushing" the near-wall particles away from the wall.

The analogous trajectories found using the PDM are displayed as solid lines in Figure 5.4. It is clear from this figure that the PDM fails to accurately predict the path of a particle positioned close to the cylinder wall. When observing each trajectory with respect to the particle’s original positions, we can see that the accuracy of this method degrades with a decreasing particle–wall gap. The final deviations as shown in the figure are $(h_2 - h_1)/h_1 = 0.11$, 0.37 and 1.44 for $h_1/b = 1.0$, 0.5 and 0.22, respectively. Although the PDM overshoots the particle’s deviation in each of the cases tested, it does provide a reasonable approximation for the case of a particle positioned at the center of the pore.

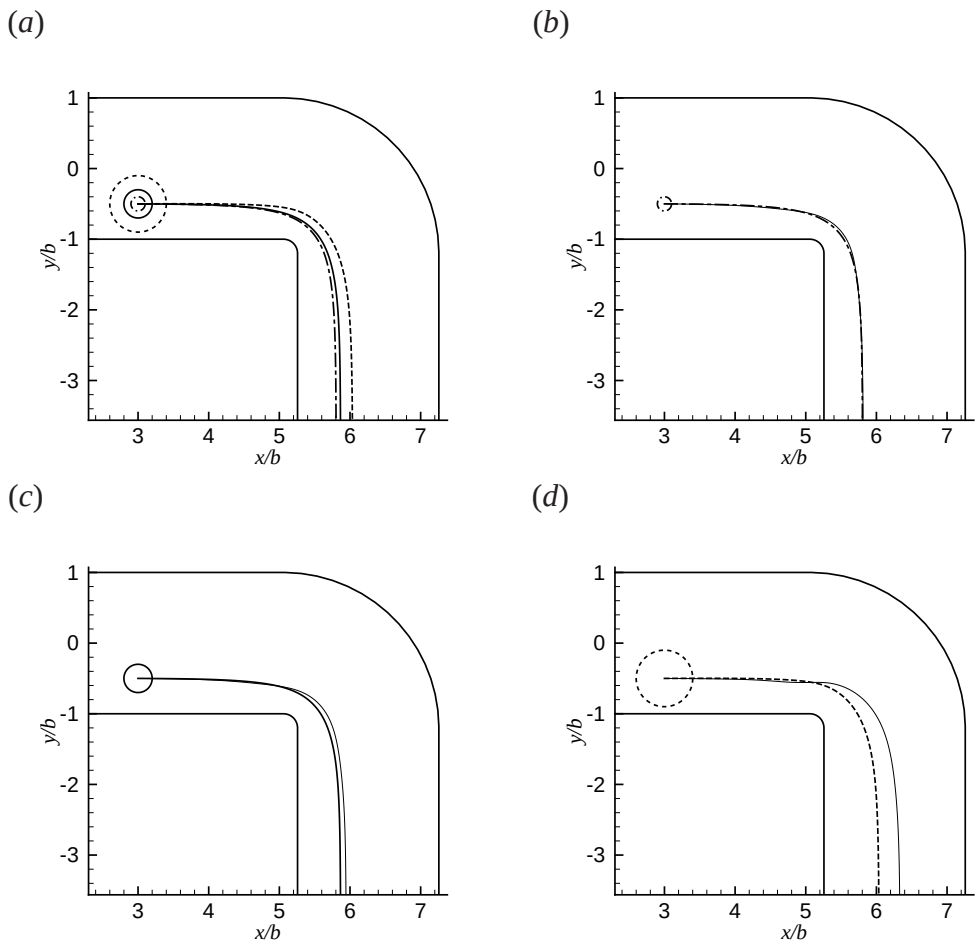

Figure 5.5: The effect of the particle size, a/b, on the particle trajectory for the case of $h_1/b = 0.5$ and $E_0^* = 5$. Dash-dotted, solid (thick) and dashed line patterns represent $a/b = 0.1$, 0.2 and 0.4 respectively in (a). In (b-d) the thin-solid line represents the estimate from the point-dipole method.

5.6.2 Effect of particle size

In scaling, the dielectrophoretic force is also proportional to the volume of the insulating particle. Therefore it is also of interest to study how the particle's radius effects its trajectory. In the present study, this effect is complicated by the manner in which the particle's finite, insulating volume modifies the flow and electric field. Three particle-to-cylinder radius ratios were tested in this section: $a/b = 0.1$, 0.2 and 0.4. The same original position was used for each of the particles, $h_1/b = 0.5$, and the nominal electric field was held constant at $E_0^* = 5$. The resulting trajectory for each case can be seen in Figure 5.5(a). As one would expect, the the larger particle shifts toward the centerline of the pore to a greater extent when compared to the smaller particles. The final deviations from the wall are $(h_2 - h_1)/h_1 = 0.09$, 0.22 and 0.56 for the three cases respectively.

We also calculated the trajectory of the particle based on the PDM to evaluate its validity. Figures 5.5(b), (c) and (d) plot a comparison between the trajectories found using our numerical technique and the PDM for each particle size. The thin-solid line shows the PDM result, whereas the line pattern for the BEM result follows that of Figure 5.5(a). From Figures 5.5(b) and (c) it is apparent that at sufficiently small particle sizes, the PDM can provide a reasonable approximation of its trajectory in this configuration. For $a/b = 0.1$, the difference in the trajectories predicted by the two methods is less than 1% of the pore radius. For $a/b = 0.2$, this difference is roughly 8%. Observing Figure 5.5(d), however, we can conclude that utilizing the PDM leads to significant error for the case of a large particle size. The final difference between the two techniques for the case of $a/b = 0.4$ is approximately 30% of the pore radius.

To more clearly visualize the difference in the results of the two numerical methods, Figure 5.6 plots the non-dimensional magnitude of the DEP force as a function of the non-dimensional time as the particle migrates through the dashed trajectory shown in Figure 5.5(d). Both the BEM calculation (dashed line) and the point-dipole approximation (solid line) of the DEP force are plotted. It can be seen from Figure 5.6 that

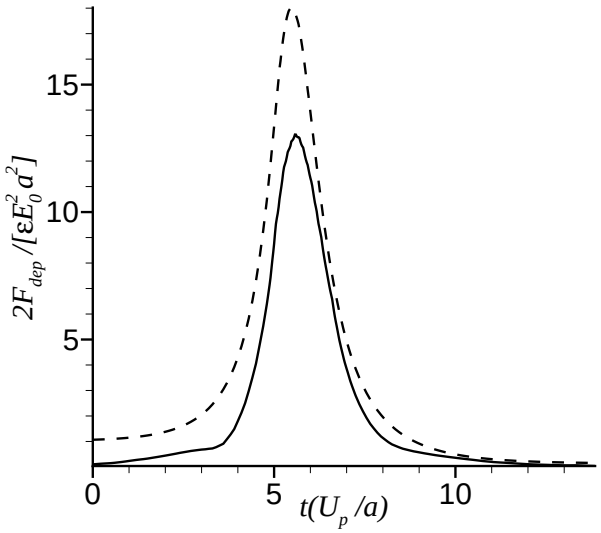

Figure 5.6: The normalized DEP force as the particle moves along the trajectory shown in Figure 5.5(d) from the BEM simulation. The dashed line shows the current result, and the solid line shows the point-dipole approximation.

during the initial stage, the BEM yields a DEP force whereas the PDM does not. At this phase, the particle is positioned close to the inside of the wall just before the bend. The presence of the particle causes a strong electric field in the narrow region, which generates a DEP force acting laterally and pushes the particle away from the wall. This result is similar to the flat-wall case described earlier in Table 5.1(b). When using the PDM, there is no such particle–wall interaction and therefore there is no DEP force.

As the particle nears the inside corner of the bend, the magnitude of the DEP force quickly increases to a maximum before decreasing as it leaves the turn. This occurs because of the non-uniform electric field originating from the insulating boundary. During this phase, the current technique reports a stronger DEP force compared to the PDM. Again, the enhanced DEP can be explained by the interaction between the finite-size particle and the wall.

It is important to note that although the resultant DEP force is stronger when using the Maxwell stress tensor compared to the PDM, the former does not result in greater lateral motion of the particle compared to that found from the PDM. On the contrary, the

trajectory predicted by the PDM overshoots as shown in Figure 5.6 and thus indicates a higher lateral velocity. This result can be explained by the use of the Stokes drag formula, Eq. (5.17), to equate with the DEP force in the PDM. However, Stokes drag is valid for unbounded or large domains. Because the spherical particle in this study is bounded by the pore of comparable sizes, the hydrodynamic drag acting on the particle will be greater than that predicted by Stokes drag.

In Figure 5.6, after the particle passes through the turn, the DEP forces given by both the BEM and PDM decrease to approximately zero. This is because the particle is positioned near the center and there is little particle–wall interaction. Therefore, the two techniques agree with each other.

5.6.3 Effect of the electric field

Table 5.3: Deviation of trajectory, $(h_2 - h_1)/h_1$, for both the point-dipole method and the BEM used in this study for the cases in Figure 5.7.

	$a/b = 0.2$		$a/b = 0.4$	
E_0^*	Current study	PDM	Current study	PDM
5	1.35	1.38	1.41	1.53
10	1.38	1.44	1.50	1.68
20	1.45	1.53	1.61	—

The electric field is spatially non-uniform in the region close to the bend. A stronger DEP force is associated with a particle positioned closer to the inner side of the bend – we have observed this in a previous section. Other than the particle's size and location, the dielectrophoretic force is also a function of the applied electric potential across both ends of the pore. As was shown by Ai *et al.* [58] for the case of a 2D simulation for a turning channel, we can expect that the particle will deviate farther from the inner wall of the pore with an increasing electric field strength. This is verified in Figure 5.7(a) and (d) for the cases of $a/b = 0.2$ and 0.4 respectively. The applied electric field

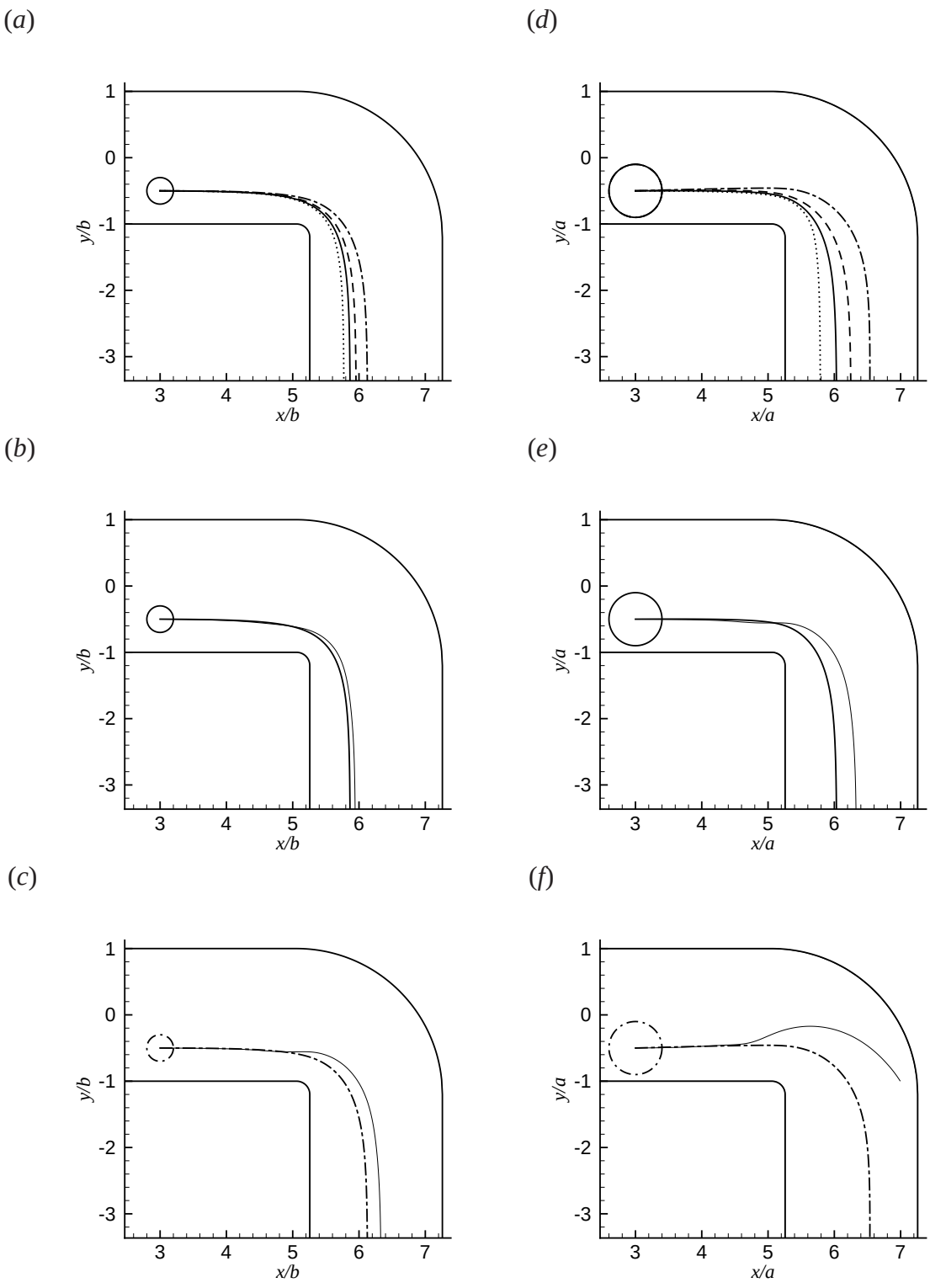

Figure 5.7: Trajectories for $a/b = 0.2$ (a-c) and $a/b = 0.4$ (d-f) under varying electric field strengths but the same initial position ($h_1/b = 0.5$). (a) and (d) depict the cases of $E_0^* = 5$, 10, 20, and the case in which DEP is neglected ($E_0^* = 5$) using solid, dashed, dot-dashed, and dotted respectively. A comparison between the PDM and BEM is shown for the cases of $E_0^* = 5$ (b,e) and 4 (c,f). Thin-solid lines represent the PDM trajectory and the line pattern of the BEM trajectories follow those introduced in (a) and (d).

values shown in both Figure 5.7(a) and (d) correspond to $E_0^* = 5$, 10 and 20 with line patterns of thick-solid, dashed and dash-dotted respectively. The inner-most dotted line represents the trajectory of the particle in the absence of dielectrophoresis for $E_0^* = 5$. For these results the particle's initial location within the pore is $h_1/b = 0.5$. From Figure 5.7(a), we can see the transient effect of electric field strength on the trajectory of an electrophoretic particle. Specifically, the stronger the electric field is, the more the particle would translate laterally across the pore. From Figure 5.7(d) we can see the combined effect of the electric field strength on the largest particle, $a/b = 0.4$. Similar to the result seen in Figure 5.7(a), the particle deviates from the inner wall to a greater extent with an increasing field strength. Additionally, because the DEP force also scales with the particle volume, the corresponding deviation for $a/b = 0.4$ is larger than that for $a/b = 0.2$.

In the numerical technique implemented in this study, the local distortion of the electric field due to the presence of the non-conducting spherical particle is accounted for by integrating Eq. (2.14) around the particle surface. As the PDM neglects this distortion, we would expect that the disagreement between the two techniques would grow with an increasing electric field strength. Figures 5.7(b) and (c) depict a comparison between the two numerical techniques for $E_0^* = 5$ and 20 where $a/b = 0.2$. Continuing in the comparison of the particle size, Figures 5.7(e) and (f) plot the results of equivalent simulations at $a/b = 0.4$. Again, the thin-solid line visualizes the PDM result and the line pattern for the BEM result follows that of Figures 5.7(a) and (d). Under a weaker electric field, the magnitude of the dielectrophoretic force is reduced and therefore the field distortion is not as influential. Therefore, the PDM and BEM give similar result, as shown in as shown in Figure 5.7(b). However, it is evident from Figure 5.7(c) that under the influence of a stronger electric field, the accuracy of the PDM degrades. At a non-dimensional field strength of $E_0^* = 20$, the difference between the two techniques is greater than 20% of the pore radius.

By comparing Figures 5.7(e) and (f), we can observe how quickly the PDM breaks

down for a larger particle-to-cylinder ratio and a higher electric field. Thus, combining the two effects to model a non-trivial microfluidic channel demands full integration of the Maxwell stress tensor, such as the numerical technique employed in this work. Table 5.3 details the numerical results, in terms of the deviation defined as $(h_2 - h_1)/h_1$, for both the PDM and the technique used in this study for the cases in Figure 5.7. The results for $E_0^* = 10$ are also included in the table. Note the deviation for $E_0^* = 20$ and $a/b = 0.4$ is not available for the PDM because it finally breaks down, as seen in Figure 5.7(f) where the particle tends to cross the wall. In a physical situation, as a finite-size particle approaches the outer wall, the DEP effect on the inner-wall side would decrease and on the other hand, the opposing DEP due to the outer wall would increase. As a result, the overall DEP force in the lateral direction becomes zero, and the particle would not come into contact with the outer wall. As shown in Figure 5.7(f), this effect is captured by the current BEM simulation but not by the PDM.

5.7 Conclusion

In this study, we investigate the fundamental effect of dielectrophoresis on the transient motion of particles in microfluidic channels and address limitations of the point-dipole method. To do so, we have considered a non-conducting spherical particle in a 90° bent cylindrical pore, where the size of particle is comparable to the pore diameter. Results show that near the corner of the wall, the DEP force has a strong effect on the particle's motion. More importantly, for near-wall situations the particle's finite size has a significant effect on its transient trajectory, and using the PDM would lead to substantial error.

As an additional discussion, we would like point out the relevance of our model to real microchannels. For a commonly used aqueous, symmetric electrolyte solution (e.g. KCl) with an ionic concentration of 10^{-3} M and its chemical and electrical properties [3, 90] at room temperature, the EDL thickness (k^{-1}) would be on the order of 10 nm. If we

consider a 20 μm diameter particle, this would yield $ka \approx 1000$, well within the limits of the thin-EDL approximation. In the present study, the minimum gap width occurring between the particle and the channel wall is around 2% of the particle radius, that is, approximately 0.2 μm, which still roughly 20 times the thickness of the EDL.

If we extend this dimensional discussion to include other parameters used in the present study for the case of $a/b = 0.2$, then the diameter and length of the pore are $2b = 100$ μm and $L = 600$ μm. Assuming common properties of polystyrene for the particles ($\zeta_p = -22$ mV, $\rho_p = 1050$ kg/m^3), PDMS for the channel walls ($\zeta_w = -80$ mV) and pure water for the suspending medium ($\epsilon = 6.9\times10^{-10}$ C/Vm, $\mu = 0.9\times10^{-3}$ kg/ms, $\rho_w = 1000$ kg/m^3), the nominal electric field strengths to generate the deviations described in this study are between $E_0 = 60$ and 240 V/cm. These values fall within a range of field strengths commonly used for DC-DEP. Under these operating conditions, one can expect to see electrokinetic particle velocities between 0.2 and 1 mm/s. The sedimentation velocity for a particle under these conditions is roughly 0.012 mm/s. Under our conditions, the particle's electrokinetic velocity is significantly larger than its sedimentation velocity. If weaker fields and/or longer channels are employed, the importance of the particle's motion due to gravity can no longer be neglected. Depending on the orientation of the bent pore, the particle's sedimentation can alter its trajectory.

CHAPTER VI

DIELECTROPHORETIC CHAINING OF TWO ELLIPSOIDAL PARTICLES

6.1 Background

With a growing number of researchers studying electrokinetics [1, 2], many valuable applications have surfaced. One area benefiting from these studies is the self-assembly of colloidal particles into organized structures. With the application of externally applied electric fields, dielectrophoretic forces are exploited to reposition suspended particles. If properly designed, this phenomenon can be used to create patterned materials with desired mechanical, chemical, and biological properties [35, 91, 92]. One such example comes from Yang *et al.* [36, 37]. In an effort to generate heart tissue on a microfluidic chip, these researchers used the electric field between interdigitated electrodes to pattern cardiac myocytes. Markx *et al.* [93] used DEP cell assembly to create a multi-layered structure mimicking that of a hematon, an artificial micro-environment for blood-producing stem cells. This serves to advance the study of stem cell activity for the treatment and prevention of blood diseases. Using latex and silica microspheres and co-planar electrodes, Lumsdon *et al.* [40] were able to assemble well-organized two-dimensional hexagonal crystals. Through means of a similar technique, Velev *et al.* [38] were able to assemble biocomposite materials from a combination of live cells and functionalized particles. In a previous publication, the same researcher had discovered a simple manner to create microwires through DEP aggregation [39].

Two particles in an infinite fluid medium are a basic model configuration to study the driving force behind the DEP colloid assembly. Consider two identical non-conducting particles suspended in an aqueous electrolyte solution under the influence of an externally applied electric field. The presence of these particles locally distorts the electric

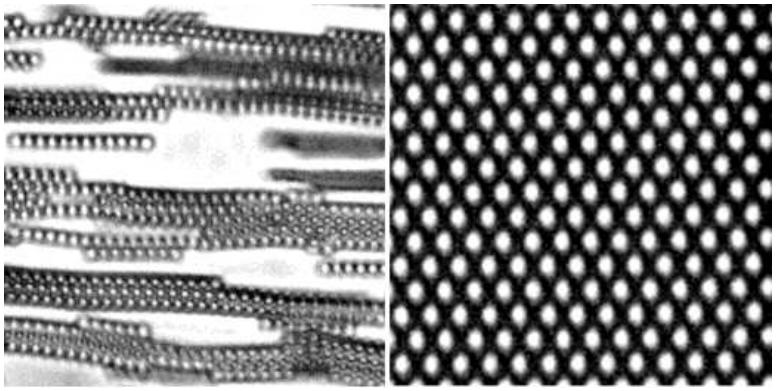

Figure 6.1: Stages of the electric field-induced aggregation of 1.4 μm spherical latex particles reported by Lumsdon *et al.* [40].

field. This results in local minima and maxima around the particle. When the two particles are close enough, the distribution of electric field strength around each particle surface becomes asymmetric. This yields an imbalance of force acting on the induced dipole across the particle. Depending on the alignment of the particles with the electric field, this results in a mutually attractive or repulsive dielectrophoretic motion. This is the underlying theory behind what is referred to as “pearl chaining", the tendency of particles to form chain-like formations when under the influence of an electric field [10, 94].

Past experimental investigations have been focused around the aggregation of spherical particles made of latex or silica [40, 95]. Reported in these studies is an initial particle chaining, followed by a field-induced lateral migration of chains as shown in Figure 6.1. This process results in hexagonally crystalline structures. Recent numerical studies have helped clarify the mechanism behind the relative electrokinetic motion of two insulating spherical particles. Kang and Li [96] investigated this phenomenon by balancing the DEP force with Stokes drag to obtain a particle velocity. In that study, they were able to show how the DEP force of two spherical particles gradually realigns the particles such that the line connecting their centers is parallel with the direction of the electric field. This realignment holds true regardless of their initial orientation with the exception of an “unstable" equilibrium orientation where the particles are initially

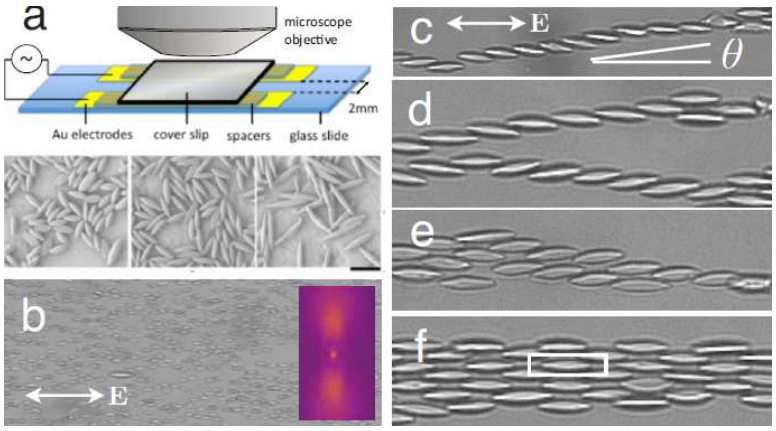

Figure 6.2: Experimental results for electric field-induced aggregation of ellipsoidal polystyrene particles reported by Singh *et al.* [98]. Aspect ratios used were $a/b = 3.0$, 4.3 and 7.6 where $a \approx 10$ μm. The particles transition from a random to an ordered orientation (*b*–*f*) where they form a distinct chaining angle, θ.

arranged orthogonal to the electric field. In a similar study, Ai and Qian [97] used a two-dimensional finite-element package to solve the coupled electric field and flow field around two spherical particles. A similar realignment process was reported. It was also shown that a repulsive hydrodynamic pressure force reduces the velocity of two particles under an attractive DEP force as they ultimately move together.

In the field of microfabrication, complex particle shapes can aid in the design of materials that meet desired properties [99, 100]. Additionally, biological cells that could be incorporated in the synthesis of new tissue typically have an irregular shape [101, 102]. As argued by the other researchers in this field [10, 35], it is important to develop an understanding of the particle–particle interaction occurring for non-spherical particles subjected to electric fields. It has been shown previously that there exists a stable orientation for a single non-spherical particle suspended in an electric field [103, 104]. The electric field induces a net torque acting on the particle which causes it to reorient itself relative to the electric field. This phenomenon is referred to as electro-orientation (not to be confused with electro-rotation which occurs only in fields of spatially varying phase). There has been limited theoretical study on two or more non-spherical particles. Recently, Singh *et al.* [98] investigated the disorder-to-order transition of el-

lipsoidal particles of varying aspect ratios. They reported that the randomly distributed particles at certain field strength form a stable chaining angle in the end, which leads to a distinct crystal structure that is a function of the particle's aspect ratio. Results of this study are visualized in Figure 6.2. Despite the experimental studies performed on the packing of non-spherical particles [99, 100], little has been done to clarify their fundamental interactions when under the influence of an the DEP force.

Previously, Yariv [105] and also Swaminathan and Hu [106] analytically investigated inertial effects on electrophoretic particles. In their work, they detailed a stable orientation that was perpendicular to the field. This contradicts DEP interaction as spherical particles are known to form chains parallel with the field. In a separate report, Kang and Li [96] compare this inertial interaction with DEP interaction and conclude that DEP forces are commonly two orders of magnitude larger than inertial forces. Based on this fact, they neglect inertial interaction. In the current study, we too neglect inertial effects.

In this study we examine the DEP interaction of two non-conducting, ellipsoidal particles in an electric field. Numerical simulations will be performed using the previously developed boundary-element method (BEM) for electrokinetic particles [71, 72]. The BEM, which requires a surface mesh only, is employed due to its superior accuracy and efficiency when considering a linear problem, i.e., an electrokinetic problem with the assumption of thin electric double layer (EDL). This feature is particularly advantageous when the two particles are very close to each other, a situation that would require a high-resolution volume mesh for other approaches such as the finite-element method. It should be pointed out that, unlike some of previous studies, the three-dimensional electric and flow fields are fully resolved when computing the Maxwell and hydrodynamic stresses on the particles, thus eliminating the need to approximate these forces using simplified formulas (e.g., Stokes drag).

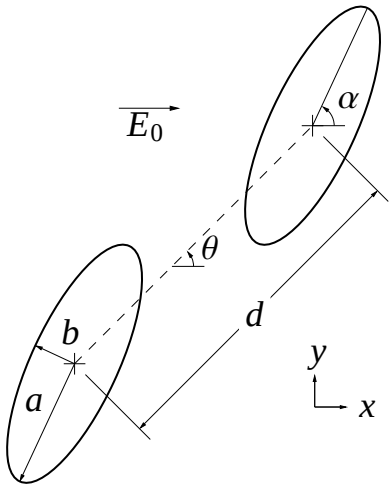

Figure 6.3: Schematic of the two non-conducting ellipsoidal particles suspended in an electrolyte solution under the influence of an electric field.

6.2 Problem specification and governing equations

We consider two identical, non-conducting particles suspended in an aqueous electrolyte solution. The schematic for this study is shown in Figure 6.3, where the particles are prolate spheroids with the following conditions: $a > b$ and $b = c$ where b is the polar radius and a is the equatorial radius. The third semi-minor axis, c, is equal to b and is parallel to the z-axis. The problem configuration is 3D, where the particles are free to rotate and translate in the plane of symmetry.

In an electrolyte, particles are naturally charged and have a non-zero zeta-potential at their surfaces. Therefore, the two particles would move under the combined electrophoretic effect and the DEP forces. However, these two effects can be decoupled if thin-EDLs are assumed near the particle surfaces, due to linearity of the governing equations. Furthermore, the two unbounded particles would have no electrophoretic interaction and would translate at the same velocity as long as they have equal zeta-potentials [107, 108]. This can be explained by modeling both the electric and flow field as potential flow under the thin-EDL assumption [108]. If we decompose the electrophoretic and dielectrophoretic velocities, we can observe the relative velocity at any point on the particle surface. If we assume that the relative velocity is everywhere

proportional to the electric field, it becomes apparent from the Laplace equation that velocity field is also divergence free. Because this satisfies our governing equations and boundary conditions, we can conclude that there is no electrophoretic interaction. This means that for a collection of particles, all with the same charge, each will translate at the Smoluchowski velocity without affecting nearby particles. Therefore, introducing a constant zeta-potential in the present problem would not change the relative motion of the particles but simply add a net electrophoretic translation. For this reason, we may ignore the surface charge and assume a zero zeta-potential for each particle.

The entire flow field is neutral, and the distribution of the electric potential, ϕ, is governed by the Laplace equation, Eq. (2.4). The electric potential is subject to the homogeneous Neumann boundary condition, $\partial\phi/\partial\mathbf{n} = 0$, at each particle surface. Note that $\mathbf{n}$ is the surface normal and points into the flow. The fluid is assumed to be Newtonian and incompressible, and the Reynolds number is small so that the fluid inertia can be ignored. The bulk flow is then governed by the Stokes and continuity equations, Eq. (3.16) The slip velocity typically used with the thin-EDL assumption, as detailed in the previous studies [71, 72], is zero because the zeta potential at each particle surface is set to zero. From this, the fluid velocity at a point $\mathbf{x}$ on the particle surface is equal to the rigid-body motion of the particle due to the no-slip condition,

$$\mathbf{u}(\mathbf{x}) = \mathbf{u}_c + \omega\mathbf{e}_z \times (\mathbf{x} - \mathbf{x}_c) \tag{6.1}$$

in which $\mathbf{x}_c$ and $\mathbf{u}_c$ are the position and velocity of the centroid of the particle, ω is the rotational velocity of the particle, and $\mathbf{e}_z$ is the unit vector in z.

The particle is assumed to be neutrally buoyant in the fluid and has negligible inertia. Thus, the total traction and torque on each particle vanish,

$$\int_P \mathbf{f}_t \, \mathrm{d}S = \mathbf{0}, \qquad \int_P (\mathbf{x} - \mathbf{x}_c) \times \mathbf{f}_t \, \mathrm{d}S = \mathbf{0}, \tag{6.2}$$

where P represents the particle surface and $\mathbf{f}_t$ is the total traction. As in the previous study, the total traction is defined as

$$\mathbf{f}_t = (\mathbf{T} + \boldsymbol{\sigma}) \cdot \mathbf{n}, \tag{6.3}$$

where $\boldsymbol{\sigma}$ is the hydrodynamic stress tensor and $\mathbf{T}$ is the Maxwell stress tensor given by Eq. (2.14).

6.3 Boundary-integral formulation and numerical approach

Note that the solution to electric potential is independent of the solution of the fluid flow, while the latter depends on the former through the particle dynamics in Eq. (6.2). Therefore, the Laplace and Stokes equations can be solved sequentially at each time step. Again, we utilize a boundary-element method to solve the governing equations. The electric potential, ϕ, is decomposed into a combination of the background potential, $\phi^\infty = -E_0 x$, and the disturbance potential, ϕ^D, generated due to the presence of the particles so that $\phi = \phi^\infty + \phi^D$. Following boundary-integral formulation, the disturbance potential at a point $\mathbf{x}_0$ that lies on the boundary, D (either of the particle surfaces), can be expressed using Eq. (3.14),

$$\frac{1}{2}\phi^D(\mathbf{x}_0) = -\int_D g(\mathbf{x}_0, \mathbf{x})[\mathbf{n} \cdot \nabla\phi^D(\mathbf{x}_0)]dS(\mathbf{x}) + \int_D \phi^D(\mathbf{x})[\mathbf{n} \cdot \nabla g(\mathbf{x}_0, \mathbf{x})]dS(\mathbf{x}), \tag{6.4}$$

where $\mathbf{n}$ is the surface normal pointing into the flow field which is outside of the particle volumes enclosed by, D. Under this condition, the following integral identity from Eq. (3.23) applies,

$$\int_D [\mathbf{n}(\mathbf{x}) \cdot \nabla g(\mathbf{x}, \mathbf{x}_0)]dS(\mathbf{x}) = -\frac{1}{2}. \tag{6.5}$$

by noting that $\mathbf{x}_0$ falls on the boundary D. If we express the second integral in Eq. (6.4) as

$$\int_D \phi^D(\mathbf{x})[\mathbf{n}\cdot\nabla g(\mathbf{x}_0,\mathbf{x})]dS(\mathbf{x}) = \int_D [\phi^D(\mathbf{x})-\phi^D(\mathbf{x}_0)][\mathbf{n}\cdot\nabla g(\mathbf{x}_0,\mathbf{x})]dS(\mathbf{x}) + \int_D \phi^D(\mathbf{x}_0)[\mathbf{n}\cdot\nabla g(\mathbf{x}_0,\mathbf{x})]dS(\mathbf{x}), \quad (6.6)$$

then we can use Eq. (6.5) to simplify it to the following form,

$$\int_D \phi^D(\mathbf{x})[\mathbf{n}\cdot\nabla g(\mathbf{x}_0,\mathbf{x})]dS(\mathbf{x}) = \int_D [\phi^D(\mathbf{x})-\phi^D(\mathbf{x}_0)][\mathbf{n}\cdot\nabla g(\mathbf{x}_0,\mathbf{x})]dS(\mathbf{x}) - \frac{1}{2}\phi^D(\mathbf{x}_0). \quad (6.7)$$

Implementing this adjustment into Eq. (6.4) allows us to remove the singularity and transform the integral equation for the laplace equation into

$$\phi^D(\mathbf{x}_0) = -\int_D g(\mathbf{x}_0,\mathbf{x})[\mathbf{n}\cdot\nabla\phi^D(\mathbf{x})]dS(\mathbf{x}) + \int_D [\phi^D(\mathbf{x})-\phi^D(\mathbf{x}_0)][\mathbf{n}\cdot\nabla g(\mathbf{x}_0,\mathbf{x})]dS(\mathbf{x}). \quad (6.8)$$

The fluid motion comes solely from the disturbances caused by the particle. To solve the flow, we use the boundary-integral formulation for the Stokes equation in 3D, Eq. (3.22) and express $\mathbf{u}$ at the point $\mathbf{x}_0$ that lies inside the fluid,

$$\frac{1}{2}u_j(\mathbf{x}_0) = -\frac{1}{8\pi\mu}\int_D G_{ji}(\mathbf{x}_0,\mathbf{x})f_i(\mathbf{x})dS(\mathbf{x}) + \frac{1}{8\pi}\int_D u_i(\mathbf{x})T_{ijk}(\mathbf{x},\mathbf{x}_0)n_k(\mathbf{x})dS(\mathbf{x}). \quad (6.9)$$

where $\mathbf{f} = \boldsymbol{\sigma}\cdot\mathbf{n}$ is the component of the hydrodynamic traction. Note that the dummy indices i, j, and k rotate among the components x, y, and z. In this equation, u_i and u_j are simply the rigid-body velocity components of the particles. Thus, the integral identities for 3D rigid-body motion, Eq. (3.26) can be used. After this simplification,

Eq. (6.9) reduces to,

$$u_j(\mathbf{x}_0) = -\frac{1}{8\pi\mu}\int_D G_{ji}(\mathbf{x}_0, \mathbf{x})\, f_i(\mathbf{x}) dS(\mathbf{x}). \tag{6.10}$$

After discretization, Eq. (6.10) will be used to formulate the algebraic system to obtain the hydrodynamic traction **f** on the particle surfaces. It is inherent in this formulation that the fluid velocity vanishes as **x** approaches infinity.

To discretize the integral equations, 3D particle surfaces are represented using six-node curved triangular elements. Variables pertinent to the electric field, i.e., ϕ and $\partial\phi/\partial\mathbf{n}$, are discretized at the six vertices of the elements. Variables pertinent to the flow, i.e., traction f_i and velocity u_i, are discretized at the element centroids. At each time step, the integral equation for the disturbance potential is solved first. Then, Eq. (6.10) is solved with unknown translational and rotational velocities of each particle. To match the total number of unknowns, additional equations in Eq. (6.2), expressing the total traction and the total torque on each particle are appended to the linear algebraic system. Note that in Eq. (6.2), the contribution of the Maxwell stress can be computed explicitly, once the electric field is obtained. Integrals over each element are carried out using the Gauss–Legendre quadratures, and the resulting linear equation systems are solved using the LAPACK library. The temporal update of the position and orientation of each particle is achieved using a second-order Runge–Kutta scheme. The element size of the mesh used in this study is adaptive and is based on gap distance between particles. That is, the local resolution of the mesh between the particles is increased to make sure that the small region is resolved sufficiently. An example of this adaptive technique is shown in Figure 6.4.

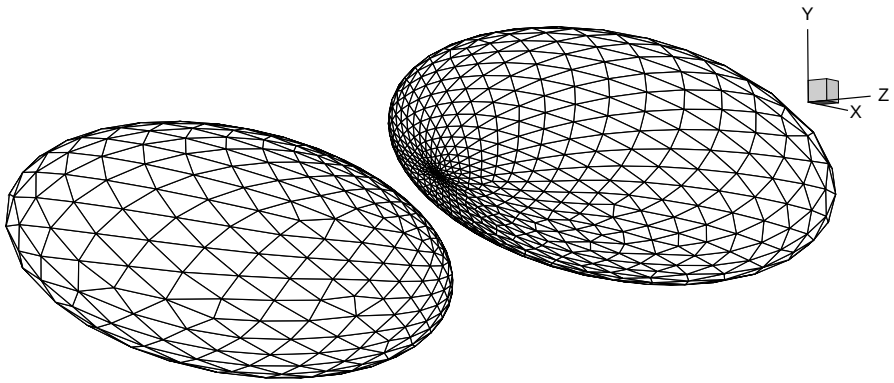

Figure 6.4: The adaptive mesh used in the BEM simulation. Elements forming the 3D particle surface are adapted in size in the narrow gap region when the two particles are in close proximity.

6.4 Code validation

The 3D BEM code used in this study has been validated for several geometric configurations in previous studies [71, 72]. In those validations, the resulting DEP force and electrophoretic velocity were compared to previously published results. In the present study, we are concerned with the DEP velocity of a non-conducting particle arising from a balance between the field-induced DEP force and resulting hydrodynamic drag. From this, it is appropriate that an additional validation be performed on the DEP mobility. To do so, we consider a non-conducting particle migrating away from a nearby plane wall under the transverse DEP force. The electric field is parallel to the wall. The exact DEP force normal to the plane wall was found previously by Young & Li [60].

In their work, they consider a non-conducting sphere positioned close to a non-conducting plane wall with an electric field is applied tangential to the plane wall. In this state, the non-conducting surfaces of the particle and wall will yield a greater electric field strength in the region between the two objects. This generates a net DEP force acting on the particle's field-induced dipole. To determine this force, the electric field must first be solved. The necessary solution of the electric potential comes from a modified analytical solution determined by Keh and Chen [109]. In their work, the thin-

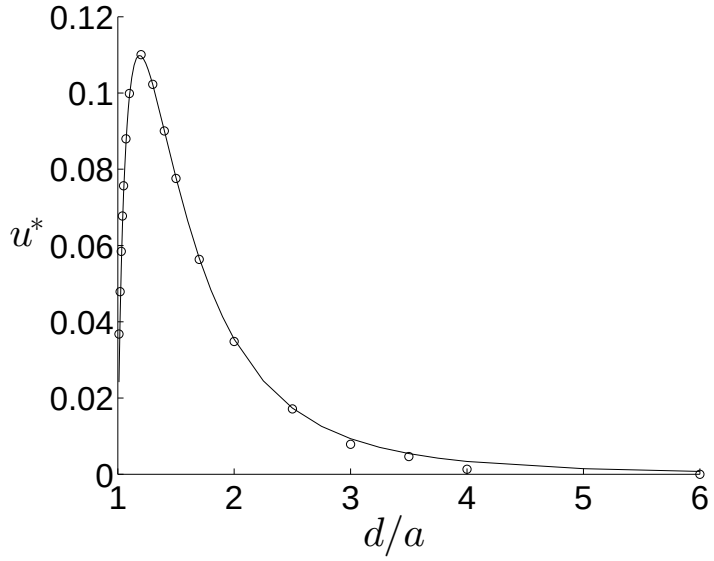

Figure 6.5: Nondimensional DEP velocity of a non-conducting sphere positioned close to a non-conducting plane surface under the influence of an electric field, E_0, directed tangential to the surface. The exact solution and present BEM solution are presented as a solid line and markers, respectively. The particle radius is a, and the distance between its center and the wall is d.

EDL assumption was employed to model the electric field using the Laplace equation. Then, the solution of the electric potential can be written in bispherical coordinates (ξ, η, φ) as

$$\phi(\xi,\eta,\varphi) = -cE_0\cos\varphi\Big[\frac{\sin\xi}{\cosh\eta-\cos\xi} - (\cosh\eta-\cos\xi)^{\frac{1}{2}} \times \sin\xi\sum_{n=1}^{\infty}(R_n\sinh(n+\tfrac{1}{2})\eta + S_n\cosh(n+\tfrac{1}{2})\eta)P_n'(\cos\xi)\Big]. \tag{6.11}$$

where $c = a\sinh\eta_0$, $\eta_0 = \cosh^{-1}(d/a)$, a and d are the particle radius and the distance of the particle center to the wall, respectively. Details for the coefficients, R_n, P_n and S_n can be found in the discussed reference [109]. The transformations for the bispherical coordinates are

$$x = \frac{c\sin\xi\cos\varphi}{\cosh\eta-\cos\xi}, \qquad y = \frac{c\sin\xi\sin\varphi}{\cosh\eta-\cos\xi}, \quad z = \frac{c\sinh\eta}{\cosh\eta-\cos\xi}. \tag{6.12}$$

In the work by Young & Li [60], they called upon an integration technique used by Swaminathan & Hu [106] to express the DEP force in the spherical coordinates. The resulting scalar force expression is one that is directed away from and perpendicular to the plane surface,

$$F_{\mathrm{DEP}} = -\frac{1}{2}\varepsilon_m a^2 \int_{\varphi=0}^{2\pi}\int_{\theta=0}^{\pi}\left[\left(\frac{1}{a}\frac{\partial\phi}{\partial\xi}\frac{\partial\xi}{\partial\theta}\right)^2 + \left(\frac{1}{a\sin\theta}\frac{\partial\phi}{\partial\varphi}\right)^2\right]\sin\theta\cos\theta\,\mathrm{d}\theta\,\mathrm{d}\varphi \qquad (6.13)$$

Note that F_{DEP} scales with $\varepsilon_m E_0^2 a^2$. The transformations for the spherical coordinates are

$$r = \sqrt{(z-d)^2 + x^2 + y^2}, \qquad \theta = \tan^{-1}\frac{\sqrt{x^2+y^2}}{z-d}, \quad \text{and} \quad \varphi = \tan^{-1}\frac{y}{x}. \qquad (6.14)$$

Table 6.1: Values of the nondimensional DEP velocity presented in Figure 6.5. The particle radius is a, and the distance between its center and the wall is d.

	$12\pi\mu u/[\varepsilon_m E_0^2 a]$	
d/a	Current study	Exact solution
1.01	0.03677	0.02416
1.02	0.04787	0.04104
1.05	0.07567	0.07354
1.10	0.09985	0.09910
1.20	0.11005	0.10972
1.50	0.07759	0.07779
2.00	0.03482	0.03541

The DEP force acting on the particle induces a repulsive motion. As the particle moves away from the plane wall, it experiences a counteracting hydrodynamic drag. Previously, Brenner [110] determined an analytical solution for the steady motion of a sphere moving orthogonal to a plane surface using bipolar coordinates. It is presented as,

$$F_{\mathrm{HYD}} = 6\pi\mu a u\lambda \qquad (6.15)$$

where λ is a correction factor given by

$$\lambda = \frac{4}{3}\sinh\eta_0 \sum_{n=1}^{\infty} \frac{n(n+1)}{(2n-1)(2n+3)}\left[\frac{2\sinh(2n+1)\eta_0 + (2n+1)\sinh 2\eta_0}{4\sinh^2(n+\frac{1}{2})\eta_0 - (2n+1)^2\sinh^2\eta_0} - 1\right]. \quad (6.16)$$

From the results presented by Brenner, it can be seen that $\lambda \to 1$ when $d/a \gg 1$. This allows us to recover Stokes' drag when the particle is far away from the plane surface. As the particle gets closer to the wall ($d/a \to 1$), the increasing effect of the correction can be seen as $\lambda \to \infty$. Thus, the presence of the wall results in a drag force greater than that of a unbounded particle.

By equating the modified version of Stokes' law in Eq. (6.15) to the DEP force described by Eq. (6.13), $F_{\mathrm{HYD}} = F_{\mathrm{DEP}}$, we can obtain the particle velocity. The analytical solution was evaluated using Mathematica. Details of the formulation can be found in the appendix. The nondimensional velocity, $u^* = 12\pi\mu u(\varepsilon_m E_0^2 a)$, obtained from this approach is presented alongside the results found using our BEM in Figure 6.5 and Table 6.1. As seen from the figure, the BEM code implemented in this work yields a high level of accuracy.

6.5 Results

6.5.1 Electro-orientation of a single prolate spheroid

Before discussing the interaction of two particles, we shall further examine the local reorientation of a single particle because a particle's electro-orientation will be coupled with the global orientation, as will be shown later.

It is well understood that in a DC field, a prolate spheroid particle will reorient itself such that its longest axis is parallel with the electric field (Figure 6.6(a)). This is because a non-spherical particle is in orientational equilibrium when its field-induced dipole (which, in this case, is in line with the major axis of the ellipsoid) is parallel with the field vector [10]. When its minor axis is parallel with the electric field, the particle

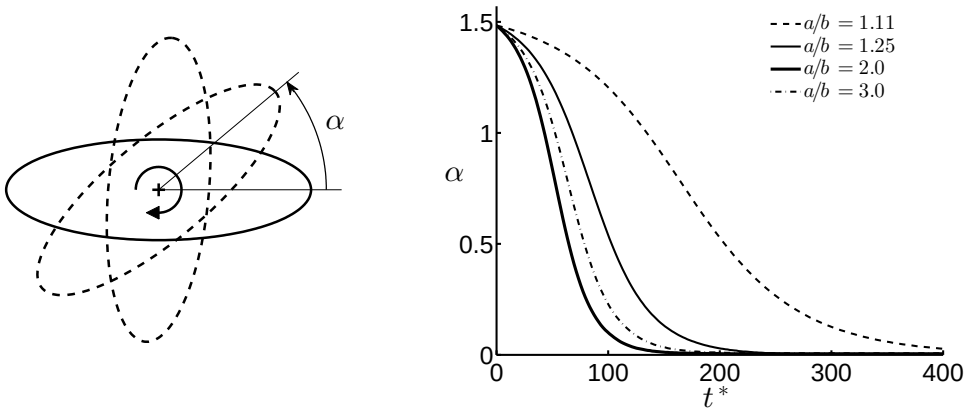

Figure 6.6: (*a*) A diagram of the electro-orientation process for $a/b = 3.0$ when the electric field is directed left to right. (*b*) The self-orientation angle of a single particle as a function of nondimensional time for various aspect ratios.

is in an equilibrium but unstable position. Figure 6.6(b) visualizes the self-orientation angle, α, of a single, unbounded particle as a function of the nondimensional time, $t^* = t\varepsilon_m E_0^2/\mu$, for four different aspect ratios: $a/b = 3.0$, 2.0, 1.25 and 1.11, where the angle between the long axis and the electric field is initially $\alpha_0 = 85°$. These results were obtained using our BEM code.

From the figure we can see the influence of the aspect ratio on the relaxation time, which we will define as the amount of time required for the particle's self-orientation angle, α, to fall below 1% of its initial angle. A constant electric field does not exert a torque on a spherical particle. This is because the local Maxwell stress in Eq. (2.14) is always in line with the surface normal and passes through the centroid of the particle. Therefore, we can expect that a nearly spherical particle has a greater relaxation time due to its reduced magnitude of the DEP torque. This is reflected well in Figure 6.6(b) as the relaxation time for $a/b = 1.11$ is roughly $t^* = 440$, the longest among the four cases.

For larger aspect ratios, the relaxation time is reduced. Specifically, for $a/b = 1.25$, 2.0 and 3.0, we see the nondimensional time of $t^* = 223$, 143, and 178, respectively.

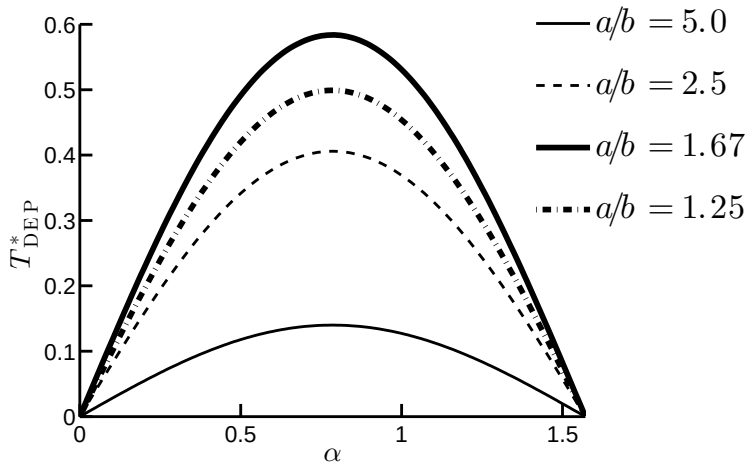

Figure 6.7: Normalized DEP torque as a function of the single particle's orientation with respect to the electric field.

It also becomes apparent from these values that there is a minimum relaxation time achieved with respect to the aspect ratio. This can be explained by the balance between the DEP and hydrodynamic torques, $T_{\mathrm{DEP}} = T_{\mathrm{HYD}}$. To further illustrate the torque balance on a single particle, we utilize existing analytical solutions for each torque. Jones [10] gave an analytical formula of the DEP torque acting on a single, unbounded ellipsoid of arbitrary orientation and a finite permittivity ratio with respect to its suspending medium, ε_p and ε_m, where ε_p and ε_m correspond to the permittivity of the particle and medium, respectively. For a non-conducting prolate spheroid particle ($\varepsilon_p \ll \varepsilon_m$), this relation is expressed in Eq. (2.21). The solution to this relation is plotted in Figure 6.7, where the nondimensional torque is defined as $T^*_{\mathrm{DEP}} = 2T_{\mathrm{DEP}}/(a^3\varepsilon_m E_0^2)$. The figure shows that for all the aspect ratios considered here, the maximum torque is achieved when $\alpha = \frac{\pi}{4}$. In addition, the DEP torque increases as the ratio a/b is decreased from 5.0 to 1.67, which is because a slender particle causes minor distortion to the electric field. On the other hand, the DEP torque for $a/b = 1.25$ drops below that for $a/b = 1.67$ since the former particle becomes close to a zero-torque sphere.

The hydrodynamic torque acting on a prolate spheroid rotating about its minor axis can be found in Wu [111]. Through fundamental singularities, the analytical solution

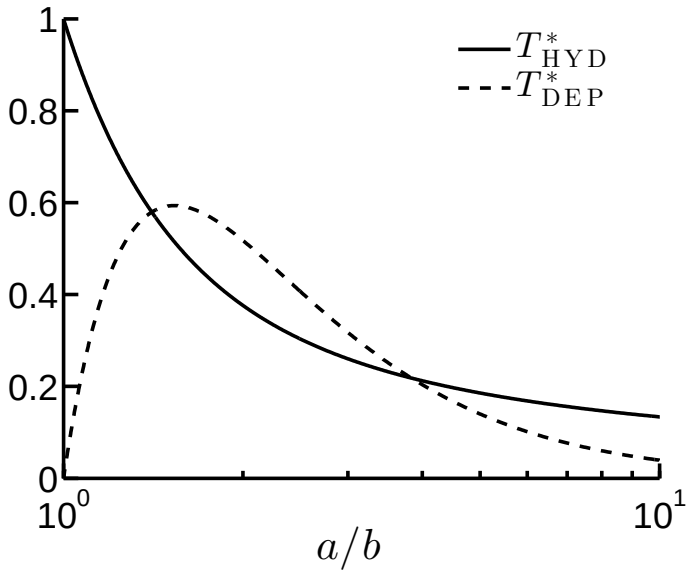

Figure 6.8: Normalized DEP and hydrodynamic torques as functions of the aspect ratio where the DEP torque shown is for $\alpha = \frac{\pi}{4}$.

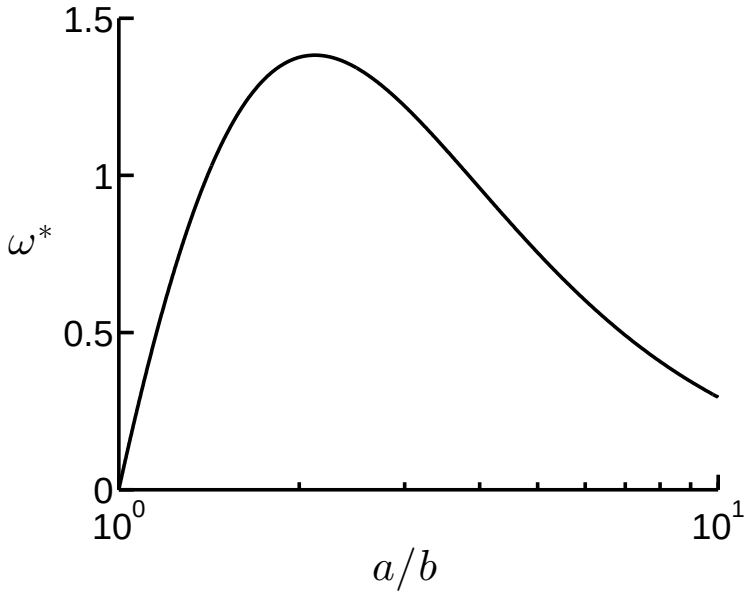

Figure 6.9: Rotational velocity at $\alpha = \frac{\pi}{4}$ (resulting from a balance of the hydrodynamic and DEP torques) as a function of the aspect ratio.

can be expressed as,

$$T_{\mathrm{HYD}} = \frac{32}{3}\pi\mu ab^2\omega e^3\left(\frac{2-e^2}{1-e^2}\right)\left[-2e + (1+e^2)\log\frac{1+e}{1-e}\right]^{-1} \tag{6.17}$$

where e, the eccentricity is defined as $e = \sqrt{1 - b^2/a^2}$. Defined as $T^*_{\mathrm{HYD}} = T_{\mathrm{HYD}}/(8\pi\mu a^3\omega)$, where ω is the rotational velocity, the normalized torque is plotted in Figure 6.8 as a function of a/b. Together shown in the figure is the aforementioned DEP torque assuming the orientation angle is at $\alpha = \pi/4$. For a spherical particle, $a/b = 1$, the normalized hydrodynamic torque takes its well-known value, $T^*_{\mathrm{HYD}} = 1$. An increasing aspect ratio results in a decreasing value of hydrodynamic torque. Equating the two torques, we obtain the electro-orientation velocity of a single particle as a function of the aspect ratio, as shown in Figure 6.9, where the angular velocity at the orientation angle $\alpha = \pi/4$ is defined as $\omega^* = 16\pi\mu\omega/(\varepsilon_m E_0^2)$. The result shows that the maximum angular velocity takes place near $a/b = 1.4$, which is consistent to the relaxation time observed in Figure 6.6(b).

6.5.2 Two particles: combined electro-orientation and global reorientation

Next, we shall observe the interaction of two particles and will start by considering arbitrary initial configurations. We will see that the transient motion of the particles largely depends on their initial positions.

Li [96] and Ai & Qian [97] showed that two spherical particles with an arbitrary initial orientation angle, θ, will globally rotate and reorient themselves so that they ultimately arrive in a tandem arrangement and finally they are attracted to each other. For two ellipsoids, we expect that both global and electro-orientation will occur. Therefore, we first consider the situation shown in Figure 6.10. In this alignment, each particle is nearly vertical with respect to the electric field and so is its own self-orientation angle. Here, we account for the simultaneous electro-orientation and global orientation

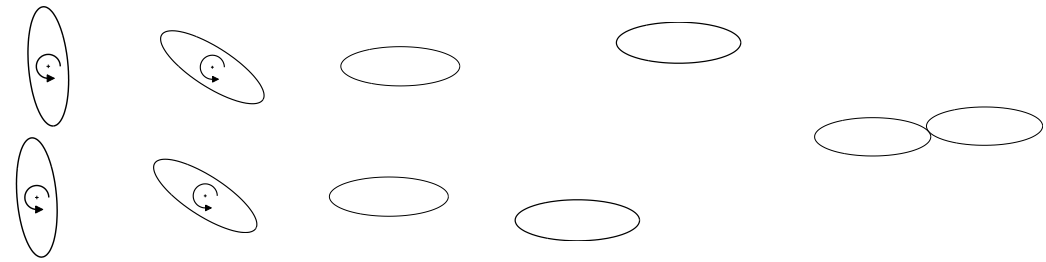

Figure 6.10: Combined electro-orientation and global reorientation of two interacting ellipsoids. Results are shown for the case of $a/b = 3.0$, $\theta_0 = 85°$, $\alpha_0 = 85°$, and $d_0/a = 2.2$. The electric field is directed left to right. Arrows represent the direction of T_{DEP}.

processes and how the combination influences interaction between the two particles. In doing so, we compare the time scale associated with the global reorientation to the time scale with the electro-orientation, i.e., the relaxation time.

Specifically, we consider two particles with $a/b = 3.0$ initially positioned at $\theta_0 = 85°$ and a center-to-center distance of $d_0/a = 2.2$. The particles are each initially oriented with respect to the electric field such that $\alpha_0 = 85°$. Figure 6.10 visualizes the interacting particles at various moments in time through the process. The example shows that each particle's relaxation time is much shorter than the time required for global orientation. In the case considered here, the electro-orientation is completed by $t^* = 132$, which is somewhat shorter than the relaxation time of a single particle reported in the previous section, $t^* = 178$. The difference can be attributed to the interaction between particles. The global reorientation, however, requires roughly $t^* = 18000$ and is even much longer that the relaxation time of a single particle with $a/b = 1.11$ shown in Figure 6.6(b).

In order to view the simulation from a dimensional perspective, we introduce relevant dimensional parameters. If we approximate the suspending medium as pure water ($\varepsilon_m = 6.9 \times 10^{-10}$ C/V·m, $\mu = 0.9 \times 10^{-3}$ kg/m·s), then under an applied field of 100 V/cm, we would expect electro-orientation of the particle in Figure 6.10 to be completed

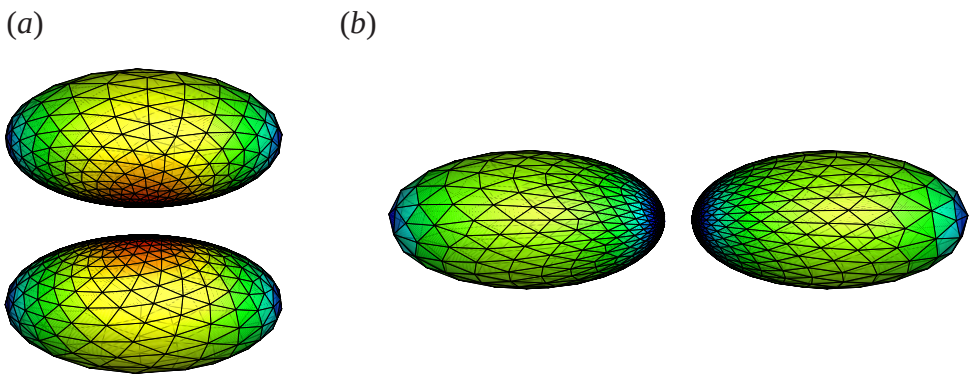

Figure 6.11: Surface plot of $|\mathbf{E}|^2$ for ellipsoidal particles oriented at (a) $\theta = 90^\circ$ and (b) $\theta = 0^\circ$. The electric field is directed left to right. Red shading represents a high field strength whereas blue represents weak field strength.

within 2 seconds while the entire global reorientation process would require close to 4 minutes.

The large difference in time scales between the two orientation processes implies that we can reasonably model the global orientation process for particles of arbitrary initial self-orientation by assuming that the particles have already completed the electro-orientation process. Complication arises when the two particles are very close to each other and their self-rotation is interfered by contact. Such special cases will be discussed in the end of this chapter.

6.5.3 Two particles at perpendicular ($\theta_0 = 90^\circ$) or parallel ($\theta_0 = 0^\circ$) alignments

First, we consider two particles initially positioned such that the line connecting their centers is either perpendicular ($\theta_0 = 90^\circ$) or parallel ($\theta_0 = 0^\circ$) with the electric field, where distortion of the electric field is symmetric. Such distortion leads to a DEP force that is attractive for the parallel case or repulsive for the perpendicular case, and the two-particle system does not globally rotate. Figure 6.11(a) displays a surface plot of $|\mathbf{E}|^2$ for the case of $\theta = 90^\circ$. Here, we can see that a region of strong electric field forms between the particles. This yields a mutual DEP force that would repel the two particles away from each other along a straight line. As shown later, this globally

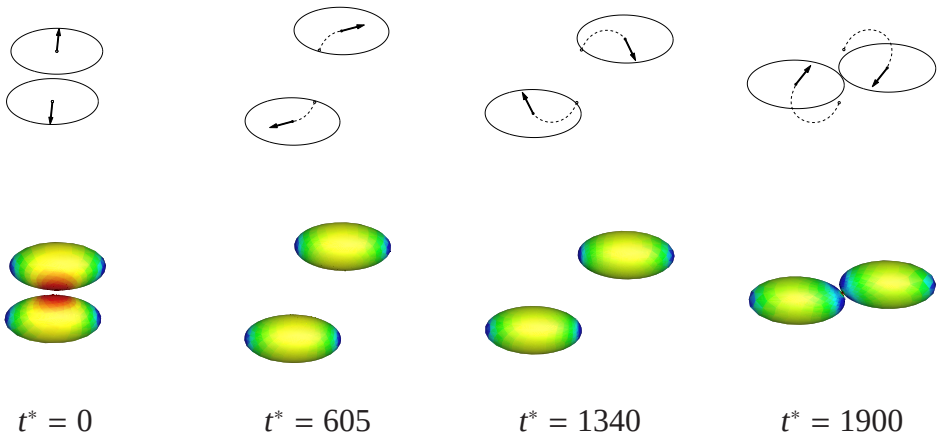

Figure 6.12: Global reorientation of two ellipsoids, where the electric field is applied left to right. Results are shown for the case of $a/b = 2.0$, $\theta_0 = 85°$ and $d_0/a = 1.1$. Vectors represent the direction of F_{DEP}. The corresponding contour plot of $|\mathbf{E}|^2$ is shown on the lower row.

perpendicular orientation is unstable. That is, a disturbance in either direction would produce a DEP force component that would ultimately lead to chain formation. Figure 6.11(b) displays a similar plot for the case of $\theta = 0°$. Contrastingly, this parallel orientation produces a region of low-strength electric field between the particles. The resulting mutually attractive DEP force drives the particles toward each other, also along a straight line. A detailed discussion of these two distinct orientations was presented by Ai & Qian [97] for the case of two spherical particles.

6.5.4 Global reorientation with initial configuration $0° < \theta_0 < 90°$

Next, we consider the case when two particles initially have a global orientation angle, $0° < \theta_0 < 90°$. Here, the distorted electric field exhibits a *two-fold* rotational symmetry about the z-axis that passes through the midpoint between the two particles. The mutual DEP force causes the two particles to translate in curved paths and so their centers rotate clockwisely. An example of this reorientation process is depicted in Figure 6.12. Recall that if either of these particles were present under the same conditions without the presence of the second particle, there would not be a net DEP force. There-

fore, the perturbed electric field and its asymmetry have led to a net DEP force that is equal in magnitude but opposite in direction for the two particles, as shown in Figure 6.12. In this case, the particles start with $\theta_0 = 85°$, when the DEP force is nearly vertical and repulsive. As the particles move away from each other, they also slightly shift horizontally, which creates greater asymmetry and causes the DEP force to become nearly horizontal ($t^* = 605$). Later, as the horizontal shift becomes sufficiently large (and θ becomes small), the DEP force becomes attractive in the vertical direction while remaining to be repulsive in the horizontal direction ($t^* = 1340$). In the end, the force becomes completely attractive, and the particles move toward each other ($t^* = 1900$) along a small global orientation angle.

Previous experimental study [98] has shown that densely distributed ellipsoidal particles that are initially arranged in a random manner will tend to form chains. These chains are shown to have a distinct angle with respect to the direction of the electric field, similar to the current observations from a two particle configuration. Therefore, the transient behavior and particle-particle interaction exhibited in the current study could be used as the fundamental mechanism to explain the phenomenon in the experiment.

To systematically investigate the global reorientation of two particles, we vary the initial orientation and distance between the two particles and run a series of simulations to obtain the particle trajectories and the final orientation angle. Three aspect ratios, $a/b = 1.0$, 2.0, and 3.0, are considered in this study. Contact mechanics is not considered in this study, and the numerical simulation would eventually break down if the gap between the particles is sufficiently small. Thus, we define a threshold for the gap distance at which the two particles are deemed to be at the terminal configuration. Although predicting the particle motion beyond the threshold is not considered here, from the directions of their final translational velocity it is reasonable to believe that the particles will form a stable pair after contact.

Figure 6.13 visualizes this reorientation process for several cases from the simula-

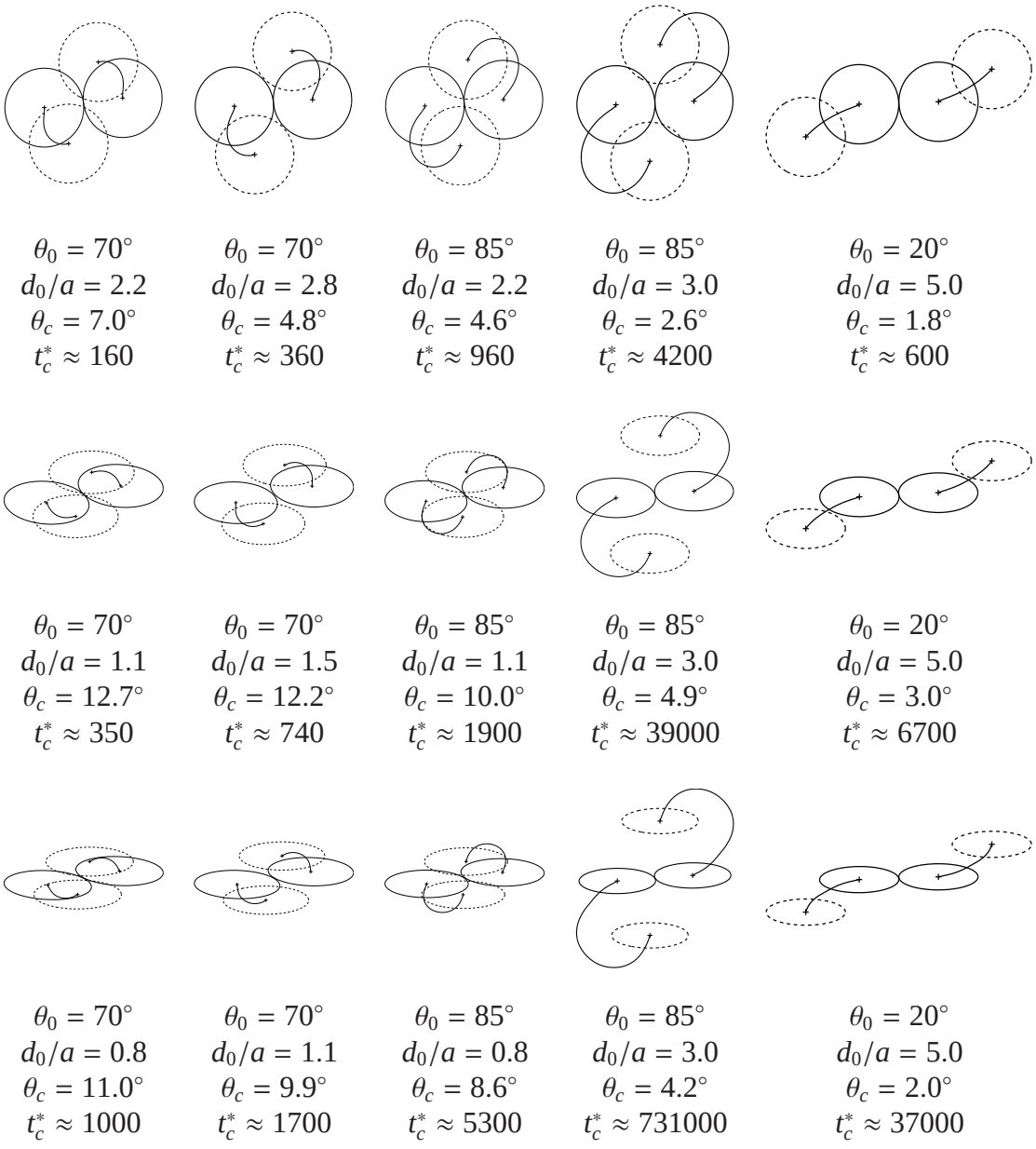

$\theta_0 = 70°$ $d_0/a = 2.2$ $\theta_c = 7.0°$ $t_c^* \approx 160$	$\theta_0 = 70°$ $d_0/a = 2.8$ $\theta_c = 4.8°$ $t_c^* \approx 360$	$\theta_0 = 85°$ $d_0/a = 2.2$ $\theta_c = 4.6°$ $t_c^* \approx 960$	$\theta_0 = 85°$ $d_0/a = 3.0$ $\theta_c = 2.6°$ $t_c^* \approx 4200$	$\theta_0 = 20°$ $d_0/a = 5.0$ $\theta_c = 1.8°$ $t_c^* \approx 600$
$\theta_0 = 70°$ $d_0/a = 1.1$ $\theta_c = 12.7°$ $t_c^* \approx 350$	$\theta_0 = 70°$ $d_0/a = 1.5$ $\theta_c = 12.2°$ $t_c^* \approx 740$	$\theta_0 = 85°$ $d_0/a = 1.1$ $\theta_c = 10.0°$ $t_c^* \approx 1900$	$\theta_0 = 85°$ $d_0/a = 3.0$ $\theta_c = 4.9°$ $t_c^* \approx 39000$	$\theta_0 = 20°$ $d_0/a = 5.0$ $\theta_c = 3.0°$ $t_c^* \approx 6700$
$\theta_0 = 70°$ $d_0/a = 0.8$ $\theta_c = 11.0°$ $t_c^* \approx 1000$	$\theta_0 = 70°$ $d_0/a = 1.1$ $\theta_c = 9.9°$ $t_c^* \approx 1700$	$\theta_0 = 85°$ $d_0/a = 0.8$ $\theta_c = 8.6°$ $t_c^* \approx 5300$	$\theta_0 = 85°$ $d_0/a = 3.0$ $\theta_c = 4.2°$ $t_c^* \approx 731000$	$\theta_0 = 20°$ $d_0/a = 5.0$ $\theta_c = 2.0°$ $t_c^* \approx 37000$

Figure 6.13: DEP trajectories for various initial conditions (indicated by dashed lines). The first, second, and third rows correspond to aspect ratios of $a/b = 1.0$, 2.0, and 3.0, respectively. The initial (θ_0) and final (θ_c) angle are presented along with the initial separation (d_0/a) and the travel time, t_c.

tion series. The initial and final configurations as well as the transient trajectories are plotted in the figure. The orientational angle just prior to contact, θ_c, and the time taken to complete the travel, t_c^*, are provided for each case. Several observations can be made from this figure. First, for all the cases shown, including the spherical shape, the particles finally reach an oblique configuration that has a chaining angle with respect to the direction of the electric field. The chaining angle in these cases are less than 13°, and it depends on both the initial configuration and the aspect ratio of the particles. For example, considering the spheres ($a/b = 1.0$), if we compare the two cases at $\theta_0 = 70°$, or the two cases at $\theta_0 = 85°$, we can see that increasing the initial particle distance d_0 while keeping θ_0 constant would lead to a smaller chaining angle. On the other hand, keeping the initial distance constant while increasing θ_0 could lead to a smaller chaining angle as well. A comparison of the two cases with $\theta_0 = 70°$ or 85° and $d_0/a = 2.2$ illustrates this argument. Furthermore, when the particles are far apart, e.g., $\theta_0 = 20°$ and $d_0/a = 5.0$, the chaining angle could also be small (less than 2°), and the two particles are almost parallel with the electric field. For the other two geometric ratios, $a/b = 2.0$ or 3.0, we can observe the similar trend of the chaining angle as θ_0 or d_0 is varied. However, for slender particles, the time required for global reorientation is typically much longer compared to the time for bluff particles. This result can be attributed to the fact that a slender particle causes less distortion to the electric field and thus induces a lower DEP force. In addition, the effective distance between the two particles (equivalent to the gap width) is larger for two slender particles when compared to that of bluff particles under the same center-to-center distance, which leads to a weaker particle–particle interaction.

As seen in the experiment with densely distributed particles [98], the reported chaining angle is $16 \pm 5°$ for particles of approximate aspect ratio $a/b = 3.0$. The closest case in our study to the experimental condition would be $a/b = 3.0$, $\theta_0 = 70°$, and $d_0/a = 0.8$, where the chaining angle is $\theta_c = 11°$. This angle is smaller compared to what was seen in the experiment, possibly due to the fact that only two particles are being considered

here.

To get a better view how the initial configuration affects the particle chaining, we plot a map of the particle motion by grouping the trajectories with different θ_0 and d_0 into one single figure, which is shown in Figure 6.16 for the three aspect ratios. On the map, the trajectories display a pattern that consists of a family of open rings that originate near the *y*-axis and end near the *x*-axis. These rings do not cross over each other. The particles could start at any point initially on a loop. They will then follow the trajectory and complete the rest of the path. Note that to initiate the global rotation and also to shorten the simulation time, we have used $\theta_0 < 90^\circ$ so that the start location is just off the *y*-axis. In addition, the trajectories can not be extended much further in the map since at the start and end points, there is a minimal gap between the two particles.

In the results published by Ai and Qian [97], they report that a slight dependence of particle trajectory on electric field strength. In more detail, it is explained that a stronger electric field yields a curved trajectory that is outside that of a weaker field. In other words, the two particles would be farther apart at the same θ for a greater value of E_0. We point this out because our studies yield a different result. Here, we would like to point out that the externally applied electric field strength, E_0, has no effect on particle trajectories. This is because both the electric field and flow are governed by linear functions. Raising E_0 will increase the DEP force quadratically, as indicated in Eq. (2.14). Since the counteracting hydrodynamic drag is linearly proportional to the velocity, the translation of the particles would increase quadratically as well. However, the directions of the DEP force and velocity would not depend on the amplitude of E_0. It is important to note, however, that increasing the field strength will certainly reduce the orientation times discussed herein.

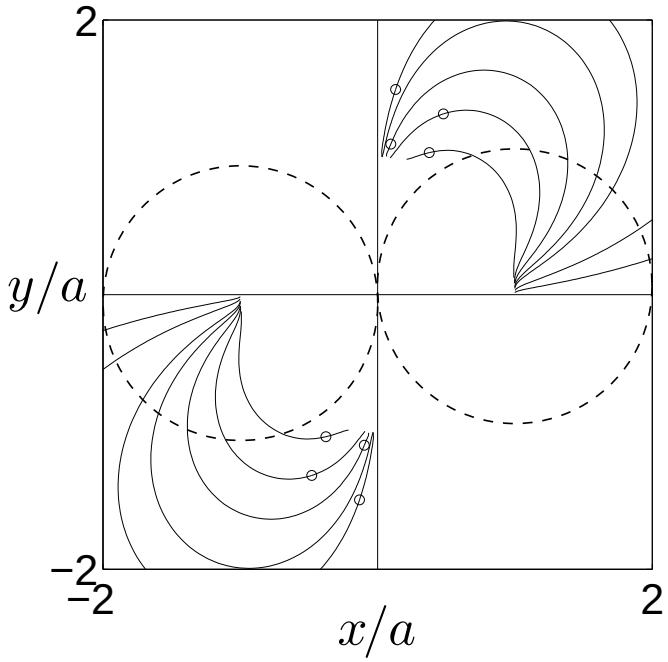

Figure 6.14: Trajectory map for $a/b = 1.0$. Dashed ellipses represent approximate final configurations. Open circles correspond to the cases visualized in Figure 6.13.

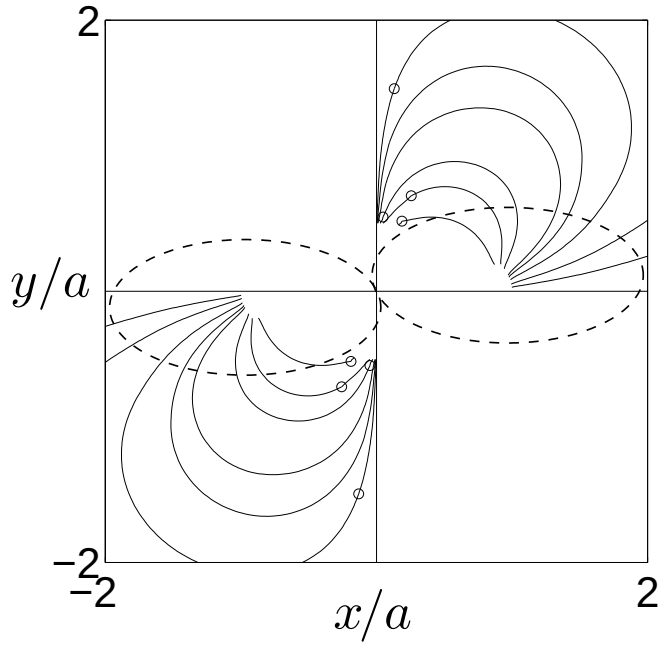

Figure 6.15: Trajectory map for $a/b = 2.0$. Dashed ellipses represent approximate final configurations. Open circles correspond to the cases visualized in Figure 6.13.

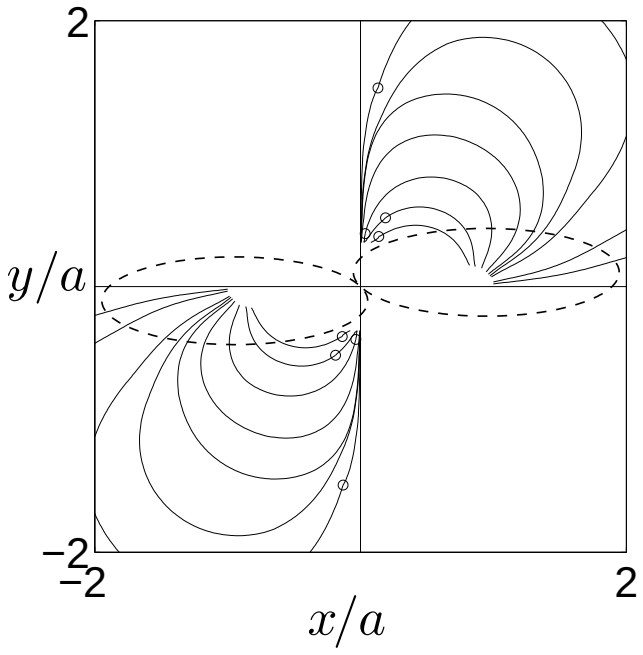

Figure 6.16: Trajectory map for $a/b = 3.0$. Dashed ellipses represent approximate final configurations. Open circles correspond to the cases visualized in Figure 6.13.

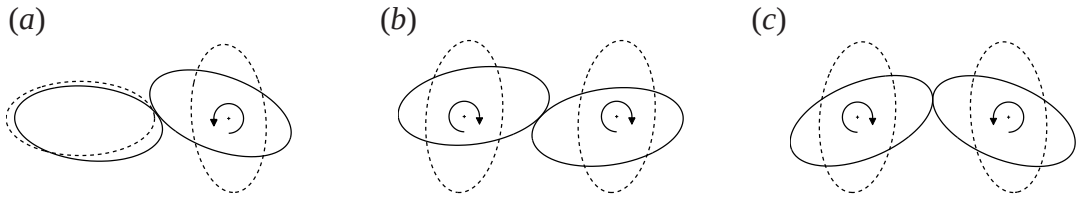

Figure 6.17: Particles under electro-orientation when they are initially positioned close to one another (as indicated by dashed lines). Results are shown for the case of $a/b = 2.0$, $\theta_0 = 0°$, $d_0/a = 2.0$. An initial perturbation of 5° has been applied to each nearly vertical particle.

6.5.5 Particles interacting without sufficient separation

As mentioned earlier, two particles with arbitrary initial self-orientation will go through a combined rapid electro-orientation and slow global orientation. If the particles are positioned too close to each other, their self-alignment process could be interfered due to contact. Examples of this situation can be found in Figure 6.17, where the particle centers are in tandem arrangement with $d_0/a = 2.0$ but each particle may have arbitrary orientation. The two particles move toward each other while they are rotating. The reduced separation causes the particle to contact before they could finish electro-orientation. Further motion of the particle pair would depend on the nature of the contact. In this situation, the final configuration is case-specific and does not have a general pattern as seen in earlier discussion. A similar situation was also seen in the experiment by Singh *et al.* [98], where the electro-orientation interference from this close-range interaction was discussed as “jamming".

6.6 Conclusion

In this study, we investigate the fundamental mechanics of non-spherical particle coalescence under the dielectrophoretic effect. To do so we have utilized a three-dimensional boundary-element method to model the transient motion of two interacting non-conducting prolate spheroids under a DC electric field. In our approach, we perform surface integration of the Maxwell stress tensor, and the viscous drag is obtained by solving the Stokes flow.

Combining previously available analytical solutions for the hydrodynamic and dielectrophoretic torques, we first identified an aspect ratio that minimizes the relaxation time for electro-orientation of a single particle. As the numerical simulation shows, the electro-orientation of the particles is much faster than the global reorientation. Based on this observation, we modeled the relative motion of two particles whose field-induced dipole is already parallel with the field vector. With this model, we clarified the mech-

anism that drives the ellipsoidal particles to form a stable chain. The transient motion of the particles and their chaining angle are generalized in a trajectory map for the particles with a constant aspect ratio. In particular, when the particles are initially closely separated, the chaining angle resembles what was observed in a previous experiment of densely distributed particles. Therefore, this study provides a possible mechanism to explain the experimental phenomenon. We have further studied the relationship between the initial separation of the particles and the final chaining angle. It was shown that particles of higher aspect ratios tend to form reduced chaining angles and require more time for self-assembly. Trajectories and chaining angles discussed are shown to be independent of field strength.

CHAPTER VII

CONCLUSIONS

7.1 Summary of present work

The ability to rapidly detect disorders or infectious agents is of superlative importance within the medical community. While still young in its development, lab-on-a-chip technology has shown signs of an auspicious future in which bacteria, diseases and viruses can be quickly and accurately detected and subsequently treated. Required of this technology is the ability to manipulate colloidal materials at the micron scale. The recent expansion of microfluidic studies has helped identify and exploit fundamental phenomena to improve our level of control over the biological suspensions used in these LOC devices. Increasingly popular within the field of microfluidics is the use of electric fields to drive actuation. This technique does not require mechanical, moving components. Instead it uses electrodes that are fabricated by straightforward techniques. A potential bottleneck to the future LOC devices is the repeatability of the assays they perform. Precision is a challenging demand when operating with particles and fluidic channels at length scales of 1-100 μm. However, it is this same demand of precision that sets the efficacy required for a positive future of the technology.

Driven by this demand, many researchers have worked to answer some of the more fundamental questions regarding electrokinetic effects in microfluidics. Still, there is more to be understood regarding the complex electrokinetic behavior of colloidal particles. Some researchers choose to employ approximations that are simple and efficient, but limited in their accuracy. Others derive and utilize analytical solutions, however, these are available only for elementary geometries and conditions. Numerical approaches that use volume meshes such as a finite-element method are capable, but in-

efficient for systematic studies required in the design and optimization of microfluidic networks. They are also inaccurate under conditions where a high resolution volume mesh is required. Thus, there is need for an alternative numerical technique in the study of electrokinetic effects. To help resolve this need, the goal of this work is to aid in the expansion of applications of the boundary-element method to incorporate electrokinetic effects in microfluidics. In this dissertation, we present the BEM as an alternative technique and implement it to investigate situations that are not well-suited for the aforementioned techniques.

The body of work discussed herein can be broken into three sections. In Chapter IV, we implemented our two-dimensional BEM to study the influence of parallel walls on the electrophoretic mobility of a cylindrical particle. Previous studies using single walls have shown an increase in mobility as the particle approaches the wall due to distortion of the electric field in the gap region. What we were able to to show, however, is that in the case of two bounding walls this “enhancement" can be mitigated by the viscous drag induced by the second wall. Notably, when the particle and channel wall are comparable in size, the viscous effect is comparable to that of electrophoresis. By utilizing our 3D BEM code, in Chapter V, we were able to study the effect of dielectrophoresis on a spherical particle moving through a bent cylindrical channel. The shape of the channel creates a non-uniform electric field, which induces a DEP force that “pushes" the particle away from the inside corner. Our study clarifies the effect under various field strengths, sizes and initial positions. As the particle becomes close to the wall, its finite size has an increasingly important effect on its own transient motion. By comparing our results with those using a common approximation (PDM), we were able to clarify the limitations of the approximation. The next step was to extend our 3D BEM code to incorporate two particles and also to model non-spherical particles. With these modifications in place, in Chapter VI we were able to study the DEP interaction that takes place between two slender particles in the vicinity of each other. Here, we clarify the chaining mechanism between slender particles and observe the dependence of its

final chaining angle on particle aspect ratio.

7.2 Limitations of present work

When using the results reported in this dissertation, it is important to consider their limitations. Several assumptions are inherent in the numerical model which may not be suitable under extreme conditions. As discussed before, Joule heating is a natural occurrence in electrokinetic applications. This can lead to non-uniform temperatures within the medium, altering its mechanical, electrical and chemical properties [112, 113]. Joule heating is more significant at high field strengths and should be monitored in experiments. We also do not consider DLVO-type interactions that can occur if two surfaces are significantly close to each other. This classical theory encompasses van der Waals forces and EDL interactions. Our method assumes negligible EDL thickness and van der Waals contributions. These interactions would be more significant at smaller length scales ($< 1\ \mu$m). An electrokinetic effect that is not considered is electrodeformation [114]. This is surface deformation arising from the field-induced stresses. Our simulations assume all particles and channel walls are rigid. The relevance of deformation is dependent upon the particles used. Lastly, our model is developed around the linearity of Stokes equations. If channel dimensions are large enough and yield increased values of Reynolds number, inertial effects must also be considered.

7.3 Contributions of present work

The first objective of this work was to advance the application of the boundary-element method within electrokinetics in microfluidics. In meeting this objective, we provide several key contributions to the field.

- We have developed the 2D and 3D boundary-integral formulations for the electrokinetic motion of particles in microchannels. These formulations were then

utilized to construct both a comprehensive 2D and 3D BEM code based on a previous solver for Stokes flow.

- Implementing these codes, we have demonstrated the effectiveness of the BEM as an accurate alternative to other numerical techniques. It has been applied in three studies whose geometries would be computationally demanding for numerical techniques limited by volume discretization.

- As a proof of its accuracy, each study is accompanied with a thorough validation. Each of these validations include a comparison of our BEM results with those obtained through analytical techniques for similar geometries. For each of the comparisons, the BEM achieved significantly high levels of accuracy.

- To justify the need for a numerical technique, we compare results obtained using our BEM to those obtained using a point–particle approach. This comparison exemplifies the inaccuracies obtained without accounting for the finite size of the particle.

Another objective of this work was to utilize the developed BEM to study the fundamental electrokinetic motion of particles. In this respect, we contribute the following concepts identified in the studies herein.

- When bound by two parallel walls, the viscous effect acting on a tightly-bound cylindrical particle is comparable to its electrophoretic effect. In addition, the particle's rotational velocity is sensitive to its eccentricity.

- The size of a spherical particle has an increasingly significant effect on its own transient motion when traversing through a bent pore. This is especially true if the particle is positioned close to the wall.

- Lastly, with sufficient distance, electro-orientation has little or no effect on the field-induced chaining of slender particles. The final chaining angle formed be-

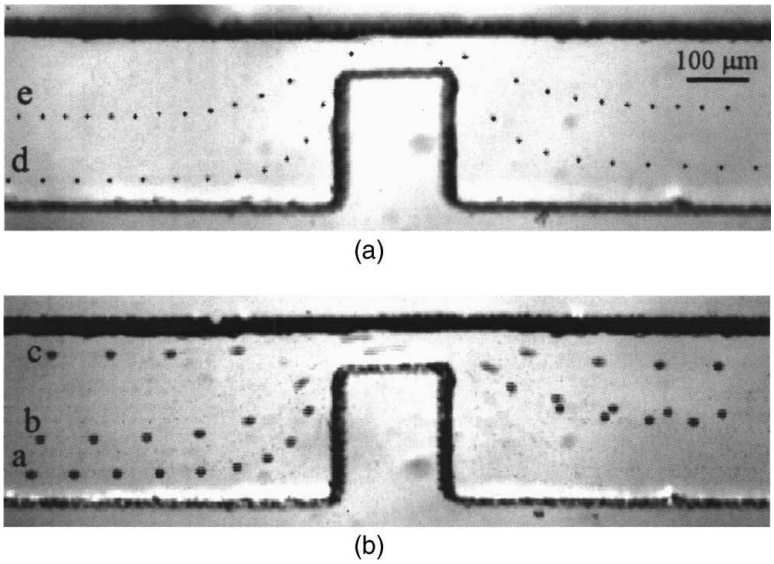

Figure 7.1: Experimental results of DC-DEP effect created by insulating hurdle for (*a*) 2.85 μm and (*b*) 7.85 μm particles reported by Kang *et al.* [41].

tween two particles is dependent upon the aspect ratio of the particles. The mechanism reported in our study serves as rationale for the observed experimental phenomenon.

7.4 Directions for future work

7.4.1 Characterization of hurdle-based DC-DEP for particle manipulation

With the three-dimensional BEM code in place and validated, there are several directions that one could choose to extend its application within electrokinetics. As a proven numerical method, one could utilize the code in an effort to optimize microchannel design associated with certain DEP techniques. One example of this is the hurdle-based DEP. This technique is often applied to particle separation by size or electrical properties. There are several geometric approaches in the design of these hurdles such as the rectangular, triangular, spiraling or serpentine. The advantage of implementing a BEM code to optimize the geometric parameters governing microchannel design, is its efficiency. A systematic study on these parameters would be a useful and straightfor-

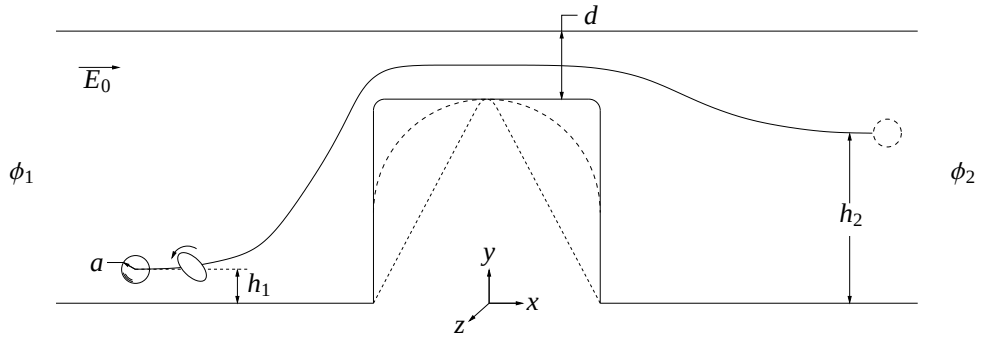

Figure 7.2: Schematic of a microchannel design used for particle separation based on DC-DEP from an insulating hurdle. Dashed lines represent potential hurdle shapes. The trajectory shown is what would be expected of a non-conducting particle when traveling through the DC-DEP mechanism.

ward extension of the work detailed in Chapter V. As an example, Figure 7.2 depicts the variables that could be used in a simple study to design and optimize the hurdle conditions. The problem specification in this study would be identical to those of the studies performed in this dissertation. In fact, we completed a preliminary test to observe the effect of particle size from a rectangular hurdle. Figure 7.3 plots the results of this test. The three trajectories depicted represent the three different particle sizes: $2a/d = 0.125$ (solid line), 0.250 (dashed line) and 0.375 (dash-dotted line). Each of the particles was initially positioned at $h_1/d = 1.25$. The overall channel is $37.5d$ long (L), $6.25d$ wide and $1.25d$ deep in the x, y and z directions, respectively. If we define the nominal electric field strength as $E_0 = (\phi_1 - \phi_2)/L$, and its non-dimensional counterpart as $E_0^* = E_0(d/\zeta_p)$, then the value of E_0^* was held constant at 16.0. As was expected, the larger particles deviated farther from their original streamline while moving around the hurdle. The final deviations for each of the particles from smallest to largest was h_2/d = 2.45, 3.30 and 4.05. Our results matched those reported by Kang *et al.* [41, 115] as seen in Figure 7.1

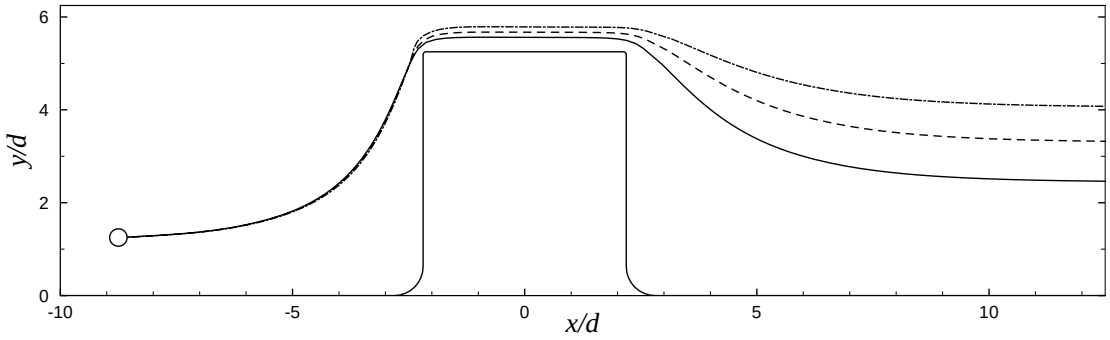

Figure 7.3: Results for a DC-DEP simulation using a square hurdle and a non-dimensional, nominal electric field strength of $E_0^* = 16$ at varying particle sizes: $2a/d$ = 0.125 (solid line), 0.250 (dashed line) and 0.375 (dash-dotted line).

7.4.2 Characterization of embedded electrode AC-DEP for particle manipulation

As mentioned before, alternating current is also used when implementing DEP. There are advantages to using AC-DEP that make it favorable under certain conditions. To model the effect of AC-DEP, modifications are necessary to account for the time-varying field. The conductivity and permittivity of suspended particles are a function of the frequency of the applied field. This results in a distinct response over a range of frequencies depending on the type of particle you are modeling. In fact, there exists a cross-over frequency where the direction of the DEP force reverses (from negative to positive DEP). This occurs when the permittivity of the particle approaches that of the suspending medium. To generate a non-uniform field using alternative current, asymmetric electrode geometries must be used [116–118]. In these studies, continuous separation of particles is achieved by utilizing pressure-driven flow to move the particles through a separation region. One of several designs proposed by Barbaros Çetin *et al.* [119, 120] makes an effort to reduce the size of the separation region. In this design, a more narrow region is generated using two planar copper electrodes, one on each side of a rectangular channel. It is believed that this can serve to further reduce the negative effects on cells induced by overexposure to electric fields.

In a recent unpublished study by Barbaros Çetin, a comparison was made between the resulting trajectories using two numerical approaches to model his planar AC-DEP design. Similar to our study [72], the comparison was made between a point-dipole method and full integration of the Maxwell stress tensor over the surface of the particle. Qualitatively, the results were similar, but the simplified point-dipole method yielded significant error resulting in over- and under-shooting trajectories. In these 2D simulations, commercial software (COMSOL) used a finite-element approach to utilize the more accurate Maxwell stress tensor approach. This required re-meshing between time steps that caused the software to become unstable and crash during longer trajectory simulations. Thus, there is need for a BEM study to complete an optimization to enhance separation effectiveness. Specifically, studies could be performed on the following parameters: electrode size, channel geometry (aspect ratio), particle size, particle shape, initial location.

Figure 7.4 shows a schematic of what the problem setup may look like. In this design, specified electric potential would be used at the surface of each electrode. By designing the channel to be sufficiently long, one could approximate the inlet and outlet potentials as zero. Electric potential would no longer the driving force behind bulk flow because the electrodes are positioned across the width of the channel instead of its length. Therefore a pressure gradient would be required to move the particle through the channel by means of the induced hydrodynamic force. To simulate this, different values of traction would be specified at the channel inlet and outlet. Note that the slip velocity along the channel walls will be approximately zero in regions distant from the electrodes. Because there is no EDL at the electrode surface, a no-slip boundary condition would be applied.

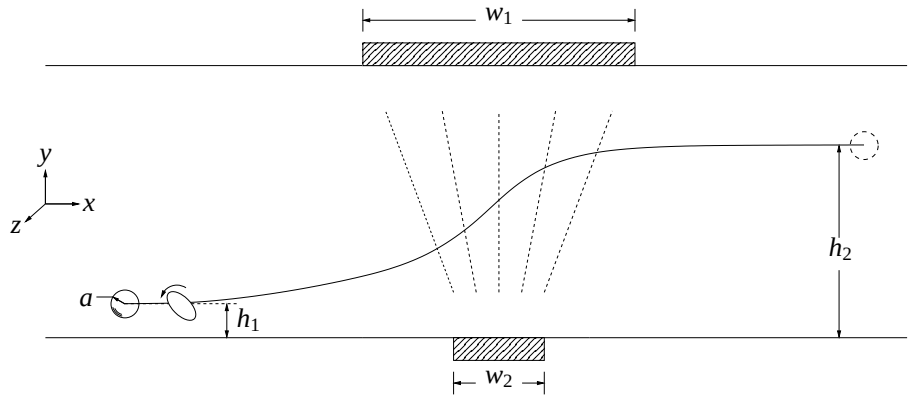

Figure 7.4: Schematic of a microchannel design used for particle separation based on AC-DEP from 3D asymmetric electrodes. Dashed lines represent the electric field lines. The trajectory shown is what would be expected of a non-conducting particle when traveling through the AC-DEP mechanism.

7.4.3 Other future studies

For non-spherical particles in an alternating field, the frequency-dependent permittivity results in multiple orientational equilibrium positions. In general, an ellipsoid would still have one “relaxed" orientation for a given frequency, however, this relaxed orientation would be a function of its frequency-dependent permittivity. In the case of an ellipsoid with three distinct axes, it would have three different orientations in which it would be considered relaxed. This could prove useful in self-assembly applications. Thus, one could use the current BEM to model this frequency-dependent interaction.

Interest has been developing for a numerical model capable of accounting for deformation of soft particles in electrokinetic flows. Researchers have shown relationships between deformability and health status for certain cells [114]. Such a trait could potentially be exploited for characterization and diagnostics applications. As the BEM computes the total stress acting on the particle surface, it would serve as a capable technique in this area. To extend the code to incorporate deformation, one would have to account for the elasticity of the cell membrane.

There are several more immediate extensions of the current BEM code as well. For example, modeling particles of arbitrary shapes. It has been shown previously, that par-

ticles of more complex shape can be used to aggregate into desired patterns [99, 100]. Also, biological particles can be irregularly shaped. Thus, to ensure that microfluidic chips are flexible enough to account for arbitrarily-shaped particles, it is necessary that they are optimized for a variety of shapes. The BEM would provide a useful numerical technique for predicting the behavior of complex particle shapes. In addition, one could study the interaction of multiple particles. In the present work, only up to two particles are considered. Another area that needs investigating is the interaction of particles within bounded flow. Previous researchers have observed interactions between particles traversing a microfluidic channel. These particles tend to chain, which interferes with DEP separation studies. It would be useful to model this interaction in the presence of boundaries for two or more particles to identify its impact on DEP manipulation techniques. At its present stage, the BEM code is capable of handling each of these simulations.

REFERENCES

[1] Daniel M., Haeberle S., Roth G., von Stetten F., and Zengerle R. Microfluidic lab-on-a-chip platforms: requirements, characteristics and applications. *Chem. Soc. Rev.*, 39:1153–1182, 2010.

[2] Pethig R. Review article–dielectrophoresis: status of the theory, technology and applications. *Biomicrofluidics*, 4:022811, 2010.

[3] Li D. *Electrokinetics in Microfluidics*. Elsevier, 1 edition, 2004.

[4] Chakraborty S. *Microfluidics and Microfabrication*. Springer, 2010.

[5] Kang Y and Li D. Electrokinetic motion of particles and cells in microchannels. *Microfluid. Nanofluid.*, 6:431–460, 2009.

[6] Hardt S and Schönfeld F. *Microfluidic technologies for miniaturized analysis systems*. Springer Science, 2007.

[7] Chang HC and Yeo LY. *Electrokinetically driven microfluidics and nanofluidics*. Cambridge University Press, 2010.

[8] Abramson HA. *Electrokinetic phenomena and their application to biology and medicine*. The chemical catalog company, Inc., 1934.

[9] Pohl HA. *Dielectrophoresis*. Cambridge University Press, 1978.

[10] Jones TB. *Electromechanics of particles*. Cambridge University Press, 1995.

[11] Morgan H and Green NG. *AC Electrokinetics: colloids and nanoparticles*. Research Studies Press Ltd., 1 edition, 2003.

[12] Kang Y, Li D, Kalams SA, and Eid JE. DC-dielectrophoretic separation of biological cells by size. *Biomed. Microdevices*, 10:243–249, 2008.

[13] Gascoyne PRC and Vykoukal J. Particle separation by dielectrophoresis. *Electrophoresis*, 23:1973–1983, 2002.

[14] Xuan X, Zhu J, and Church C. Particle focusing in microfluidic devices. *Microfluid. Nanofluid.*, 9:1–16, 2010.

[15] Pethig R. Dielectrophoresis: using inhomogeneous AC electrical fields to separate and manipulate cells. *CRC Cr. Rev. Biotechn.*, 16(4):331–348, 1996.

[16] Pethig R and Markx GH. Applications of dielectrophoresis in biotechnology. *Trends in Biotechnol.*, 15(10):426–432, 1997.

[17] Cummings EB and Singh AK. Dielectrophoresis in microchips containing arrays of insulating posts: theoretical and experimental results. *Anal. Chem.*, 75:4724–4731, 2003.

[18] Vahey MD and Voldman J. An equilibrium method for continuous-flow cell sorting using dielectrophoresis. *Anal. Chem.*, 80(9):3135–3143, 2008.

[19] Thwar PK, Linderman JJ, and Burns MA. Electrodeless direct current dielectrophoresis using reconfigurable field-shaping oil barriers. *Electrophoresis*, 28(24):4572–4581, 2007.

[20] Demierre N, Braschler T, Muller R, and Renaud P. Focusing and continuous separation of cells in a microfluidic device using lateral dielectrophoresis. *Sensor. Actuat. B-Chem*, 132(2):388–396, 2008.

[21] Zhu J, Tzeng TRJ, Hu Guoqing, and Xuan X. DC dielectrophoretic focusing of particles in a serpentine microchannel. *Microfluid. Nanofluid.*, 7:751–756, 2009.

[22] Chou CF, Tegenfeldt JO, Bakajin O, Chan SS, Cox EC, Darnton N, Duke T, and Austin RH. Electrodeless dielectrophoresis of single- and double-stranded DNA. *Biophys J.*, 83(4):2170–2179, 2002.

[23] Asbury CL, Diercks AH, and van den Engh G. Trapping of DNA by dielectrophoresis. *Electrophoresis*, 23(16):2658–2666, 2002.

[24] Ho CT, Lin RZ, Chang WY, Chang HY, and Liu CH. Rapid heterogeneous liver-cell on-chip patterning via the enhanced field-induced dielectrophoresis trap. *Lab Chip*, 6:724–734, 2006.

[25] Hagedorn R, Fuhr G, MÃijller T, and Gimsa J. Traveling-wave dielectrophoresis of microparticles. *Electrophoresis*, 13(1):49–54, 1992.

[26] Wang XB, Huang Y, Becker FF, and Gascoyne PRC. A unified theory of dielectrophoresis and travelling wave dielectrophoresis. *J. Phys. D Appl. Phys.*, 27(7):1571–1574, 1994.

[27] Kua CH, Lam YC, Rodriguez I, Yang C, and Youcef-Toumi K. Cell motion model for moving dielectrophoresis. *Anal. Chem.*, 80:5454–5461, 2008.

[28] Hughes MP, Morgan H, and Rixon FJ. Measuring the dielectric properties of herpes simplex virus type 1 virions with dielectrophoresis. *BBA-Gen Subjects*, 1571(1):1–8, 2002.

[29] Ratanachoo K, Gascoyne PRC, and Ruchirawat M. Detection of cellular responses to toxicants by dielectrophoresis. *Lab Chip*, 1564(2):449–458, 2002.

[30] Marszalek P, Zielinsky JJ, Fikus M, and Tsong TY. Determination of electric parameters of cell membranes by a dielectrophoresis method. *Biophys. J.*, 59(5):982–987, 1991.

[31] Docoslis A, Kalogerakis N, Behie LA, and Kaler KVIS. A novel dielectrophoresis-based device for the selective retention of viable cells in cell culture media. *Biotechnol. Bioeng.*, 54(3):239–250, 1997.

[32] Perch-Nielsen IR, Bang DD, Poulsen CR, El-Ali J, and Wolff A. Removal of pcr inhibitors using dielectrophoresis as a selective filter in a microsystem. *Lab Chip*, 3:212–216, 2003.

[33] Kadaksham J and Singh P Aubry N. Dielectrophoresis induced clustering regimes of viable yeast cells. *Electrophoresis*, 26(19):3738–3744, 2005.

[34] Zhu K, Kaprelyants AS, Salina EG, Schuler M, , and Markx GH. Construction by dielectrophoresis of microbial aggregates for the study of bacterial cell dormancy. *Biomicrofluidics*, 4(2):022810, 2010.

[35] Velev OD and Bhatt KH. On-chip micromanipulation and assembly of colloidal particles by electric fields. *Soft Matter*, 2:738–750, 2006.

[36] Yang M, Lim CC, Liao R, and Zhang X. Oriented and vectorial patterning of cardiac myocytes using a microfluidic dielectrophoresis chip–towards engineered cardiac tissue with controlled macroscopic anisotropy. *J Microelectromech S*, 15(6):1483–1490, 2006.

[37] Yang M and Zhang X. Electrical assisted patterning of cardiac myocytes with controlled macroscopic anisotropy using a microfluidic dielectrophoresis chip. *Sensor Actuat A-Phys*, 135:73–79, 2007.

[38] Gupta S, Alargova RG, Kilpatrick PK, and Velev OD. On-chip electric field driven assembly of biocomposites from live cells and functionalized particles. *Soft Matter*, 4:726–730, 2008.

[39] Hermanson KD, Lumsdon SO, Williams JP, Kaler EW, and Velev OD. Dielectrophoretic assembly of electrically functional microwires from nanoparticle suspensions. *Science*, 294(5544):1082–1086, 2001.

[40] Lumsdon SO, Kaler EW, and Velev OD. Two-dimensional crystallization of micropsheres by a coplanar AC electric field. *Langmuir*, 20:2108–2116, 2004.

[41] Kang KH, Xuan X, Kang Y, and Li D. Effects of DC-dielectrophoretic force on particle trajectories in microchannels. *J. Appl. Phys.*, 99(6):064702, 2006.

[42] Barbulovic-Nad I, Xuan X, Lee JSH, and Li D. DC-dielectrophoretic separation of microparticles using an oil droplet obstacle. *Lab Chip*, 6:274–279, 2006.

[43] Church C, Zhu J, Wang G, Tzeng TRJ, and Xuan X. Electrokinetic focusing and filtration of cells in a serpentine microchannel. *Biomicrofluidics*, 3:044109, 2009.

[44] Zhu J and Xuan X. Particle electrophoresis and dielectrophoresis in curved microchannels. *J. Colloid Interf. Sci.*, 340:285–290, 2009.

[45] Ai Y, Qian S, Sheng L, and Joo SW. Dielectrophoretic choking phenomenon in a converging-diverging microchannel. *Biomicrofluidics*, 4:013201, 2005.

[46] Cummings EB, Griffiths SK, Nilson RH, and Paul PH. Conditions for similitude between the fluid velocity and electric field in electroosmotic flow. *Anal. Chem.*, 72:2526–2532, 2000.

[47] Santiago JG. Electroosmotic flows in microchannels with finite inertial and pressure forces. *Anal. Chem.*, 73:2353–2365, 2001.

[48] Santiago JG. Comments on the conditions for similitude in electroosmotic flows. *J. Colloid Interf. Sci.*, 310:675–677, 2007.

[49] Kwon JS, Maeng JS, Chun MS, and Song S. Improvement of microchannel geometry subject to electrokinesis and dielectrophoresis using numerical simulations. *Microfluid. Nanofluid.*, 5:23–31, 2008.

[50] Church C, Zhu J, Nieto J, Keten G, Ibarra E, and Xuan X. Continuous particle separation in a serpentine microchannel via negative and positive dielectrophoresis focusing. *J. Micromech. Microeng.*, 20:1–6, 2010.

[51] Çetin B and Li D. Lab-on-a-chip device for continuous particle and cell separation based on electrical properties via alternating current dielectrophoresis. *Electrophoresis*, 31:3035–3043, 2010.

[52] Lo YJ and Lei U. Experimental validation of the theory of wall effect on dielectrophoresis. *Appl. Phys. Lett.*, 97:093702, 2010.

[53] Liang L, Ai Y, Zhu J, Qian Shizhi, and Xuan X. Wall-induced lateral migration in particle electrophoresis through a rectangular microchannel. *J. Colloid Interf. Sci.*, 347:142–146, 2010.

[54] Liang L, Qian Shizhi, and Xuan X. Three-dimensional electrokinetic particle focusing in a rectangular microchannel. *J. Colloid Interf. Sci.*, 350:377–379, 2010.

[55] Rosales C and Lim KM. Numerical comparison between maxwell stress method and equivalent multipole approach for calculation of the dielectrophoretic force in single-cell traps. *Electrphoresis*, 26:2057–2065, 2005.

[56] Al-Jarro A, Paul J, Thomas DWP, Crowe J, Sawyer N, Rose FRA, and Shakesheff KM. Direct calculation of maxwell stress tensor for accurate trajectory prediction during DEP for 2D and 3D structures. *J. Phys. D: Appl. Phys.*, 40:71–77, 2007.

[57] Asbury CL, Diercks AH, and van den Engh G. Modeling of the dielectrophoretic forces acting upon biological cells: a numerical comparison between finite element/boundary element maxwell stress tensor methods and point-dipole approach. volume 1, pages 184–188, Boston, MA, March 2004. NSTI Nanotechnology Conference and Trade Show.

[58] Ai Y, Park S, Zhu J, Xuan X, Beskok A, and Qian S. DC electrokinetic particle transport in an l-shaped microchannel. *Langmuir*, 26(4):2937–2944, 2010.

[59] Keh HJ and Chen SB. Electrophoresis of a colloidal sphere parallel to a dielectric plane. *J. Fluid Mech.*, 194:377–390, 1988.

[60] Young EWK and Li D. Dielectrophoretic force on a sphere near a planar boundary. *Langmuir*, 21(25):12037–12046, 2005.

[61] Yariv E and Brenner H. The electrophoretic mobility of a closely fitting sphere in a cylindrical pore. *SIAM J. Appl. Math*, 64(2):423–441, 2003.

[62] Yariv E and Brenner H. Near-contact electrophoretic motion of a sphere parallel to a planar wall. *J. Fluid Mech.*, 484:85–111, 2003.

[63] Yariv E. "force-free" electrophoresis? *Phys. Fluids*, 18:031702, 2006.

[64] Ye C and Li D. 3D transient electrophoretic motion of a spherical particle in a t-shaped rectangular microchannel. *J. Colloid Interf. Sci.*, 272(2):480–488, 2004.

[65] Hsu JP and Kuo CC. Electrophoresis of a finite cylinder positioned eccentrically along the axis of a long cylindrical pore. *J. Phys. Chem. B*, 110(35):17607–17615, 2006.

[66] Davison SM and Sharp KV. Transient simulations of the electrophoretic motion of a cylindrical particle through a 90 degrees corner. *Microfluid. Nanofluid.*, 4(5):409–418, 2008.

[67] Pozrikidis C. *Boundary integral and singularity methods for linearized viscous flow*. Cambridge University Press, New York, 1992.

[68] Sellier A. On boundary effects in electrophoresis. *C. R. Acad. Sci. Sèrie IIb*, 329(8):565–570, 2001.

[69] Allison SA and Xin Y. Electrokinetic transport of rigid macroions in the thin double layer limit: A boundary element approach. *J. Colloid Interf. Sci.*, 288(2):616–628, 2005.

[70] Wong X and Rosales C. Robust dielectrophoretic single-cell trap design using BEM. *Eng. Anal. Bound. Elem.*, 32:388–394, 2008.

[71] House DL and Luo H. Electrophoretic mobility of a colloidal cylinder between two parallel walls. *Eng. Anal. Boundary Elem.*, 34(5):471–476, 2010.

[72] House DL and Luo H. Effect of DC dielectrophoresis on the trajectory of a non-conducting colloidal sphere in a bent pore. *Electrophoresis*, in press, 2011.

[73] Srivastava SK, Gencoglu A, and Minerick AR. DC insulator dielectrophoretic applications in microdevice technology: a review. *Analytical and Bioanalytical Chemistry*, 2011.

[74] Çetin B. *Microfluidic continuous separation of particles and cells by AC-dielectrophoresis*. PhD thesis, Vanderbilt University, 2009.

[75] Wang X, Wang XB, and Gascoyne PRC. General expressions for dielectrophoretic force and electrorotational torque derived using the maxwell stress tensor method. *J. Electrostat.*, 39:277–295, 1997.

[76] Voldman J. Electrical forces for microscale cell manipulation. *Annu. Rev. Biomed. Eng.*, 8:425–454, 2006.

[77] Markx GH and Davey CL. The dielectric properties of biological cells at radiofrequencies: applications in biotechnology. *Enzyme Microb Tech*, 25:161–171, 1999.

[78] Castellanos A, Ramos A, González A, Green NG, and Morgan H. Electrohydrodynamics and dielectrophoresis in microsystems: scaling laws. *J Phys D Appl Phys*, 36:2584–2597, 2003.

[79] Gencoglu A, Camacho-Alanis F, Nguyen VT, Nakano A, Ros A, and Minerick AR. Quantification of ph gradients and implications in insulator-based dielectrophoresis of biomolecules. *Electrophoresis*, 2011.

[80] Zhu J, Canter RC, Keten G, Vedantam P, Tzeng TJ, and Xuan X. Continuous-flow particle and cell separations in a serpentine microchannel via curvature-induced dielectrophoresis. *Microfluid. Nanofluid.*, 11(6):743–752, 2011.

[81] Moncada-Hernandez H, Baylon-Cardiel JL, Pérez-González VH, and Lapizco-Encinas BH. Insulator-based dielectrophoresis of microorganisms: theoretical and experimental results. *Electrophoresis*, 32:1–10, 2011.

[82] Gascoyne PRC, Wang XB, Huang Y, and Becker FF. Dielectrophoretic separation of cancer cells from blood. *IEEE Trans. Ind. Appl. Soc.*, 33:670–678, 1997.

[83] Pozrikidis C. *A practical guide to boundary element methods with the software library BEMLIB*. CRC Press, 2002.

[84] Keh HJ and Anderson JL. Boundary effects on electrophoretic motion of colloidal spheres. *J. Fluid Mech.*, 153:417–439, 1985.

[85] Hsu JP, Chen ZS, Ku MH, and Yeh LH. Effect of charged boundary on electrophoresis: sphere in spherical cavity at arbitrary potential and double-layer thickness. *J. Colloid Interf. Sci.*, 314(1):256–263, 2007.

[86] Keh HJ and Hsieh TH. Electrophoresis of a colloidal sphere in a spherical cavity with arbitrary zeta potential distributions and arbitrary double-layer thickness. *Langmuir*, 24(2):390–398, 2008.

[87] Keh HJ, Horng KD, and Kuo J. Boundary effects on electrophoresis of colloidal cylinders. *J. Fluid Mech.*, 231:211–228, 1991.

[88] Unni HN, Keh HJ, and Yang C. Analysis of electrokinetic transport of a spherical particle in a microchannel. *Electrophoresis*, 28(4):658–664, 2007.

[89] Keh HJ and Chiou JY. Electrophoresis of a colloidal sphere in a circular cylindrical pore. *AIChE. J.*, 42(5):1397–1406, 1996.

[90] Ye C and Li D. Electrophoretic motion of a sphere in a microchannel under the gravitational field. *J. Colloid Interf. Sci.*, 251:331–338, 2002.

[91] Gagnon Z. R. Cellular dielectrophoresis: Applications to the characterization, manipulation, separation and patterning of cells. *Electrophoresis*, 32:2466–2487, 2011.

[92] Grzelczak M., Vermant J., Furst E. M., and Liz-Marzán L. M. Directed self-assembly of nanoparticles. *A.C.S. Nano*, 4(7):3591–3605, 2010.

[93] Markx G. H., Carney L., Littlefair M., Sebastian A., and Buckle A. M. Recreating the hematon: microfabrication of artificial haematopoietic stem cell microniches in vitro using dielectrophoresis. *Biomed. Microdevices*, 11:143–150, 2009.

[94] Velev OD, Gangwal S, and Petsev DN. Particle–localized AC and DC manipulation and electrokinetics. *Annu. Rep. Sect. C*, 105:213–246, 2009.

[95] Lumsdon SO, Kaler EW, Williams JP, and Velev OD. Dielectrophoretic assembly of oriented and switchable two-dimensional photonic crystals. *Appl. Phys. Lett.*, 82(6):949–951, 2003.

[96] Kang KH and Li D. Dielectric force and relative motion between two spherical particles in electrophoresis. *Langmuir*, 22:1602–1608, 2006.

[97] Ai Y and Qian S. DC dielectrophoretic particle–particle interactions and their relative motions. *J. Colloid Interf. Sci.*, 346:448–454, 2010.

[98] Singh JP, Lele PP, Nettesheim F, Wagner NJ, and Furst EM. One- and two-dimensional assembly of colloidal ellipsoids in AC electric fields. *Phys. Rev. E*, 79(5):050401, 2009.

[99] Herlihy KP, Nunes J, and DeSimone JM. Electrically driven alignment and crystallization of unique anisotropic polymer particles. *Langmuir*, 24(16):8421–8426, 2008.

[100] Glotzer SC and Solomon MJ. Anisotropy of building blocks and their assembly into complex structures. *Nat. Mater.*, 6:557–562, 2007.

[101] Gomez FA. *Biological applications of microfluidics*. Wiley Interscience, 2008.

[102] Wan YW and Keh HJ. Electrophoresis of an axisymmetric particle along its axis of a revolution perpendicular to two parallel plane walls. *Microfluid. Nanofluid.*, in press, 2010.

[103] Teixeira-Pinto AA, Nejelski Jr. LL, Cutler JL, and Heller JH. The behavior of unicellular organisms in an electromagnetic field. *Exp. Cell Res.*, 20(3):548–564, 1960.

[104] Saito M, Schwan HP, and Schwarz G. Response of nonspherical biological particles to alternating electric fields. *Biophys. J.*, 6(3):313–327, 1966.

[105] Yariv E. Inertia-induced electrophoretic interactions. *Phys. Fluids*, 16:24–27, 2004.

[106] Swaminathan TN and Hu HH. Particle interactions in electrophoresis due to inertia. *J. Colloid Interf. Sci.*, 273(1):324–330, 2004.

[107] Reed LD and Jr. FA Morrison. Hydrodynamic interactions in electrophoresis. *J. Colloid Interf. Sci.*, 54(1):117–133, 1976.

[108] Anderson JL. Colloid transport by interfacial forces. *Ann. Rev. Fluid Mech.*, 21:61–99, 1989.

[109] Keh HJ and Chen SB. Particle interactions in electrophoresis: Ii. motion of two spheres normal to their line of centers. *J. Colloid Interf. Sci.*, 130(2):556–567, 1989.

[110] Brenner H. The slow motion of a sphere through a viscous fluid towards a plane surface. *Chem. Eng. Sci.*, 16:242–251, 1961.

[111] Chwang AT and Wu TY. Hydromechanics of low-Reynolds number flow. Part 2. Singularity method for stokes flows. *J Fluid Mech*, 67(4):787–815, 1975.

[112] Xuan X. Joule heating in electrokinetic flow. *Electrophoresis*, 298:33–43, 2008.

[113] Çetin B and Li D. Effect of joule heating on electrokinetic transport. *Electrophoresis*, 29:994–1005, 2008.

[114] Ai Y, Mauroy B, Sharma A, and Qian S. Electrokinetic motion of a deformable particle: Dielectrophoretic effect. *Electrophoresis*, 32:2282–2291, 2011.

[115] Kang KH, Kang Y, Xuan X, and Li D. Continuous separation of microparticles by size with direct current-dielectrophoresis. *Electrophoresis*, 27:694–702, 2006.

[116] Doh I and Cho YH. A continuous cell separation chip using hydrodynamic dielectrophoresis (DEP) process. *Sensor Actuat A-Phys*, 121:59–65, 2005.

[117] Choi S and Park JK. Microfluidic system for dielectrophoretic separation based on a trapezoidal electrode array. *Lab Chip*, 5:1161–1167, 2005.

[118] Nieuwenhuis JH, Jachimowicz A, Svasek P, and Vellekoop MJ. Optimization of microfluidic particle sorters based on dielectrophoresis. *IEEE Sens J*, 5(5):810–816, 2005.

[119] Çetin B, Kang Y, Wu Z, and Li D. Continuous particle separation by size via ac-dielectrophoresis using a lab-on-a-chip device with 3D electrodes. *Electrophoresis*, 30:766–772, 2009.

[120] Çetin B and Li D. Microfluidic continuous particle separation via ac-dielectrophoresis with 3D electrodes. Boston, MA, October 2008. ASME International Mechanical Engineering Congress and Exposition (IMECE'08).